

Expanding the repertoire of DNA-mediated signaling in DNA repair

Thesis by

Timothy Paul Mui

In Partial Fulfillment of the Requirements

for the Degree of

Doctor of Philosophy

California Institute of Technology

Pasadena, California



2014

(Defended September 6th, 2013)

UMI Number: 3597170

All rights reserved

INFORMATION TO ALL USERS

The quality of this reproduction is dependent upon the quality of the copy submitted.

In the unlikely event that the author did not send a complete manuscript and there are missing pages, these will be noted. Also, if material had to be removed, a note will indicate the deletion.



UMI 3597170

Published by ProQuest LLC (2013). Copyright in the Dissertation held by the Author.

Microform Edition © ProQuest LLC.

All rights reserved. This work is protected against unauthorized copying under Title 17, United States Code



ProQuest LLC.
789 East Eisenhower Parkway
P.O. Box 1346
Ann Arbor, MI 48106 - 1346

© 2014

Timothy Paul Mui

All Rights Reserved

ACKNOWLEDGEMENT

Graduate school is a marathon, well maybe more of a sprint marathon.

Throughout this race I have received constant support from a variety of sources that have ultimately helped me to complete this race, and I would like to take this moment to thank everyone who helped me along the way. First of all, I would like to thank my committee for unparalleled academic support. My advisor, Professor Jackie Barton, has provided a great lab environment to work in, given me many challenges that have helped me grow as a scientist, and supported me in my many endeavors. She has taught me the importance of obtaining a good work-life balance. My committee chair, Professor Harry Gray, has always provided great discussion and was always willing to lend an ear. Professor Sarah Reisman has always been a source of enthusiasm, encouragement, and provided an important outside perspective to my scientific problems throughout graduate school. Finally, I would like to thank Professor Judy Campbell for not only engaging in extremely helpful discussions about yeast and yeast proteins, but also for opening up her lab to help us with our projects. I'd also like to thank our collaborators Professor John Tainer and Justin Ishida, and, in particular, Dr. Jill Fuss, whose expertise in not only protein biology, but also DNA repair has been invaluable to me. I would like to thank her for always being available to discuss problems and providing a constant supply of protein. I'd also like to thank my undergraduate advisor Scott Silverman as well as Dana Baum for their constant encouragement and initial research training.

During a race, I would find it impossible to make it through without aid. I'd like to thank the many members of the support staff here at Caltech, who go above and beyond their jobs to make graduate school much easier. Throughout my time here,

Agnes Tong has been a constant source of humor and encouragement. Her love of Disney and travel is enthusiastic, and I will miss dropping by her office to catch up and have a quick cup of coffee. Steve, Leah, and Elisa have made sure that I always have what I need. Joe, Ron, and Memo have been invaluable when the bunker is a mess, letting me drive the cart, and always being friendly. Silva is amazing for her vast computer knowledge and is always upbeat and cheerful. I'd like to finally thank Maureen Renta for always having a good pot of coffee, a good story, and always being supportive for whatever problems I had. She has been another constant source of support throughout this race, and I can't thank her enough for everything that she has done.

Before even deciding to run a race you need inspiration. My family has provided endless support and has pushed me to always do my best. From an early age my grandparents have always encouraged me to pursue the sciences. My parents, Roth and Jenny, have always helped me pursue my interests even if they were a little out there. They have always stood by my side and provided unconditional love and support. My brother, Michael, is a constant source of inspiration as he pursues what he is passionate about and constantly challenges me to be better. My Aunt Ruth and Uncle Bob have had to mediate endless battles between my brother and myself, so it is thanks to them that I survived long enough to get to grad school. I'd also like to thank my Aunt Kathy and Uncle John for always encouraging me to do after-school activities and providing the three most wonderful cousins in the world, and also my Uncle George and Aunt Jan for always making sure that I'm in tip-top dental shape! I'd also like to thank my aunts and uncles on my mother's side who have always encouraged me to do well in school.

Together, my family has been there for me to not only get me into the race, but also to watch me finish it.

In the early part of a race, it is important to not burn out. I'd like to thank my fellow brothers in Alpha Chi Sigma for their continued support. In particular, those who always got to play the bonus or just wanted to drive down to Matt's: Valerie, Jeanne, Nick, James, Colin, Status, Nick, Kevin, and Kurt. In particular, I'd like to thank my running buddies Joe and Matt for being willing to travel to random places to run a race and maybe stay at a hotel that's a little far from the start line. I'd also like to thank Jason and Julia for their constant support. Ever since undergrad, we've gone on so many adventures and they have always been there for me. My good friend Jason has always been up for a productive conversation ranging from spreads, to straddles, to favorites, to where the euro is going, those topics always kept life interesting over those Fuji lunches. Finally, I thank John and April for always making sure we see each other during winter breaks even though they root for Michigan now. These friends have always kept me going and I've always enjoyed all the great memories that we have shared.

The middle of the race can be boring and it's important to be able to get through this rough patch. I've had the opportunity to work with some of the most amazing people over the years. I'd like to thank Barton group members past and present for always having wonderful discussions and being part of one of the most interesting D-league softball teams out there. I'd especially like to acknowledge the North Side both past and present for putting up with all of my lousy music choices. Also I'd like to thank the lunch crew for always being there; Anna for always being there to talk about mini things

and travel plans, and Katie for always being there when I needed to talk. Finally, to Alyson, Alex, and Phil for many tasty dinners, Broad breakfasts and terrible movies.

The last few miles can be the most miserable without proper training and help. These folks helped me throughout the race, but in particular helped me with that last mile. I'd like to thank Alexis and Andrew for being rational and always being willing to lend an ear and for always bringing back coffee! I'd also like to thank my friend Elizabeth for always being a phone call away to help me get through those rough times. DJ Pam has always been a source of humor, encouragement, and a great joke! I'll always remember our crazy adventures and wonderful memories. This goes without saying, but Kaycie has been the most incredible friend ever, and I'd like to thank for her always listening to my crazy issues over Go China and for preventing me from making the biggest mistake of my life. Finally, I'd like to thank my favorite co-worker, Ariel, without whom I don't think I could've made it through the last kick; she bakes the best pumpkin pies and always makes me smile.

Abstract

DNA damage is extremely detrimental to the cell and must be repaired to protect the genome. A variety of mechanisms exist to repair DNA damage, which speaks to the importance of the integrity of DNA. DNA is capable of conducting charge through the overlapping π -orbitals of stacked bases; this phenomenon is extremely sensitive to perturbations in the π -stack, as they attenuate DNA charge transport (CT). Based on the *E. coli* base excision repair (BER) proteins EndoIII and MutY, it has recently been proposed that redox-active proteins containing metal clusters can utilize DNA CT to signal one another to locate sites of DNA damage.

To expand our repertoire of proteins capable of utilizing DNA-mediated signaling, we measured the DNA-bound redox potential of the nucleotide excision repair (NER) helicase XPD from *Sulfolobus acidocaldarius*. A midpoint potential of 82 mV versus NHE was observed, resembling that of the previously reported BER proteins. The redox signal increases in intensity with ATP hydrolysis in only the WT protein and mutants that maintain ATPase activity; an increase was not observed for ATPase-deficient mutants. The signal increase was found to correlate directly with ATP activity, suggesting that DNA-mediated signaling may play a general role in protein signaling.

Several mutations in human XPD that lead to XP-related diseases have been identified. Using SaXPD, we explored how these mutations, which are conserved in the thermophile, affect protein electrochemistry. Biochemically, the G34R, R460P, and A511R mutants are both ATPase- and helicase-deficient, while the L325V and R460W mutants have activities resembling the WT protein. On DNA-modified electrodes, the G34R mutant exhibits a redox signal comparable to the WT protein, while the L325V,

R460P, R460W and A511R mutants are CT deficient. Attempts were made to restore CT activity to CT-deficient mutants using an artificial mutant, Y104A, that showed an enhanced redox signal. However, incorporation of this second Y104A mutation into CT-deficient mutants did not restore their CT capabilities. Based on the SaXPD crystal structure, we also modeled an L325V/M331A mutant in another attempt to restore CT, which was similarly unsuccessful.

To further understand the electrochemical signaling of XPD, we initiated studies on the yeast *S. cerevisiae* Rad3 protein. After purification, we measured ATPase, helicase, and DNA-binding activities of the WT, G47R, I463V/del716-730, R618P, R618W, and C665R protein mutants, which are analogous mutations to those explored in SaXPD. The Rad3 protein exhibits activity similar to the SaXPD proteins. Interestingly, the Rad3 mutants all contain a [4Fe-4S] cluster, as evidenced by a UV-Vis absorbance at 410 nm. ScRad3 mutants were incubated on a DNA-modified electrode, and exhibit a midpoint redox potential of 80 mV versus NHE consistent with the previously reported proteins containing [4Fe-4S] clusters.

To investigate the role of Rad3 *in vivo*, we developed a haploid strain of *S. cerevisiae* that has Rad3 knocked out and complemented with Rad3 on a plasmid. In both a UV-and a 4-nitroquinoline 1-oxide (NQO) survival assay, the ATPase- and helicase-deficient G47R, R618P, and C665R mutants have little to no survival at either 20 J/m² or 20 ng/mL NQO, while the mutants I463V/del716-730 and R618W exhibit survival similar to WT. Growth curves show similar results; ATPase and helicase deficient mutants show t_{1/2} shifts greater than 15 hours compared to the WT strain, which has a t_{1/2} shift of only 1.5 hours. When assayed on DNA-modified electrodes, these

protein mutants exhibit DNA signals closely resembling the WT protein, suggesting these mutations do not alter the potential of the cluster. Finally, the survival ability of these strains in the presence of different DNA damaging agents was tested. When the WT and G47R strains were challenged with hydroxyurea (HU), methyl methanesulfonate (MMS), and camptothecin (CPT), both strains exhibit comparable activity in the presence of HU, while with MMS and CPT, the G47R strain exhibits a significant change in $t_{1/2}$ compared to the WT, suggesting that Rad3 is involved in repairing damage beyond traditional NER substrates.

We additionally utilized an atomic force microscopy (AFM) assay that measures the ability of proteins to relocalize in the vicinity of damage. In protein samples of EndoIII or SaXPD, we observed a binding density ratio (BDR) of ~ 1.5 for both proteins, suggesting that the proteins redistribute onto the strands containing a single C:A mismatch. However, in mixtures of protein samples where either EndoIII or SaXPD is CT-deficient, a BDR of ~ 1.0 is observed. These data suggest that a) proteins from completely different repair pathways and organisms can signal one another to coordinate to a site of DNA damage and b) that deficiencies in CT play a large role in coordinating protein binding at sites of DNA damage.

The results described here involve investigations of new proteins for DNA repair that contain a redox active [4Fe-4S] cluster. By utilizing electrochemistry, an AFM assay, and previously established spectroscopic techniques, we have characterized a new group of proteins capable of performing DNA-mediated CT. We find that protein activity can be correlated to electrochemical activity, and that DNA-mediated signaling

can be utilized by a variety of DNA repair proteins that bind DNA and contain a [4Fe-4S] cluster.

TABLE OF CONTENTS

Acknowledgement	iii
Abstract.....	vi
Table of contents	x
List of figures and schemes	xii
List of tables.....	xiv
Chapter 1. Biological context of DNA-mediated Charge Transport DNA-mediated Charge Transport in DNA repair	
DNA repair Pathways	2
Base Excision Repair (BER)	2
Mismatch Repair (MMR)	5
Double Strand Break (DSB) repair.....	8
Nucleotide Excision Repair (NER)	11
DNA-mediated Charge Transport	13
Redox signaling in the cell.....	16
Activation of transcription with DNA CT	18
Cellular processes involving DNA CT.....	18
DNA CT through Metalloproteins.....	20
References	23
Chapter 2. ATP-stimulated DNA-mediated redox signaling by XPD, a DNA repair and transcription helicase	
Introduction	28
Materials and Methods	30
Results and Discussion	
Electrochemistry on DNA-modified electrodes (Au)	34
Magnesium addition enhances ATP-dependent DNA-mediated signaling	47
SaXPD incubation on a DNA-modified electrode	47
Substrate specificity of SaXPD electrochemistry	49
Optimizing protein concentration for electrochemical ATPase assay	49
Endonuclease III ATPase titration	53
Bulk Electrolysis of SaXPD on DNA-modified electrodes	53
SaXPD on HOPG electrodes	56
Light-activated ATP activation with SaXPD	58
References	61
Chapter 3. Charge transfer properties of mutants related to the human diseases xeroderma pigmentosum, cockayne syndrome, and trichothiodystrophy in the [4Fe-4S] cluster-containing helicase XPD from <i>Sulfolobus acidocaldarius</i>	
Introduction	65
Materials and Methods	67
Results	
SaXPD single mutations: biochemical characterization and electrochemical characterization	71
Double mutant electrochemistry to restore CT to single point mutants	77
Modeling a double mutant to restore CT to the deficient L325V mutant in SaXPD	79
Discussion	83
References	86

Chapter 4. Initial electrochemical observations from other [4Fe-4S] cluster containing proteins related to DNA repair	
Introduction	91
Materials and Methods	95
Results	
Isolation of haploid <i>S. cerevisiae</i> with a Rad3 knockout for survival studies	102
Characterization of Rad3 knockouts	104
UV-survival assay	110
NQO-survival assay	113
Mutations at R618 in <i>S. cerevisiae</i> Rad3 show variable growth in response to NQO...	116
Effect of Rad3 mutants in survival from non-NER DNA damaging agents	119
qPCR to monitor transcription of DNA repair genes in Rad3 mutant <i>S. cerevisiae</i>	123
Isolation of <i>S. cerevisiae</i> Rad3	126
Biochemical characterization of <i>S. cerevisiae</i> Rad3	128
Electrochemical characterization of Rad3 on DNA-modified electrodes.....	136
Discussion	140
References	145
Chapter 5. DNA charge transport as a first step in coordinating the detection of lesions by repair proteins	
Introduction	152
Materials and Methods	157
Results	
Experimental strategy using AFM to probe protein distribution	162
Detection of XPD Complexes.....	163
Atomic Force Microscopy of Protein Mixtures	165
Discussion	168
References	176
Chapter 6. Summary and outlook.....	182
Appendix 1. Primers and plasmids for <i>S. cerevisiae</i> in vivo assays.....	190

LIST OF FIGURES AND SCHEMES

Chapter 1 Figures

1.1 Base excision repair schematic	4
1.2 Mismatch repair cartoon schematic	7
1.3 DSB repair by NHEJ	10
1.4 Nucleotide excision repair schematic	12
1.5 DNA Charge Transport	14
1.6 Proposed model for DNA-mediated signaling	22

Chapter 2 Figures

2.1 Cartoon schematic of DNA-modified electrode for SaXPD electrochemistry	35
2.2 Electrochemistry of DNA-bound WT SaXPD	36
2.3 ATP-dependent electrochemistry of SaXPD on different DNA substrates	39
2.4 ATP-dependent electrochemistry of SaXPD on different DNA substrates illustrated	40
2.5 ATP-dependent signal increase with 5 mM ATP addition	41
2.6 Electrochemical comparisons of SaXPD mutants after 5 mM ATP addition	43
2.7 Electrochemistry of SaXPD on control surfaces	45
2.8 UV-Vis spectrum of WT SaXPD	46
2.9 SaXPD on a DNA-modified electrode with ATP and magnesium additions	48
2.10 SaXPD on various DNA films	50
2.11 Concentration dependent signaling of SaXPD	51
2.12 Stability of SaXPD on a DNA-modified electrode	52
2.13 Endonuclease III ATP-dependence	54
2.14 Bulk electrolysis of SaXPD	55
2.15 Electrochemistry of SaXPD on bare HOPG electrodes	57
2.16 Light-activated ATP electrochemistry	59

Chapter 3 Figures

3.1 UV-Vis of various SaXPD mutants	74
3.2 Electrochemical signal for various SaXPD single mutants	76
3.3 Double mutant SaXPD electrochemistry	78
3.4 Pymol model of SaXPD for L325V mutation	81
3.5 Modeled repair of L325V SaXPD mutation	82

Chapter 4 Figures

4.1 Alignment of XPD-family of helicases	94
4.2 Tetrad analysis for generating Rad3 knockout <i>S. cerevisiae</i>	103
4.3 PCR based SDM strategy to delete regions of a plasmid	106
4.4 Rad3 mutant viability by the plasmid shuffle	108
4.5 Growth curves of Rad3 strains in SD-HIS	109
4.6 Calculated thymine dimer damage in yeast <i>S. cerevisiae</i>	111
4.7 UV-survival of Rad3 strains at 200 J/m ²	112
4.8 NQO-survival assay of Rad3 mutants	114
4.9. Effect of NQO on growth for Rad3 strains	115
4.10 Pymol representations of mutations at the R460 position in SaXPD	117
4.11 NQO survival assay for additional Rad3 mutants	118
4.12 Spot assay for Rad3 mutant strains with DNA damaging agents	121

4.13 Effect of DNA damaging agents on Rad3 mutant <i>S. cerevisiae</i> strains	122
4.14 qPCR of DNA repair genes in mutant Rad3 <i>S. cerevisiae</i> strains	124
4.15 Representative protein purification for ScRad3	127
4.16 Representative UV-Vis spectra of ScRad3	129
4.17 ATPase activity of ScRad3 and SaXPD	130
4.18 ATPase activity of Rad3 mutants after storage	131
4.19 Fluorescent helicase activity of Rad3 mutants	133
4.20 Representative FP binding data for Rad3 to fluorophore DNA	134
4.21 Electrochemistry of Rad3 protein on a 5' ssDNA overhang DNA-modified electrode	138
4.22 Electrochemistry of Rad3 protein mutants	139

Chapter 5 Figures

5.1 Model for damage detection and redistribution by repair proteins	156
5.2 Atomic force microscopy to visualize protein	171
5.3 Electrochemistry of WT and L325V SaXPD	172
5.4 Representative tapping mode AFM images	173
5.5 Binding density ratio in mixtures of SaXPD and EndoIII	174

LIST OF TABLES

Chapter 2

2.1 Redox and Biochemical activity of WT and G34R XPD	44
2.2 Representative table of DNA duplex utilized	50

Chapter 3

3.1 Biochemical activity of single SaXPD mutants	75
--	----

Chapter 4

4.1 Yeast strains generated with variants in Rad3 compared to SaXPD	107
4.2 <i>S. cerevisiae</i> genes involved in DNA repair	125
4.2 Relative biochemical activities of ScRad3 and SaXPD	135

Chapter 5

5.1 Binding density ratios for atomic force microscopy samples	175
--	-----

Chapter 1

DNA repair and DNA charge transport

DNA Repair Pathways

DNA is constantly assaulted by a variety of damage sources, ranging from endogenous reactive oxygen species and chemical damaging agents to external high energy UV light (1, 2). Each of these agents causes damage that, if unrepaired, leads to extended genomes, mutations, and cell death. Cells have a variety of DNA repair pathways for specific types of damage, such as base excision repair (BER), which involves the excision of a single damaged base, followed by gap filling and ligation by a polymerase (3). Nucleotide excision repair (NER), in contrast, involves larger substrates that distort the structure of DNA and are repaired by an entirely different family of enzymes (4, 5). Mismatch repair (MMR) machinery uniquely repairs mismatches that occur through DNA polymerization errors (2). While each pathway is almost entirely independent, some enzymatic overlap exists; for example, DNA polymerase ϵ is utilized in both NER and BER. Although the activity of each of the proteins in these pathways is understood, it is not known how proteins from each pathway target their specific lesions (6). In cells, these repair pathways work in tandem to repair the genome before mutations are passed on to future generations.

Base Excision Repair

Base excision repair (BER), a well conserved pathway found in both bacteria and eukaryotes, handles the removal of a damaged base. The enzymes that perform this excision are known as glycosylases because they excise the base from the sugar. DNA bases have many reactive groups, including carbonyls and amines, that can readily react with various chemicals (3). For example, cytosine is easily deaminated to form uracil, which must be subsequently removed by uracil deglycosylase, and guanine can be

oxidized to 8-oxo-guanine, which is removed by the MutY family of DNA glycosylases. These are just a few examples of a slew of other base damage products that have specific glycosylases ready to repair them.

Guanine is particularly susceptible to damage as it has the lowest oxidation potential of all the bases, and is therefore especially prone to oxidation by reactive oxygen species (ROS), which are often indicators of oxidative stress in a cell. The most common oxidation product is 7,8-dihydro-8-oxoguanine (8-oxoguanine, Figure 1.1), which is extremely deleterious to the cell because 8-oxoguanine can behave like a thymine. During replication, this oxidized base can lead to an 8-oxoG:A base pair instead of the correct G:C base pair, and a subsequent round of replication will lead to a T:A transversion (Figure 1.1). The cell has evolved enzymes capable of repairing this damage prior to the incorrect T:A insertion. Initially, MutM (OGG1) excises 8-oxoG from the 8-oxoG:C base pair, but if this lesion remains unrepaired, MutY (MUTYH) remove adenines from the 8:oxoG:A base pair. Once the damaged or incorrect bases are removed, polymerases can complete DNA synthesis without transversion (3). Mutations in the human MutY protein have been directly linked to colorectal cancer; when missense mutations are present in MutY, polyps are often found in the colon, known as MUTYH-associated polyposis. A variety of other progeria exist as a result of BER deficiencies, but the MutY system is the best characterized.

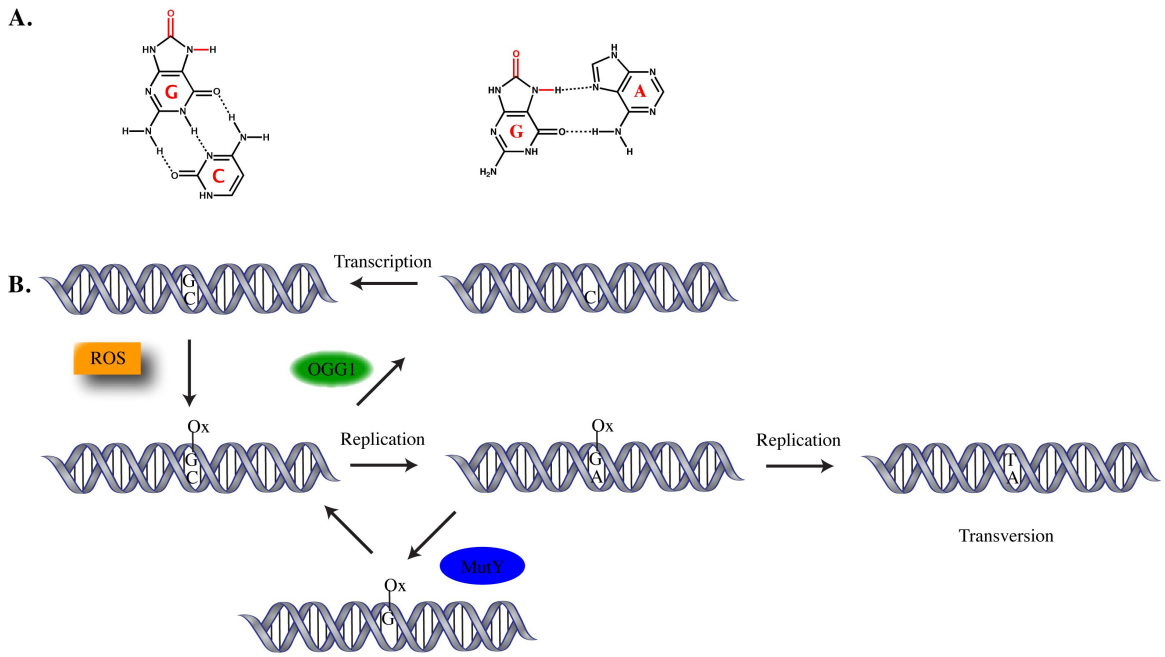


Figure 1.1. Base excision repair schematic. (A). Chemical structures of an 8-oxo guanine: cytosine base pair and an 8-oxo guanine: adenine base pair. (B). Repair process by which DNA is oxidized by a reactive oxygen species (ROS) to generate an 8-oxo guanine: cytosine mis-pair. This can either be removed by OGG1 and subsequently repaired, or a replication error inducing an 8-oxo guanine : adenine mis pair occurs. In this case, MutY must repair the lesion, or a T : A transversion will be permanently included into the DNA genome.

Mismatch Repair

Mismatches in DNA occur when bases pair in a non-Watson Crick fashion (adenine always pairs with thymine and guanine with cytosine). Mismatches are not typically chemically induced, but are the byproducts of poor polymerization (7). In the cell, DNA is replicated at thousands of base pairs per second by the leading strand DNA polymerase ϵ and the lagging strand DNA polymerases α and δ . These proteins replicate DNA at staggering speeds, but are especially error prone. To combat these errors, they contain a proofreading function to verify that the correct nucleotides were incorporated, but errors still occur at a rate of 1 per 1000's of base pairs synthesized (8). Errors are corrected through the mismatch repair (MMR) pathway, which is conserved between bacteria and eukaryotes. MMR is a constant search and repair process generally broken down into four steps. The first is recognition of the mismatch site, performed by the MutS family of proteins. In humans, a heterodimer termed MutS α , composed of human MSH2 and human MSH6, identifies base pair mismatches, while the MutS β complex, composed of human MSH2 and MSH3, scans for insertion and deletion loops. Based on crystal structures, it is currently believed that the complex binds DNA at mismatch sites and actively scans as a sliding clamp with a higher affinity for mismatch DNA in the ATP-bound form and a lower affinity in the ADP-bound form (9) (Figure 1.2).

Subsequent steps in MMR involve the recruitment of additional repair enzymes. In humans, the DNA-MutS-ATP complex brings in the MutL complex, which displaces DNA polymerases and PCNA while also recruiting exonuclease I (Exo1). The nuclease then cleaves either upstream or downstream of the mismatch, which leaves an exposed ssDNA region. This is bound by PCNA, RFCs, and other polymerases. Finally, DNA is resynthesized by DNA polymerase δ to complete the repair process (2) (Figure 1.2).

MMR proteins are therefore very important, and mutations in MMR predispose patients to certain types of cancers as well as Lynch syndrome (9).

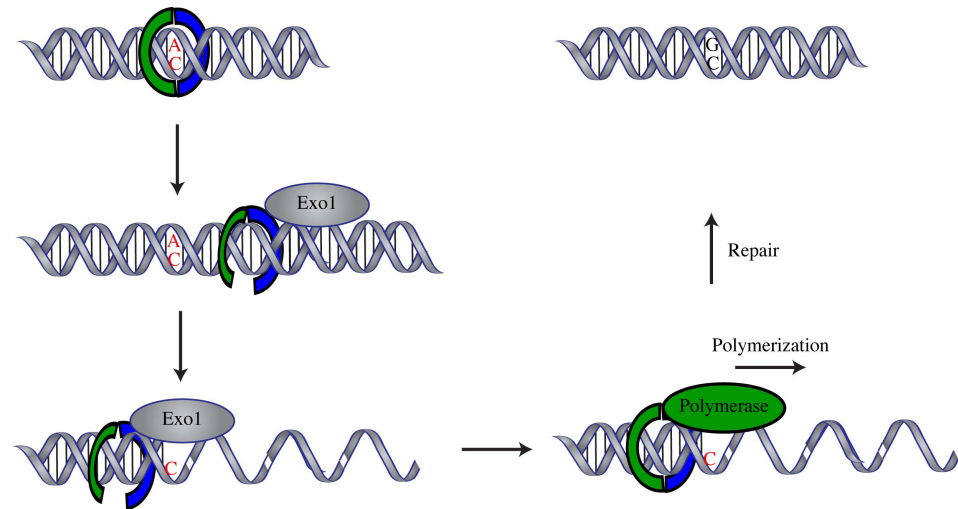


Figure 1.2. Mismatch repair cartoon schematic. Briefly, the MutS α (blue and green ring) binds to a mismatch site upon ATP hydrolysis. The complex slides along the DNA and recruits an exonuclease such as Exonuclease I (ExoI), which then degrades one strand of the DNA, allowing for the PCNA/RFC/polymerase complex to bind and polymerize DNA. This leads to reversion of the DNA mismatch from A : C to G : C.

Double Strand Break Repair

Double strand breaks (DSBs) are extremely detrimental to the cell, as they make DNA more susceptible to a large-scale deletion or other damage that can result in cell death. Double strand breaks are typically caused by collapsed replication forks, nucleases, or exogenous ionizing radiation (10). A double strand break is far more dangerous than a single strand break because there is ambiguity as to which strand is the parent strand, making repair significantly more difficult. The two principal methods for repairing DSBs are either non-homologous end joining (NHEJ) or homologous recombination (HR). NHEJ is considered to be more error-prone, as the termini are rejoined through ligation, while in HR an exchange of two DNA strands occurs, which generally is thought to be error-free (11) (Figure 1.3).

Non-homologous End Joining Repair

A major challenge associated with repairing a double strand break is that the damage can be induced by a variety of sources. Additionally, DSBs typically do not have a clean 5' phosphate and 3' hydroxyl, which are necessary for ligation. Unlike HR, which aligns DNA based on sequence homology, NHEJ ligates the DNA quickly and efficiently. Because this process is independent of sequence, NHEJ is thought to be the primary repair mechanism in non S-phase cells, which have sister chromatids in close proximity, allowing for easy HR. In NHEJ, following break formation the termini are bound with the Ku70/80 heterodimer, which recruits the DNA protein kinase catalytic subunit (XRCC4, XLF and DNA ligase IV). If no end processing is required and the DNA can be ligated, the ligase completes the repair (10). However, more often the DNA must be processed to provide the reactive groups required for ligation. If further

processing is required, other proteins, including Artemis, are recruited to cleave the ends of the DSB complex to generate a viable overhang for ligation by either polymerase μ or polymerase λ (Figure 1.3). NHEJ is important for efficient repair of DSBs and is one of many pathways required to maintain genome integrity.

Homologous Recombination

HR is vital for introducing genetic variability and maintaining genome stability. This process is more complicated and not as well understood as NHEJ, as it involves coordinated repair between two DNA strands. Briefly, when a strand break is generated, the broken end is base paired with the correct complement in the sister chromatid by a recombinase-coated single stranded DNA. Upon sequence alignment, recombinases switch homologous regions, allowing DNA polymerization to occur from the newly formed D-loop. A branch is then created that migrates and resolves to form intact DNA with few errors present (12). This process is much more common in S-phase when both sister chromatids are in close proximity. HR is a vital process for the prevention of DNA damage and requires a variety of proteins for both alignment and repair of the DSB.

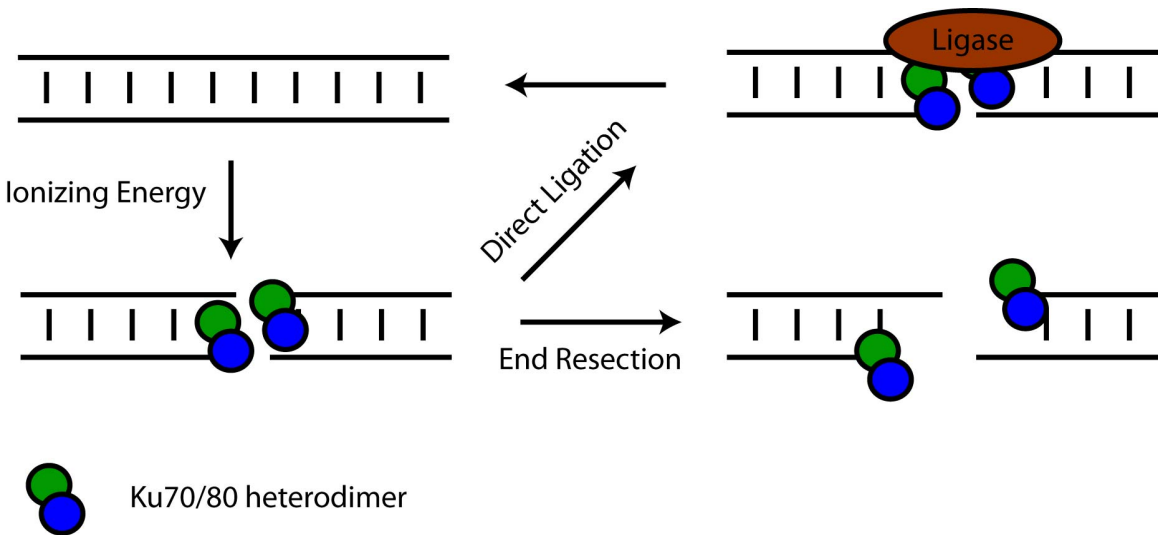


Figure 1.3. DSB repair by NHEJ. Repair via non-homologous end joining (NHEJ). A DSB is formed and bound by the Ku70/80 heterodimer (blue/green balls), and, if end resection is necessary, the proteins recruit Artemis and other proteins to resect the ends. However, if the ends are capable of direct ligation, ligases are recruited for direct ligation.

Nucleotide Excision Repair

NER is responsible for repairing a variety of bulky DNA lesions including UV-induced cyclopyrimidine dimers and chemically-induced DNA damage. These DNA lesions are larger than BER or MMR damage sites and often lead to replication errors and mutations not typically found in those pathways (6). Many proteins involved in NER are implicated in xeroderma pigmentosum (XP)-related diseases, which impart photosensitivity, growth deficiencies, predisposition to cancer, and other aging phenotypes (13). Over thirteen individual proteins have been implicated in the three main NER disorders: xeroderma pigmentosum (XP), trichothiodystrophy (TTD), or cockayne syndrome (CS) (14). Two types of NER exist: global genome repair (GGR) and transcription-coupled repair (TCR). When damage occurs over a transcribed region, repair is coordinated with transcription; the polymerase pauses near a site of damage and recruits the CSA and CSB proteins. The TFIIH core complex, which consists of ten protein subunits including the helicases XPD and XPB, is then recruited. These helicases unwind the DNA near the site of damage to expose it to recruited excision proteins, XPF and XPG. These proteins complete the process through backbone cleavage upstream and downstream of the lesion. Following excision, PCNA-polymerase completes synthesis, and the newly synthesized DNA is ligated. In global genome repair, an alternate recognition element is utilized: XPE or XPC protein is brought to the site of DNA damage. Upon binding, these proteins recruit the TFIIH complex, as described above, and complete NER similarly to TCR (15) (Figure 1.4).

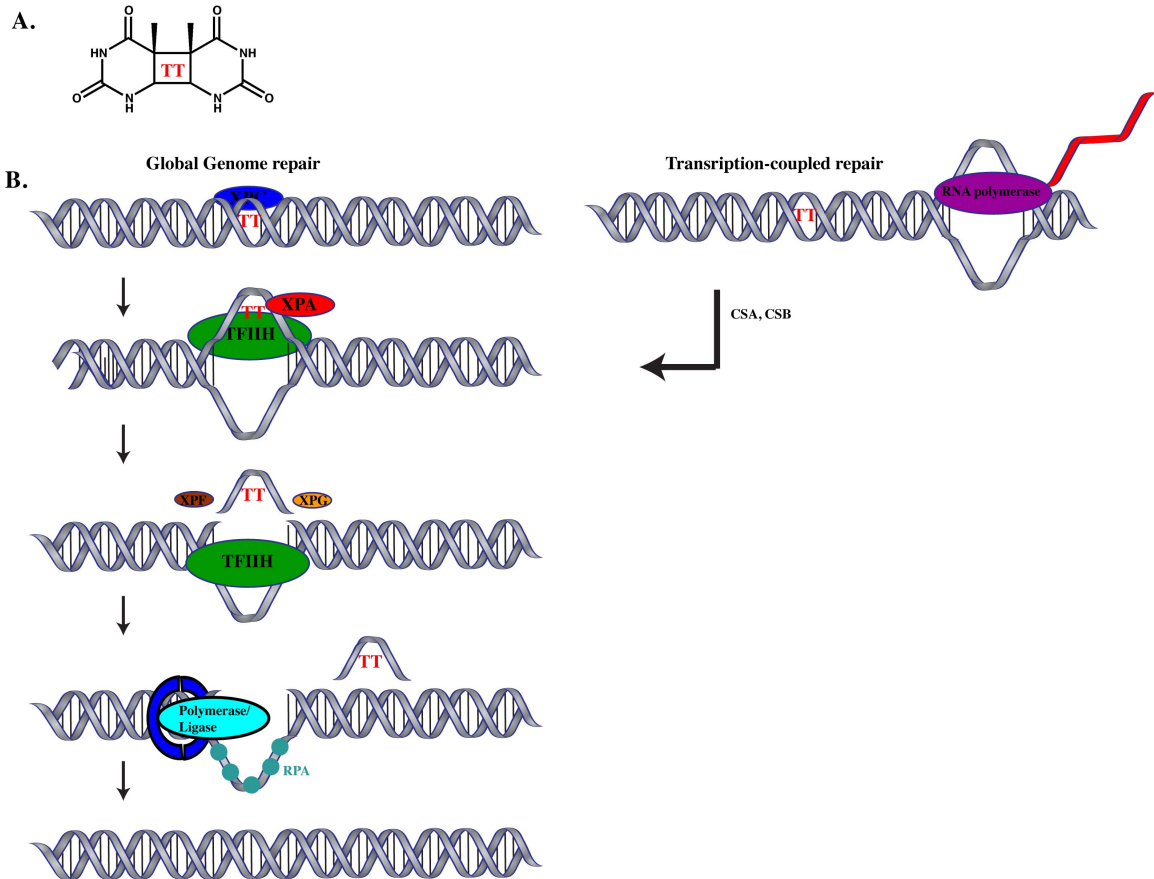


Figure 1.4. Nucleotide excision repair schematic. (A) Chemical structure of two proximal thymines forming a thymine dimer. (B). Cartoon schematic of global genome repair (GGR), in which XPC first binds the site of DNA damage, followed by recruitment of XPD and TFIIH (which is composed of 10-subunits including XPB and XPD). These helicases then unwind around the site of the lesion and recruit XPF and XPG, which cleave on the 5' and 3' sides of the lesion respectively. This cut DNA is then removed, and polymerases and ligases complete the repair process. In transcription coupled repair (TCR), RNA polymerase stalls near the site of the lesion and recruits CSA and CSB proteins, which then follow the normal GGR pathway as indicated by the arrow.

DNA-mediated Charge Transport

DNA is composed of a sequence of four different nucleobases connected by a sugar phosphate backbone. The DNA deoxyribose bases hydrogen bond between strands to form basepairs. The anti-parallel annealing of DNA strands causes base stacking, which aligns the π -orbitals of the bases, enabling electrons to pass through the overlapping π -orbitals (Figure 1.5). This phenomenon, known as DNA Charge Transport (CT), enables DNA to act as a molecular wire (16). Structurally, this process is unaffected by breaks in the sugar phosphate backbone (17). However, perturbations to the DNA π -stack significantly diminish its ability to conduct charge; in DNA, oxidized bases (8-oxo-guanine) and mismatches (cytosine-adenine mismatch) disrupt the π -stacking and interfere with CT (18) (Figure 1.5). Using a chemical probe, DNA CT has been measured by our group through 100 bases. DNA CT over this distance opens the possibility that this process occurs in the cell (19).

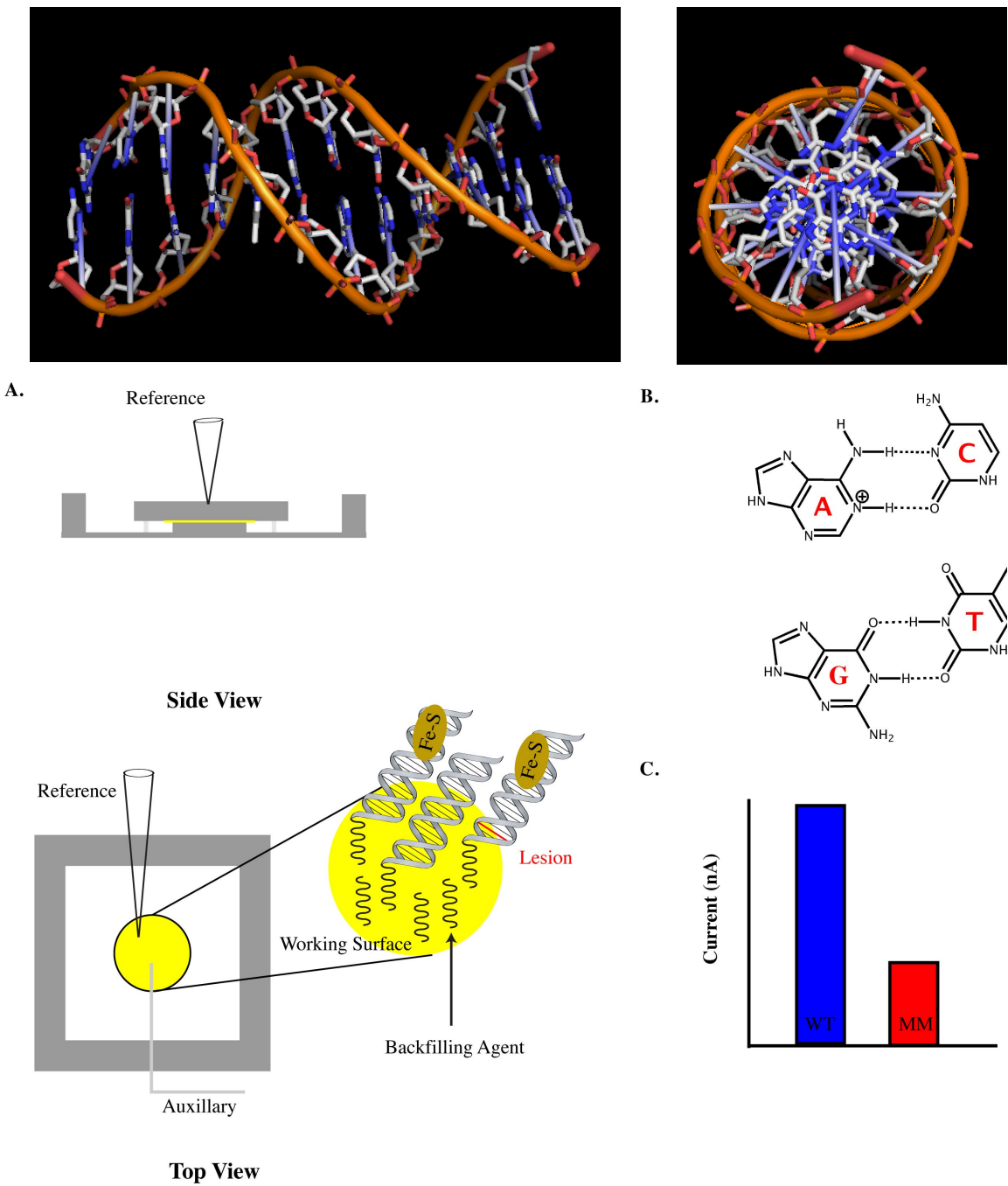


Figure 1.5 DNA charge transport (Top Left) Side-on view of DNA with sugar phosphate backbone shown in orange and the individual bases from (PDB ID 1BNA). (Top Right) Top view of DNA showing that the bases are stacked upon one another, allowing for efficient charge transfer (from PDB ID 1BNA). (A) Side-view and Top-view of single electrodes utilized in the Barton laboratory showing the reference (Ag/AgCl), auxillary (platinum wire) and working surface (DNA self-assembled monolayer on gold). (B) Chemical structures of the cytosine (C): adenine (A) mismatch

and the guanine (G) : thymine (T) mismatch. (C) Electrochemical signal on a DNA self-assembled monolayer (SAM) using well-matched (WT) and mismatched (MM) DNA showing the attenuation of CT by a single DNA mismatch or lesion.

Redox signaling in the cell

Cells contain many redox active molecules that are used to control the redox potential of the cell, including those capable of reacting with and modifying proteins. Some molecules include hydrogen peroxide, peroxynitrite, and nitrogen dioxide. Thiol-based switches utilize redox chemistry to convert two free thiols (from cysteines and methionines) into a disulfide. This is a two-electron process that creates a simple and reliable switch for proteins based on redox conditions of a cell. The redox potential in bacteria is approximately -165 mV in the periplasm, making the reduction/oxidation of disulfides easy (20). The formation of disulfides is also interesting because the conformation of the protein can change upon bond formation, which affects the catalytic ability of the protein. When a disulfide is formed, the protein is locked into a new state that can bind or block substrate binding. This redox control is relatively simple, yet provides an impetus to study these proteins as redox switches.

Many proteins contain redox active moieties. Redox potentials have been measured from -320 mV to upwards of 115 mV, all of which are achievable in the cell. One molecule used to measure the redox potential is glutathione; the ratio of GSH/GSSG gives a good representation of the redox environment of the cell. The ratio is typically 200:1, but under conditions of oxidative stress and other situations that affect the redox potential of the cell, the ratio can change significantly (21). Many molecules have also been implicated in controlling the redox state of the cell, which also affects the proteins therein through chemical reactions with free radicals and other ROS (22). Under conditions of oxidative stress, activation of the Dsb proteins have been shown to be controlled by this redox chemistry. The versatility of the disulfide bond provides an

excellent mechanism for cellular signaling via redox chemistry through intracellular reductants and oxidants.

Activation of transcription via DNA CT

DNA-mediated CT provides an alternative means of redox signaling between proteins. As opposed to using disulfides for redox chemistry, the transcription factor SoxR contains a [2Fe-2S] cluster, which provides an alternative method of redox chemistry. SoxR was originally identified because of its transcriptional activity in response to oxidative stress; when bound to DNA, it exhibits a redox potential of approximately 200 mV versus NHE, compared to the unbound redox potential of -300 mV (23). Interestingly, absence of the cluster in SoxR does not affect binding affinity or folding, but when oxidized, SoxS transcription is induced. Using a covalent rhodium photooxidant, researchers were able to demonstrate that SoxS transcription can be induced via DNA CT and not simply via oxidation of the cysteines in the protein, suggesting a transcriptional role for DNA-mediated signaling (24).

Cellular processes involving DNA CT

DNA-mediated signaling has yet to be concretely proven to be utilized in the cell, but many nucleic acid structures in the cell are capable of conducting charge. DNA wrapped in a histone core particle was shown to be oxidized by photooxidation of a rhodium metal complex, damaging the 5'-guanines in a guanine doublet (25). DNA damage has also been observed in HeLa cell nuclei using a similar photooxidation strategy, demonstrating again that the low potential guanine doublet is a preferred site for DNA damage (26). If DNA is capable of conducting charge through these biologically relevant structures, it provides a potentially unique pathway for protein signaling. Bending of DNA by the TATA binding protein, which attenuates CT, has also been

observed (27). Both SoxR signaling and TBP signal attenuation present unique opportunities for proteins to regulate DNA CT.

DNA CT through metalloproteins

Proteins have a variety of co-factors, ranging from organic chromophores to metals such as zinc and iron. Recently, it has been proposed that DNA CT may be utilized *in vivo* by proteins containing redox active moieties based on experiments with the BER proteins Endonuclease III (EndoIII) and MutY, both of which contain a redox active [4Fe-4S] cluster (28). DNA binding shifts the reduction potential of these clusters by approximately -200 mV to 80 mV vs. NHE. Additionally, in the oxidized state (3+) these proteins have a 1000-fold higher DNA binding affinity than in their reduced state (2+) (29, 30). An AFM assay confirmed that these proteins redistribute onto strands that contain a single base mismatch, which reduces the ability for the proteins to communicate via DNA CT (31). These findings point to a DNA-mediated CT model for protein localization near sites of DNA damage. In this model, freely-diffusing proteins bind DNA, activating them towards oxidation and subsequent release of an electron that travels through the DNA to a distally-bound protein. This distal protein is reduced by the electron and dissociates from the DNA; these proteins essentially conduct a scan of this region of the genome (Figure 1.6). However, if the proteins cannot communicate due to perturbations to the π -stack, the distal protein will not dissociate and will instead localize in the region of damage (32). An *E. coli* assay measuring MutY activity demonstrated that a CT deficient mutant of EndoIII decreases the efficiency of the MutY enzyme in repairing lesions (28). It was subsequently determined that with only MutY and EndoIII proteins, it would take an *E. coli* cell over 40 minutes to scan the entire genome, much longer than the doubling time of the cell. However, if DNA CT occurs over only several hundred base pairs, the search time is reduced from 40 minutes to 5 minutes (28). While

these proteins are both involved in BER, they act on completely different substrates; our findings therefore indicate that there must be cross-communication between these proteins, perhaps by DNA-mediated Charge Transfer.

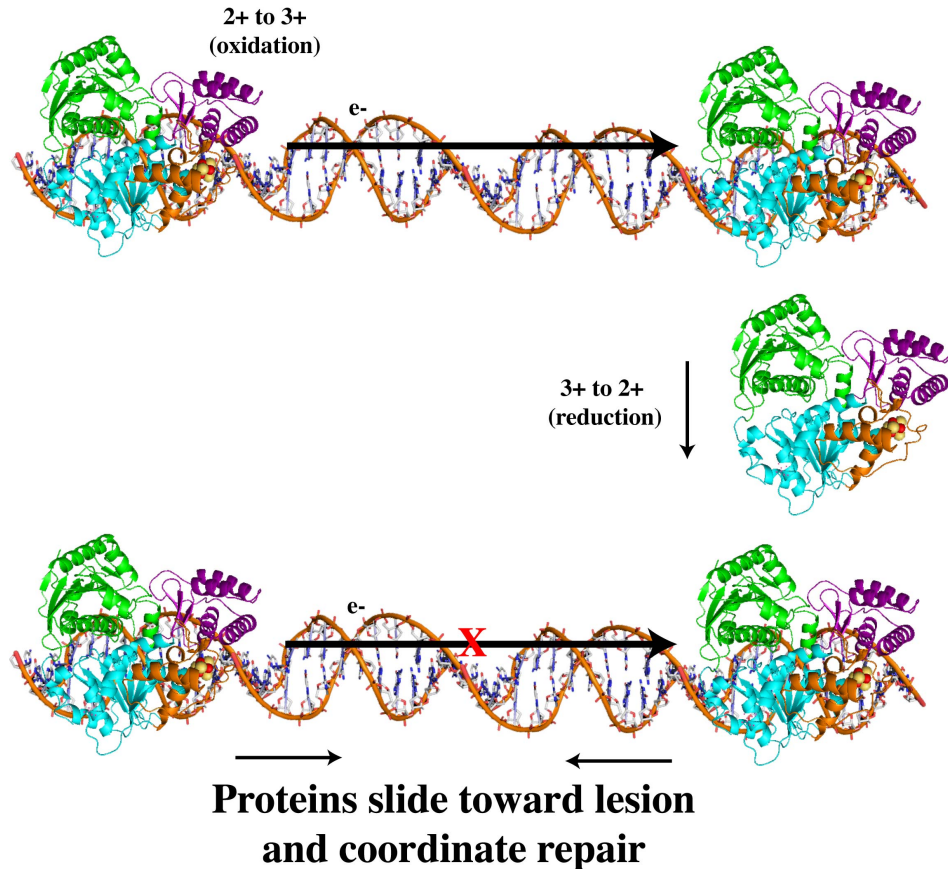


Figure 1.6 Proposed model for DNA-mediated signaling. Proposed model for DNA-mediated signaling between [4Fe-4S] cluster containing proteins.

References

1. Sancar, A., Lindsey-Boltz, L. A., Unsal-Kacmaz, K., and Linn, S. (2004) Molecular mechanisms of mammalian DNA repair and the DNA damage checkpoints, *Annu Rev Biochem* 73, 39-85.
2. Kunkel, T. A., and Erie, D. A. (2005) DNA mismatch repair, *Annu Rev Biochem* 74, 681-710.
3. David, S. S., O'Shea, V. L., and Kundu, S. (2007) Base-excision repair of oxidative DNA damage, *Nature* 447, 941-950.
4. de Boer, J., and Hoeijmakers, J. H. (2000) Nucleotide excision repair and human syndromes, *Carcinogenesis* 21, 453-460.
5. Seroz, T., Winkler, G. S., Auriol, J., Verhage, R. A., Vermeulen, W., Smit, B., Brouwer, J., Eker, A. P., Weeda, G., Egly, J. M., and Hoeijmakers, J. H. (2000) Cloning of a human homolog of the yeast nucleotide excision repair gene MMS19 and interaction with transcription repair factor TFIIH via the XPB and XPD helicases, *Nucleic Acids Res* 28, 4506-4513.
6. Helleday, T., Petermann, E., Lundin, C., Hodgson, B., and Sharma, R. A. (2008) DNA repair pathways as targets for cancer therapy, *Nat Rev Cancer* 8, 193-204.
7. Nick McElhinny, S. A., Watts, B. E., Kumar, D., Watt, D. L., Lundstrom, E. B., Burgers, P. M., Johansson, E., Chabes, A., and Kunkel, T. A. (2010) Abundant ribonucleotide incorporation into DNA by yeast replicative polymerases, *Proc Natl Acad Sci U S A* 107, 4949-4954.
8. Goodman, M. F. (2002) Error-prone repair DNA polymerases in prokaryotes and eukaryotes, *Annu Rev Biochem* 71, 17-50.

9. Jascur, T., and Boland, C. R. (2006) Structure and function of the components of the human DNA mismatch repair system, *Int J Cancer* 119, 2030-2035.
10. Wyman, C., and Kanaar, R. (2006) DNA double-strand break repair: all's well that ends well, *Annu Rev Genet* 40, 363-383.
11. Shrivastav, M., De Haro, L. P., and Nickoloff, J. A. (2008) Regulation of DNA double-strand break repair pathway choice, *Cell Res* 18, 134-147.
12. Li, X., and Heyer, W. D. (2008) Homologous recombination in DNA repair and DNA damage tolerance, *Cell Res* 18, 99-113.
13. Dubaele, S., Proietti De Santis, L., Bienstock, R. J., Keriel, A., Stefanini, M., Van Houten, B., and Egly, J. M. (2003) Basal transcription defect discriminates between xeroderma pigmentosum and trichothiodystrophy in XPD patients, *Mol Cell* 11, 1635-1646.
14. Cleaver, J. E., Lam, E. T., and Revet, I. (2009) Disorders of nucleotide excision repair: the genetic and molecular basis of heterogeneity, *Nat Rev Genet* 10, 756-768.
15. Prakash, S., and Prakash, L. (2000) Nucleotide excision repair in yeast, *Mutat Res* 451, 13-24.
16. Boon, E. M., Ceres, D. M., Drummond, T. G., Hill, M. G., and Barton, J. K. (2000) Mutation detection by electrocatalysis at DNA-modified electrodes, *Nat Biotechnol* 18, 1096-1100.
17. Liu, T., and Barton, J. K. (2005) DNA electrochemistry through the base pairs not the sugar-phosphate backbone, *J Am Chem Soc* 127, 10160-10161.

18. Boal, A. K., and Barton, J. K. (2005) Electrochemical detection of lesions in DNA, *Bioconjug Chem* 16, 312-321.
19. Slinker, J. D., Muren, N. B., Renfrew, S. E., and Barton, J. K. (2011) DNA charge transport over 34 nm, *Nat Chem* 3, 228-233.
20. Ito, K., and Inaba, K. (2008) The disulfide bond formation (Dsb) system, *Curr Opin Struct Biol* 18, 450-458.
21. Vlamis-Gardikas, A. (2008) The multiple functions of the thiol-based electron flow pathways of Escherichia coli: Eternal concepts revisited, *Biochim Biophys Acta* 1780, 1170-1200.
22. Winterbourn, C. C., and Hampton, M. B. (2008) Thiol chemistry and specificity in redox signaling, *Free Radic Biol Med* 45, 549-561.
23. Gorodetsky, A. A., Dietrich, L. E., Lee, P. E., Demple, B., Newman, D. K., and Barton, J. K. (2008) DNA binding shifts the redox potential of the transcription factor SoxR, *Proc Natl Acad Sci U S A* 105, 3684-3689.
24. Lee, P. E., Demple, B., and Barton, J. K. (2009) DNA-mediated redox signaling for transcriptional activation of SoxR, *Proc Natl Acad Sci U S A* 106, 13164-13168.
25. Nunez, M. E., Noyes, K. T., and Barton, J. K. (2002) Oxidative charge transport through DNA in nucleosome core particles, *Chem Biol* 9, 403-415.
26. Nunez, M. E., Holmquist, G. P., and Barton, J. K. (2001) Evidence for DNA charge transport in the nucleus, *Biochemistry* 40, 12465-12471.

27. Gorodetsky, A. A., Ebrahim, A., and Barton, J. K. (2008) Electrical detection of TATA binding protein at DNA-modified microelectrodes, *J Am Chem Soc* 130, 2924-2925.
28. Boal, A. K., Genereux, J. C., Sontz, P. A., Gralnick, J. A., Newman, D. K., and Barton, J. K. (2009) Redox signaling between DNA repair proteins for efficient lesion detection, *Proc Natl Acad Sci U S A* 106, 15237-15242.
29. Boal, A. K., Yavin, E., Lukianova, O. A., O'Shea, V. L., David, S. S., and Barton, J. K. (2005) DNA-bound redox activity of DNA repair glycosylases containing [4Fe-4S] clusters, *Biochemistry* 44, 8397-8407.
30. Gorodetsky, A. A., Boal, A. K., and Barton, J. K. (2006) Direct electrochemistry of endonuclease III in the presence and absence of DNA, *J Am Chem Soc* 128, 12082-12083.
31. Romano, C. A., Sontz, P. A., and Barton, J. K. (2011) Mutants of the base excision repair glycosylase, endonuclease III: DNA charge transport as a first step in lesion detection, *Biochemistry* 50, 6133-6145.
32. Sontz, P. A., Mui, T. P., Fuss, J. O., Tainer, J. A., and Barton, J. K. (2012) DNA charge transport as a first step in coordinating the detection of lesions by repair proteins, *Proc Natl Acad Sci U S A* 109, 1856-1861.

Chapter 2

ATP-stimulated, DNA-mediated redox signaling by XPD, a DNA repair and transcription helicase

Adapted from Mui, T.P., Fuss, J.O., Ishida, J.P., Tainer, J.A., Barton, J.K. "ATP-stimulated, DNA-mediated redox signaling by XPD, a DNA repair and transcription helicase" *J. Am. Chem. Soc.* **2011** 133(41) 16378-81

T.P.M. performed protein electrochemistry. J.O.F. and J.P.I. generated protein and performed biochemical characterizations.

Introduction

To protect the genome, a variety of proteins with various functions must act in concert.¹⁻³ One such protein, XPD, is a super family 2 helicase critical to nucleotide excision repair (NER) and important to transcription.⁴⁻⁶ Helicases are responsible for unwinding DNA in an ATP-dependent fashion in order to access individual bases, allowing the other proteins to repair DNA damage, and to both replicate and transcribe DNA. In humans, XPD is part of the TFIIH machinery, with single site mutations leading to human diseases with increased cancer risk or premature aging: Xeroderma Pigmentosum (XP), Cockayne Syndrome (CS), Trichothiodystrophy (TTD), or combinations thereof.^{4,5,7} Recent chemical analyses and crystal structures of archaeal XPD homologues, which have ~22% sequence identity with the human homologue, reveal the presence of a [4Fe-4S] cluster.⁸⁻¹⁰ Furthermore, combined structural, biochemical, and mutational analyses reveal that the catalytic core of XPD is conserved from archaea to humans and has functional relevance for understanding human disease.⁵ Mutational analyses of [4Fe-4S] coordinating cysteines have established the importance of the [4Fe-4S] cluster in DNA unwinding activity,¹⁰⁻¹² yet a role for XPD as a redox-active protein remains to be established.

DNA charge transport (CT), in which electrons are transferred between proteins bound to DNA in a path through the DNA bases, has been proposed as a first step in the localization of a family of base excision repair (BER) proteins containing [4Fe-4S] clusters in the vicinity of damage.¹³ DNA CT chemistry facilitates electron transfer over long molecular distances through the DNA duplex^{14,15} but is remarkably sensitive to perturbations in base pair stacking, as, for example, arise with damage.^{16,17}

DNA-mediated CT signaling by proteins was first explored in studies of a class of *E. coli* BER glycosylases that contain [4Fe-4S] clusters.^{18,19} Electrochemistry on DNA-modified electrodes showed that DNA binding shifts the cluster potential to ~80 mV, well within the physiological range for redox signaling. Biophysical experiments were then used to examine the redistribution of BER enzymes in the vicinity of damage, and genetic experiments were used to explore cooperative signaling between two BER enzymes, endonuclease (Endo) III and MutY.^{20,21} These results in combination with DNA electrochemistry connects the relocalization of Endo III (i) near a DNA mismatch (ii) to cooperate in helping MutY repair lesions *in vivo*, and (iii) to carry out DNA CT. If CT is generally important for DNA repair, we hypothesized it should be detected in repair pathways besides BER, including NER, which is the major pathway for chemically modified bases that disrupt the DNA double helix.

Materials and Methods

Chemicals were purchased from Sigma Aldrich. All reagents for DNA synthesis were purchased from Glen Research. Gold on mica was purchased from Agilent Technologies.

DNA Synthesis

DNA Sequences were synthesized using standard phosphoramidite chemistry at either IDT DNA (Coralville, IA) or on an Applied Biosystems 3400 DNA synthesizer. Thiol additions were introduced using disulfide phosphoramidites (Glen Research), which were subsequently reduced prior to experiment. All oligonucleotides were purified by HPLC and confirmed by mass-spec.

DNA Modified Electrodes

DNA modified electrodes were prepared as previously described. Briefly, a 50 μ L solution of 50 mM duplex DNA (as determined by UV-Vis) was incubated on a bare gold-on-mica surface at 4°C overnight. Free DNA was subsequently removed through rinsing of the surface a minimum of three times with phosphate buffer (5 mM phosphate, 50 mM NaCl, pH 7.0). Next, 50 μ L of a 1 mM 6-mercaptop-1-hexanol solution in protein buffer was used to passivate the surface at ambient temperature for 2 hours. Finally, the surface was rinsed a minimum of three times with protein buffer.

Protein Expression

The *Sulfolobus acidocaldarius* XPD expression construct as described² was modified to improve expression by removing a frame-shifting ATG start codon between the RBS and the correct start codon. Mutants were then generated using Quikchange XL II kit (Stratagene) and verified by sequencing. All proteins were expressed in BL21

Rosetta2 *E. coli* cells (Invitrogen) grown in Terrific Broth at 37°C for 3 hours after induction with 0.2 mM IPTG. Cells were resuspended in 20 mM MES pH 6, 100 mM NaCl, 1 mM DTT, 1 mM EDTA and lysed by sonication and constant cell disruptor (Constant Systems) at 20,000 psi. After centrifugation at 29,000 RCF for 30 min, the supernatant was heat treated (65°C, 20 min), centrifuged as before, and incubated with Capto DEAE (GE Healthcare) for 10-20 min at room temperature. The flow-through was collected by gravity and loaded onto a 5 mL HiTrap Heparin (GE Healthcare) column at 2 mL/min. Bound protein was washed (7 column volumes) with lysis buffer and eluted with a linear gradient (7 column volumes) to 45% high salt buffer (20 mM MES pH 6, 1 M NaCl, 1 mM DTT, 1 mM EDTA). SaXPD-containing fractions (~36% high salt buffer) were pooled, concentrated using Amicon Ultra, Ultracel-10k regenerated cellulose spin filters, and fractionated on a HiLoad 16/60 Superdex200 (GE Healthcare) size exclusion column at 1 mL/min in 10.8% high salt buffer (200 mM NaCl final). SaXPD-containing fractions were pooled, concentrated as above to 2-12 mg/mL by OD₂₈₀, and frozen. All cell and protein manipulations were carried out at 4°C unless otherwise noted, buffers were filtered and degassed, and purification was carried out in one day when possible to limit oxygen exposure.

Prior to electrochemical measurements, proteins were dialyzed against the protein buffer (20 mM Phosphate, 100 mM NaCl, 1 mM EDTA, 5% glycerol, pH 7.5) to remove residual DTT. The concentration of individual proteins was determined by UV-Vis using $\epsilon=17,000 \text{ M}^{-1}$ at 410 nM for the [4Fe-4S] cluster. For a representative trace, see Figure 2.8. The majority of the protein work was conducted in an oxygen-free environment to prevent degradation of the [4Fe-4S] cluster.

Protein Electrochemistry

Electrochemistry was performed as previously described¹ with modifications indicated. Measurements were obtained in an oxygen-free atmosphere using a CH Instruments 620C electrochemical analyzer. A Au (111) surface served as the working electrode with a platinum wire auxiliary. Ag/AgCl (Basi Electrodes) electrode was modified with a 4% agarose gel tip to serve as the reference. The 3-electrode setup was placed in a humidifier box filled with degassed water to prevent evaporation of the protein from the electrode. Protein was added in aliquots of 40-50 μ L with concentrations as indicated.

Both ATP and ATP- γ -S were purchased from Sigma and dissolved in protein storage buffer to make 100 mM stock solutions that were subsequently degassed with argon. For ATP and ATP- γ -S additions, the appropriate degassed stock solution was added and mixed by pipetting.

For data analysis, current values were obtained by averaging the reductive sweep of a CV after linear base line corrections. After equilibration on the surface, a linear fit was used as the background current. The value of the current was then subtracted from the background current to obtain the difference in current. This value was then normalized to the surface by dividing by the background current to obtain the % difference in current. From the % difference in current data, 1st order kinetics were plotted to fit the parameters yield=1-e^{-kt}.

Biochemical Assays

Helicase assays were performed as described² with the following modifications. 100 nM 5'-FAM-labeled DNA substrate and 50-500 nM XPD was used. Gels were

visualized and quantified using aVersaDoc MP 4000 Molecular Imager and Quantity One software, respectively (BioRad).

ATPase assays were carried out under the same conditions as the helicase assays, except that unlabeled ssDNA (25-mer from helicase substrate) was used and the total reaction volume was 50 μ L. The amount of phosphate released was measured using Biomol Green Reagent (Enzo Life Sciences) according to the manufacturer's instructions in 96-well plates on an Infinite M1000 microplate reader (Tecan).

SaXPD-DNA binding interactions were measured by fluorescence anisotropy (FA) as described² with the following modifications: 20 nM substrate was used, reactions were incubated for 15 min, and FA was measured in 384-well plates using an Infinite M1000 microplate reader (Tecan).

Results and Discussion

To determine if DNA CT might occur with XPD, we first found the DNA-bound redox potential of an archaeal XPD on DNA-modified gold electrodes (Figure 2.1 see Supporting Information for Methods). We found that XPD from the thermophile *Sulfolobus acidocaldarius* (SaXPD) has a DNA-bound redox potential of $\sim 82 \pm 10$ mV versus NHE (Figure 2.1). This potential, like those found in BER proteins, reflects physiological redox activity and is not sufficient to damage DNA.¹⁸ Additionally, when a mismatch is introduced into the DNA duplex, the redox signal is significantly attenuated, consistent with the electrochemical protein signal being DNA-mediated (Figure 1).¹⁶ We also observed that the signal intensity exhibits a linear dependence on the square root of the scan rate, which implies that the protein is binding to DNA in a diffusion-limited process.²² In addition, we observed an electron transfer rate of approximately 1.4 s^{-1} based on Laviron analysis, a similar value to previously published rates, indicating that the rate of electron transfer is limited by tunneling through the carbon linker.²³ Together these data establish that this DNA-mediated signal corresponds to the one-electron redox couple of the [4Fe-4S] cluster of SaXPD bound to DNA, and that this redox couple can be physiologically active.

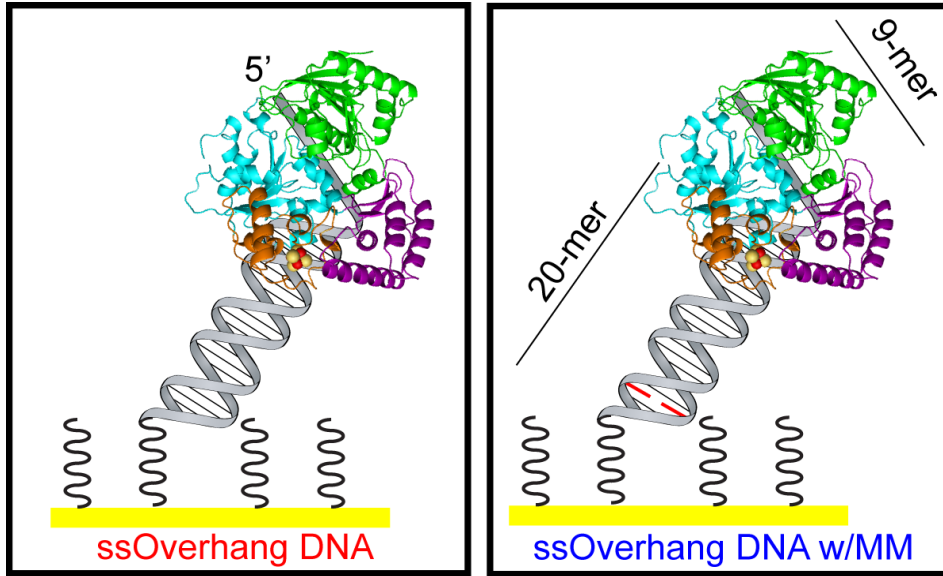


Figure 2.1 Cartoon Schematic of well-matched DNA with a 9 nucleotide single-stand overhang (left) and DNA with a CA mismatch (MM) (right).

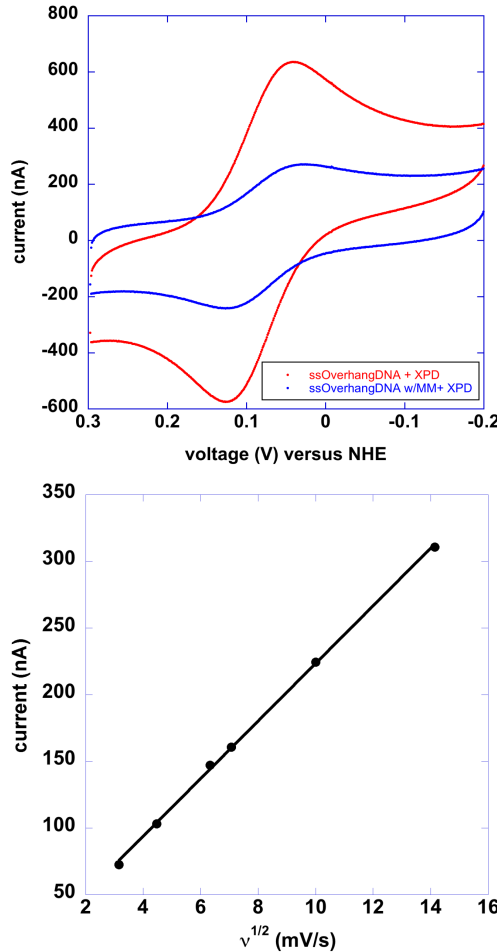


Figure 2.2. Electrochemistry of DNA-bound WT SaXPD. (Top) Cyclic voltammogram (CV) of SaXPD [120 μ M] on a well-matched DNA-modified electrode (red) and on DNA with a CA mismatch located near the gold surface as in Scheme 1 (blue). (Ag/AgCl reference electrodes; Pt auxiliary electrode, 50 mV/s scan rate, NHE = normal hydrogen electrode). (Bottom) Plot of current versus $v^{1/2}$ (square root of scan rate). The data indicate that our signal is obtained through a diffusion-limited process.

Unlike BER glycosylases, the principal activity of the XPD helicase is ATP-dependent, and as such, the effect of ATP on the DNA-bound signal could also be investigated. After the protein was allowed to equilibrate on the DNA-modified surface, various concentrations of ATP or ATP- γ -S (a markedly slower to hydrolyze ATP analogue) were added (Figure 2.2, 2.5).²⁴ Interestingly, as ATP was titrated onto the surface, a noticeable ATP-dependent increase in the current was observed. No shift in potential was evident, indicating that the cluster is neither degraded nor markedly changed in its environment, and coupling to the DNA π -stack appears to increase.

In contrast, the non-hydrolysable ATP analogue has little effect on the electrochemical signal of the protein, indicating that the electrochemical signal reports on the ATPase activity of XPD. The sensitivity of the signal to ATP hydrolysis is remarkable given that, based on the crystal structure of the protein not bound to DNA, the distance between the cluster and the ATP binding site is 30 Å.¹⁰ However, in the XPD structure, the [4Fe-4S] cluster domain is tightly linked to the ATP binding site by β -sheets that could provide a mechanism for mechanical coupling associated with motion between the cluster domain and the ATP site during hydrolysis. The increase in electrochemical signal is likely reporting on motions at the protein/DNA interface as the protein carries out ATP hydrolysis.

We additionally examined the effect of the DNA substrate (Figures 2.3 and 2.4), as XPD has shown a preference as a 5'-3' helicase.²⁵ Modeled on a surface, the 5'-3' helicase would be expected, therefore, to move downward towards the surface. As protein concentration is well above the dissociation constant (46 nM),¹⁰ it should bind DNAs with either 3'- or 5'-overhangs, as well as duplex DNA. Indeed, we see differences

in the DNA electrochemistry based on substrate. When protein is placed on the surface modified with DNA with a 3' ssDNA overhang, the signal increases temporarily, likely reflecting increased coupling, but then decreases over time. The decay may result from the protein sliding off the DNA-bound surface. Notably, the absolute signal could not be compared among the surfaces because of surface coverage variability. On the fully duplexed surface, which has no directionality bias, we see a mixture of behaviors, which is what would be expected for non-specific binding by XPD.

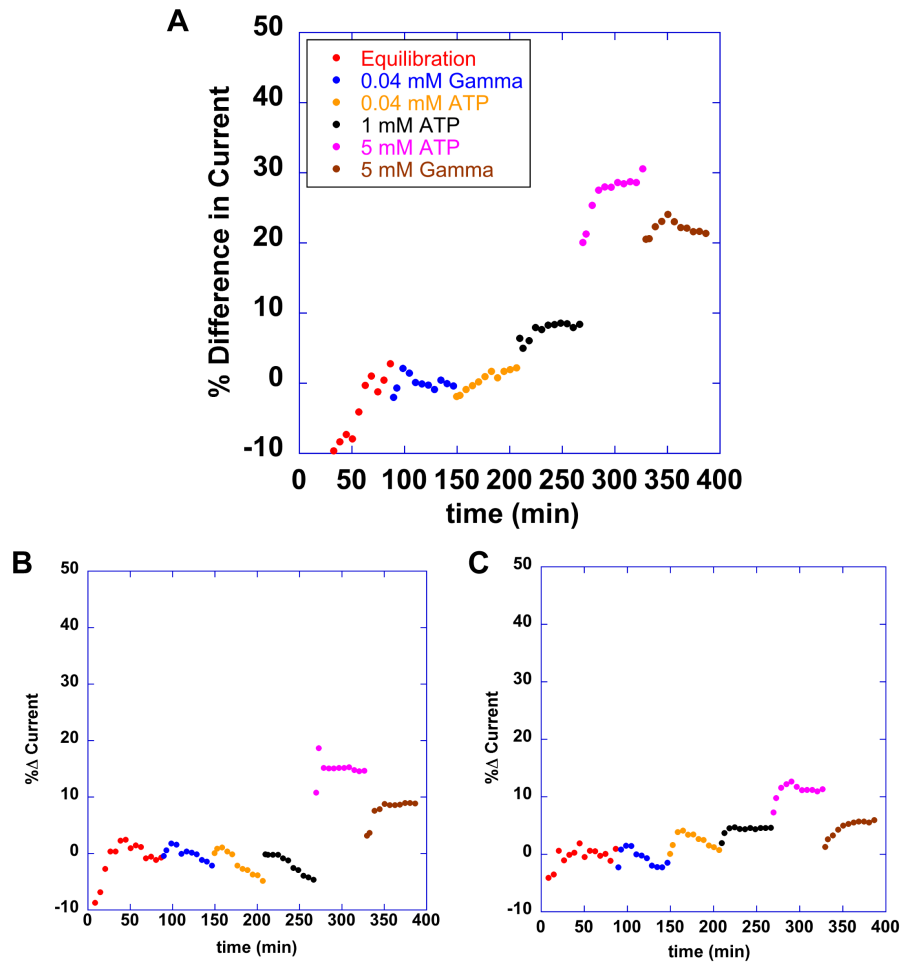


Figure 2.3. ATP-dependent Electrochemistry of SaXPD on different DNA substrates. Time points shown are every 6 minutes. (Ag/AgCl reference electrode; Pt auxiliary electrode, 50 mV/s scan rate). Percent difference in Current for SaXPD [9 μ M] on a 5'-ssDNA overhang (A), 3'-ssDNA overhang (B), fully duplexed DNA (C). The signal is ATP-dependent and sensitive to substrate. Note at the high concentration addition [5 mM ATP- γ -S], some ATP still remains, as once depleted, the signal levels off.

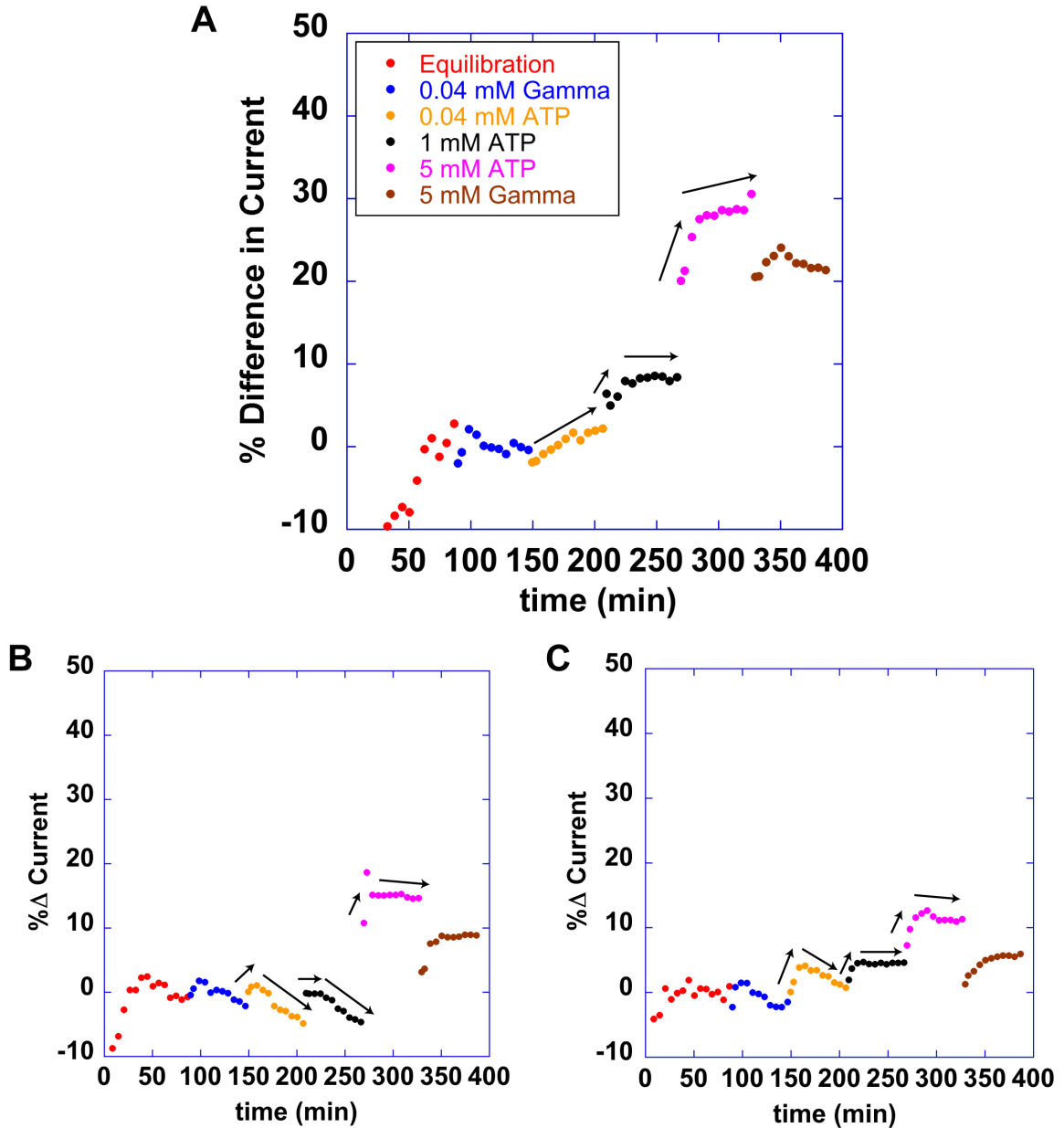


Figure 2.4 Plots as shown in Figure 2.3. Arrows have been included during the ATP additions to indicate an initial phase as well as the evolution of the signal with ATP hydrolysis.

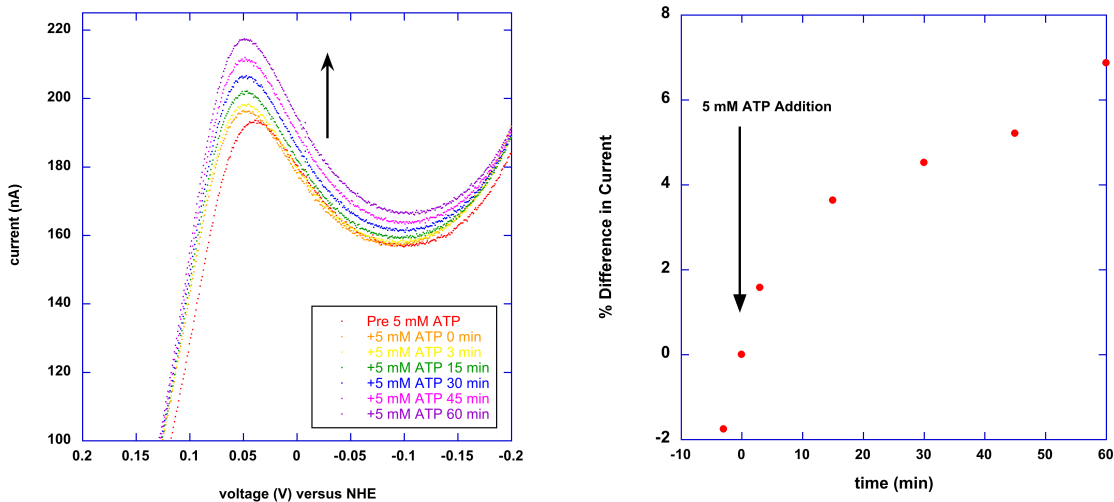


Figure 2.5. ATP-dependent signal increase with 5 mM ATP addition. Cathodic sweep of CVs for SaXPD [10 μ M] on DNA modified electrodes pre and post [5 mM] ATP addition (left). % difference in current versus time for SaXPD on DNA modified electrodes (right). The arrow on the right indicates addition of 5 mM ATP. Currents were obtained through averaging of the reductive sweep of the various voltammograms (Ag/AgCl reference electrode; Pt auxiliary electrode, 50 mV/s scan rate).

XPD mutations in humans are associated with several often fatal diseases, including XP, CS, and TTD.^{4,5,7} One such mutant, G34R, shows attenuated ATPase and helicase activity relative to wild type (WT) protein in biochemical assays. Interestingly, this SaXPD mutant exhibits a redox signal comparable to that of WT in the absence of ATP (Table 2.1). However, the rate of electronic signal increase with ATP for the G34R mutant is significantly lower compared to WT, further demonstrating the sensitivity of our assay to ATP hydrolysis (Figure 2.6). While there is certainly not a simple linear relationship between activity measured electrically and biochemically, the electronic signal appears to be a sensitive reporter of changes in protein/DNA coupling that result from ATP hydrolysis during the initial time following ATP addition. This assay complements a fluorescence helicase assay seen earlier, but without the need for DNA labeling.²⁶

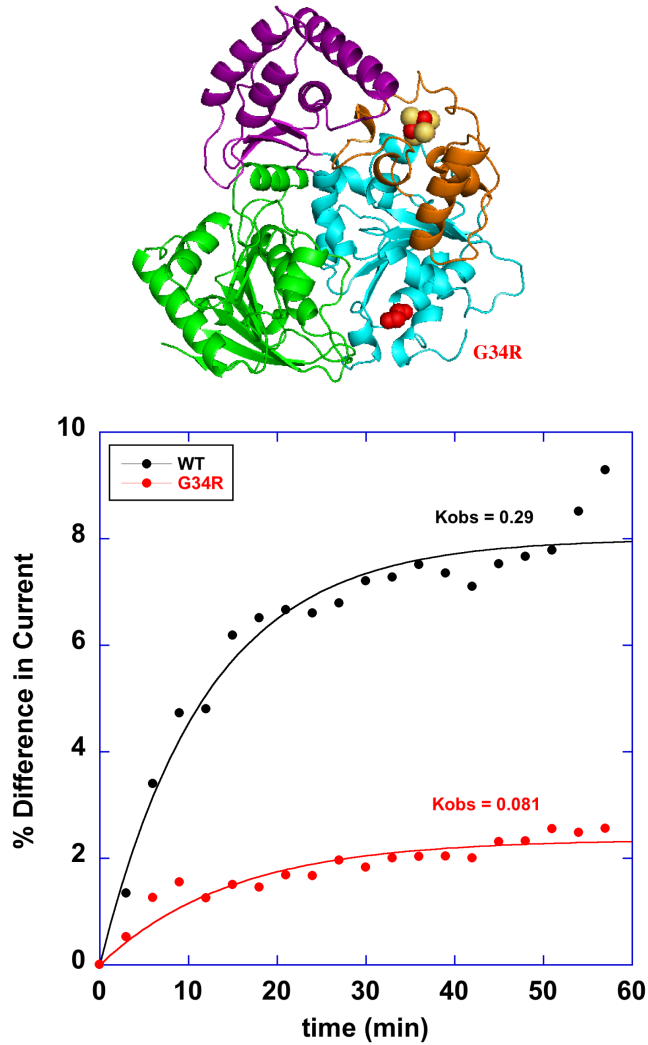


Figure 2.6. Electrochemical comparisons of SaXPD mutants after 5 mM ATP addition. (Top) Crystal structure of SaXPD with residues that were mutated shown in space filling model. Also shown in space filling models is the [4Fe-4S] cluster (Bottom), ATP-dependent CT of WT (black), and G34R (red). Observed initial rate constants (min^{-1}) of 0.29 and 0.08 for WT and G34R.

Mutant	Redox Signal Intensity	Helicase (bp/min)	ATPase (mol/sec)	ssDNA Kd (nM)
WT	1	20.5 ± 0.7	1.24 ± 0.03	66 ± 5
G34R	1.2 ± 0.09	0.8 ± 0.1	0.0 ± 0.01	67 ± 3

Table 2.1. Redox and Biochemical activity of WT and G34R XPD.

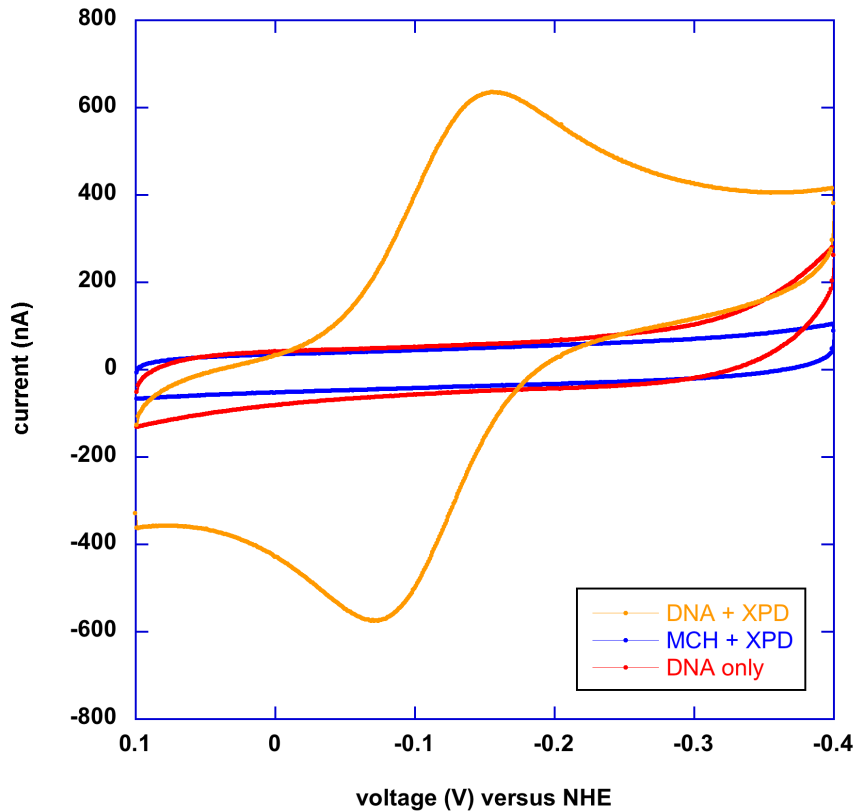


Figure 2.7. Electrochemistry of SaXPD on control surfaces. Electrochemistry of SaXPD on a DNA modified electrode backfilled with mercaptohexanol (orange), on a mercaptohexanol only electrode (blue) and without SaXPD on a DNA modified electrode (red) (Ag/AgCl reference electrode; Pt auxiliary electrode, 50 mV/s scan rate). These data indicate that this is a DNA-mediated process.

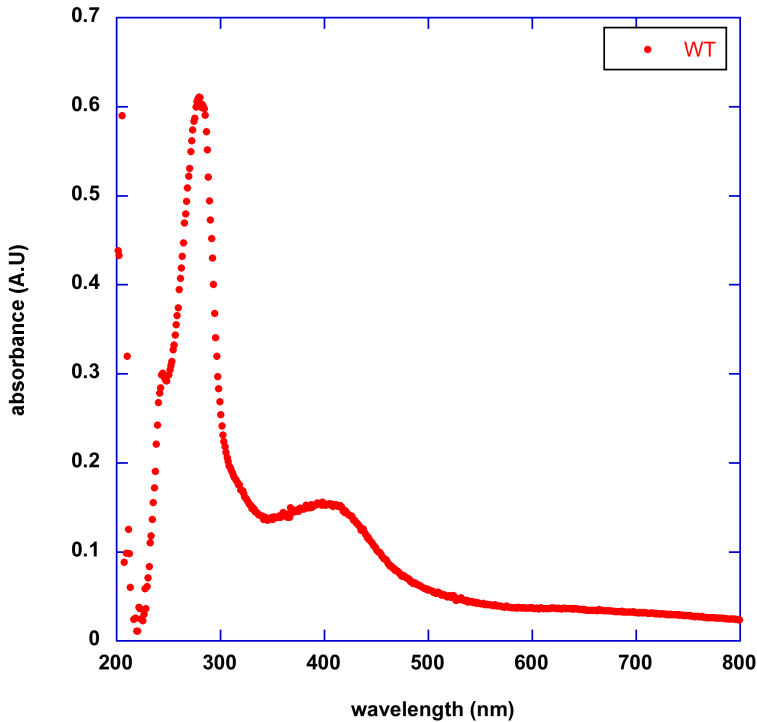


Figure 2.8. UV-Vis spectrum of WT SaXPD. The shoulder at 410 nm, is indicative of a [4Fe-4S] cluster and is used for determining the concentration of the XPD mutants.

Magnesium addition enhances ATP-dependent DNA-mediated signaling

SaXPD has exhibited a small dependence of ATPase activity on magnesium content. As such, we tested the effect of Mg²⁺ on ATP hydrolysis. Divalent cations typically serve to stabilize the hydrolyzed ATP intermediate and therefore facilitate cleavage of the triphosphate. Similar to our ATPase assay, SaXPD was incubated on a surface and ATP was titrated in small increments. After the ATP additions, 2 mM MgCl₂ was added, and CVs were taken every three minutes. Our results in Figure 2.9 show that the addition of magnesium does in fact increase the redox active signal on the surface. This result demonstrates that the ATP-dependent DNA-mediated signaling has a small magnesium dependence. However, due to assay constraints magnesium was omitted, as it provides only a negligible increase in the signal.

SaXPD incubation on the surface

To verify that the observed signal increase was due only to the addition of ATP or ATP-γ-S, SaXPD was incubated on a DNA modified electrode for 7 hours, the time course of the ATP titration assay. CVs were again taken every three minutes, and the data are shown in Figure 2.12. Throughout the time course of the experiment there is little to no deviation from the linear increase in the signal, which is used as a background correction for all subsequent experiments. Interestingly, even when the reference electrode is removed from solution and re-inserted, no increase in the redox signal is observed (data not shown).

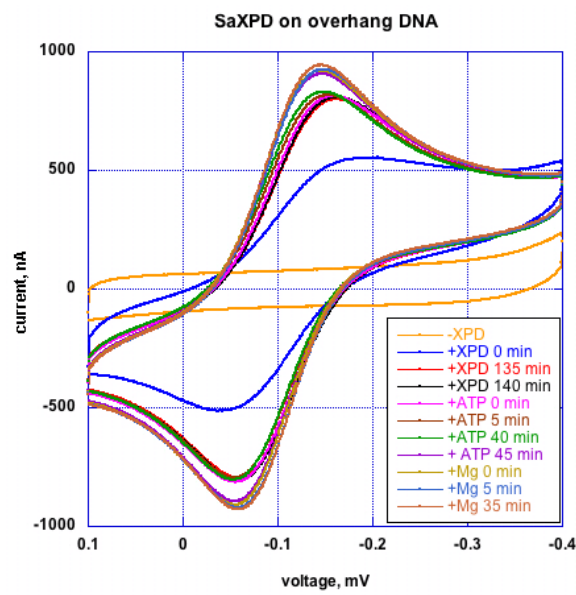


Figure 2.9 SaXPD on a DNA-modified electrode with ATP and magnesium additions.

SaXPD optimal substrate determination

Helicases are responsible for unwinding the DNA and physically separating the complementary strands of DNA. As a helicase, SaXPD has a substrate preference for ssDNA overhangs. In the past, DNA-modified electrodes assembled in the Barton lab focused on fully matched duplexes with either mismatches or different DNA damage products. By utilizing a ssDNA overhang, we hypothesized that we would generate a preferred substrate for SaXPD and target the protein to the surface. As shown in Figure 10, we assembled a variety of DNA-modified electrodes and found that on a 9 nucleotide 5' ssDNA overhang we observed the largest signal. Interestingly, on all of the substrates assayed we observed a redox signal. This is attributed to the excess protein relative to the amount of DNA. While the surface coverage is approximately 50 pmol/cm², we observed non-specific DNA binding from the helicase.

Optimizing protein concentration for electrochemical ATPase assay

Initial electrochemistry experiments required large concentrations (greater than 100 μM) of protein to observe a redox active couple and verify that the observed protein signal was DNA-mediated. When SaXPD was incubated on the electrode for 30 mins., signals of a few hundred nanoamps (nA) were observed. (Figure 2.11) Upon 5 mM ATP addition, the signal increase was quite negligible, only about 5%. (Figure 2.11) As a result, it was necessary to decrease the protein concentration on the surface to observe a greater increase in signal upon ATP addition. Experiments were performed under varying SaXPD concentrations ranging from 2, 10, 40 and 160 μM, after which the protein was allowed to incubate for 90 mins., followed by three 60 min. titrations of 40 μM, 1 mM, and 5 mM ATP. As shown in Figure 2.11, the optimal signal increase

occurred at 10 μM SaXPD. (Figure 2.11). Based on this data, all further experiments utilized 10 μM as the protein concentration.

Duplex	Sequence
Duplex DNA	SH 5' — GTGCTGCAACGTGTCTGCGC — 3' 3' — CACGACGTTGCACAGACGCG — 5'
Overhang DNA	SH 5' — GTGCTGCAACGTGTCTGCGC — 3' 3' — CACGACGTTGCACAGACGCGAGAGCAGAC — 5'
Overhang DNA w/MM (high)	SH 5' — GTGCC <u>C</u> GCAACGTGTCTGCGC — 3' 3' — CACGACGTTGCACAGACGCGAGAGCAGAC — 5'
Reverse DNA	SH 5' — CACGACGTTGCACAGACGCGAGAGCAGAC — 3' 3' — GTGCTGCAACGTGTCTGCGC — 5'

Table 2.2. Representative table of DNA duplexes utilized

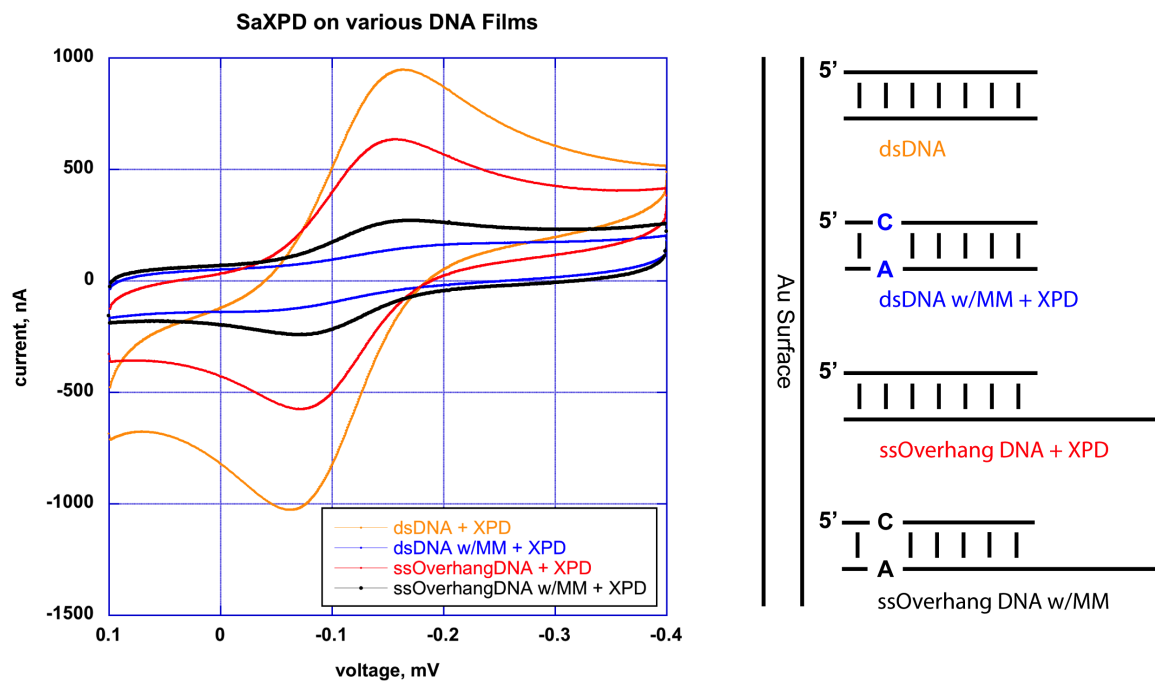


Figure 2.10 SaXPD on various DNA films. CVs of SaXPD [$\sim 120 \mu\text{M}$] on various DNA modified electrodes as shown on the right. In each case, the midpoint redox potential of the SaXPD protein is $\sim 80 \text{ mV}$ versus NHE. (shown versus Ag/AgCl). Also note that in each case of the C:A mismatch, that the redox signal is significantly attenuated relative to the well-matched sequence, suggesting that the redox signal is DNA-mediated.

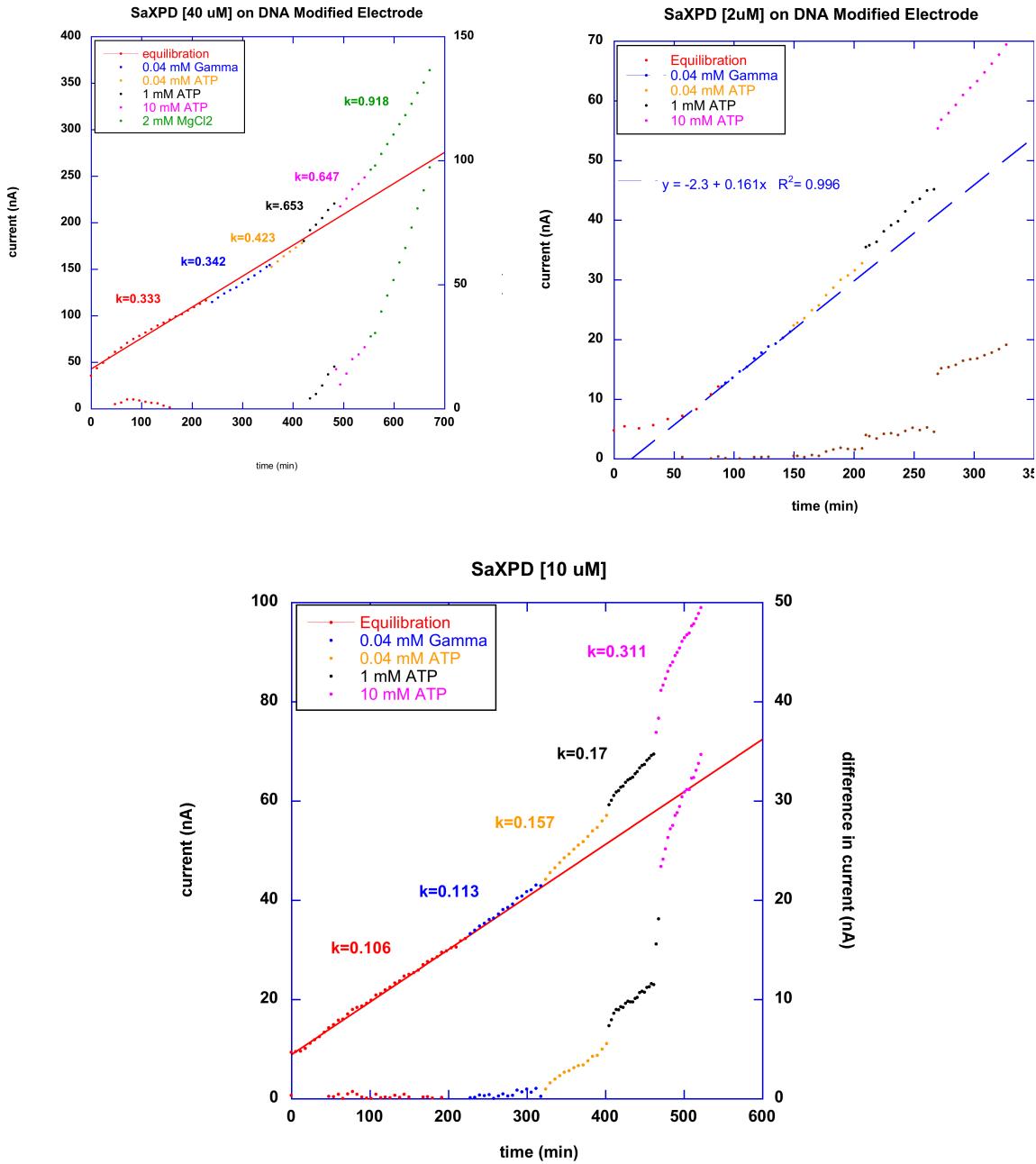


Figure 2.11. Concentration dependent signaling of SaXPD on a DNA-modified electrode. From top left clockwise SaXPD [40 μM , 2 μM , and 10 μM] on a DNA modified electrode with a 5' ssDNA overhang. In each case the protein was allowed to equilibrate, followed by titrations of ATP- γ -S and ATP. The top curves in each plot represent the raw current value obtained from the CV, while the bottom curves depict the change in current when background corrected. Note at 10 μM SaXPD exhibits the largest increase in signal when ATP is added.

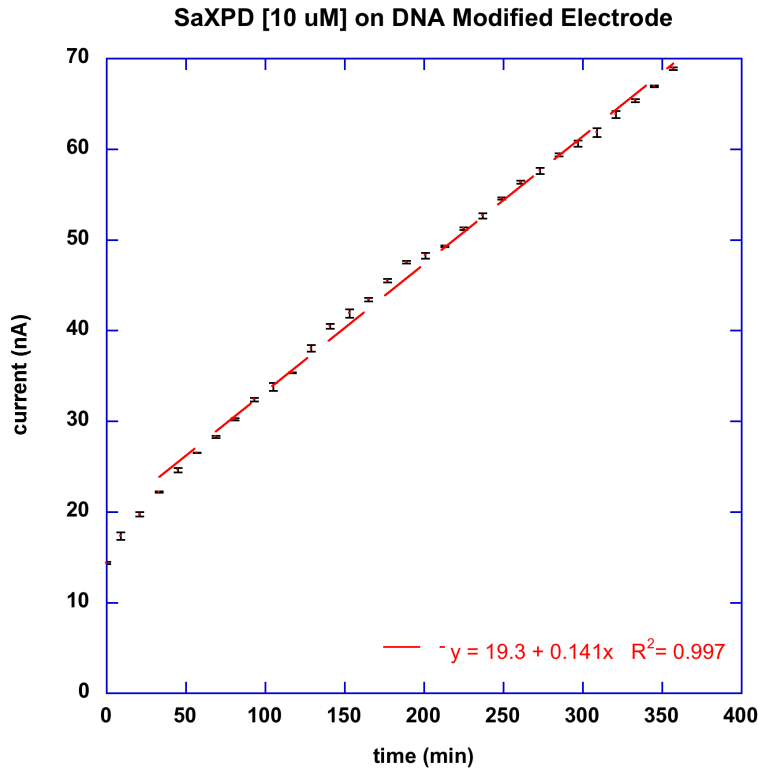


Figure 2.12 Stability of SaXPD on a DNA-modified electrode. SaXPD [10 μM] was incubated on a 5'-ssDNA overhang modified electrode for 6 hours with CVs taken every 3 minutes. Shown are the value of the currents from the reductive sweep over that same period. Note the linear increase in signal of the protein over 6 hours. This serves as a background correction in all future experiments.

Endonuclease III ATPase titration

Endonuclease III (EndoIII) has been extensively studied in our lab. It was one of the first proteins identified to contain a [4Fe-4S] cluster and is capable of a DNA-bound reduction potential. As a glycosylase, EndoII is responsible for cleaving a mispaired adenine opposite a guanine. Therefore it lacks ATP-dependent helicase activity and is a great control for our reaction to verify that we are in fact observing ATP-dependent helicase activity in SaXPD. As with our SaXPD experiments, EndoIII was incubated on the surface and followed by increasing titrations of first ATP- γ -S and ATP. The redox signal grew in over time as expected with low-concentration proteins on DNA-modified electrodes (Figure 2.12); however, during each of the additions no noticeable increase was observed (Figure 2.12). This verified that the increase in DNA mediated signaling observed with SaXPD was in fact a result of the SaXPD activity and not of the chemical additives.

Bulk Electrolysis of SaXPD on DNA-modified electrodes

SaXPD exhibits similar redox properties as the previously reported BER proteins. It would be interesting if it too had a change in binding affinity associated with the redox state of the cluster. This would allow SaXPD to signal other proteins through DNA-mediated CT as proposed in the BER model. To assay this, SaXPD was incubated on a DNA-modified electrode until the signal remained constant. After equilibration, a fully reducing potential (-350 mV) was applied for 5 minutes and a CV was taken immediately after the bulk electrolysis. As shown in Figure 2.13, we observed an increase in signal by 10%. The reverse was also performed; a fully oxidizing potential (50 mV) was again held for 5 minutes and a CV was immediately taken following the bulk electrolysis. Here the signal decreased by 5%, suggesting that in the oxidized state, the protein has a higher

binding affinity for DNA than that in the reduced state, comparable with previously reported results for the EndoIII protein.

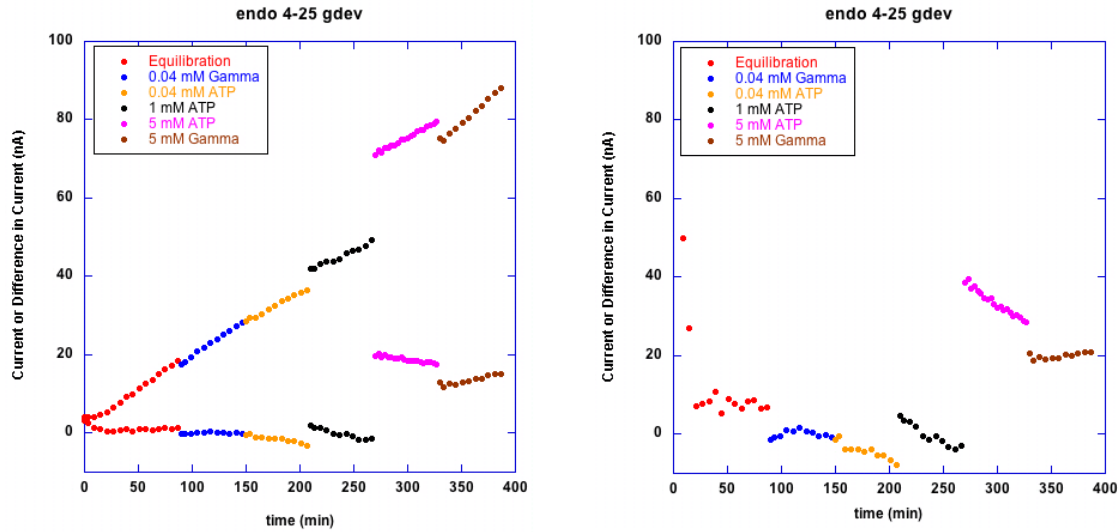


Figure 2.13 Endonuclease III ATP-dependence. Not all [4Fe-4S] cluster-containing redox active proteins demonstrate ATP-dependent signaling. EndoIII [10 μ M] was incubated on a 5'-ssDNA overhang modified electrode and subject to an ATP and ATP- γ -S titration. (Left) Current or difference in current versus time for the EndoIII protein. (Right) Percent difference in current versus time for the EndoIII protein. Notice that EndoIII signal does not change over time and grows in linearly, as expected with a protein that does not have ATP-dependent signaling. This confirms that our ATP-dependent signaling is unique to SaXPD and not a feature of all [4Fe-4S] cluster-containing proteins.

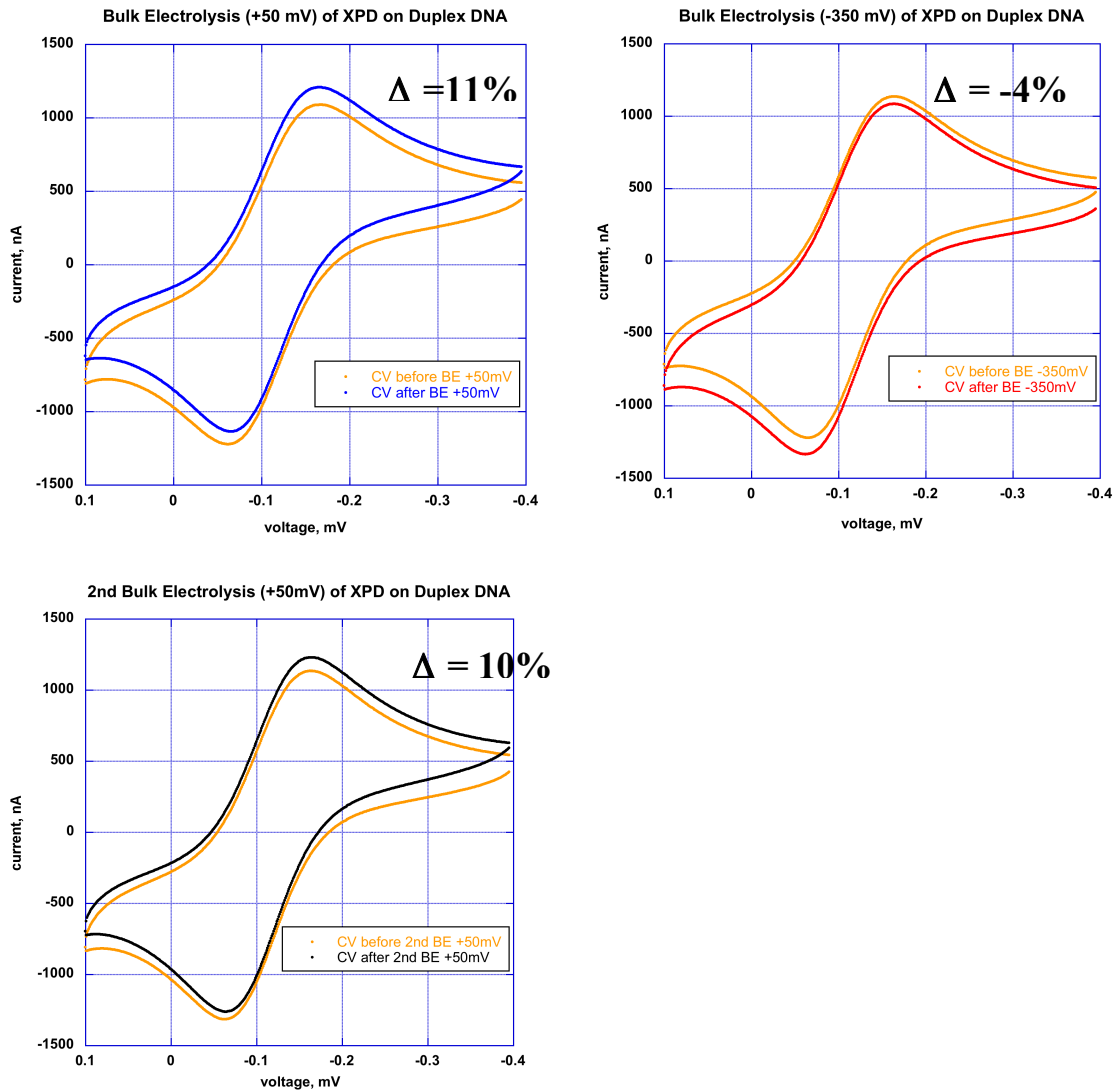


Figure 2.14. Bulk electrolysis of SaXPD. CV after 5 minute Bulk Electrolysis of SaXPD at +50 mV (a), -350 mV (b), and +50 mV (c). The orange curve represents the equilibrium prior to oxidation/reduction of the cluster.

SaXPD on HOPG Electrodes

As a final method of characterization of the SaXPD protein, we attempted to observe both the unbound and DNA-bound redox couples of SaXPD, which would allow for direct comparisons of the DNA-mediated signal and the surface bound signal. DNA binding is thought to alter the potential of the cluster. HOPG is better suited than gold for such measurements, as it can be scanned at a wider variety of potentials without damaging the surface. On HOPG surfaces, pyrene modified DNA was used for self-assembly, with octane as a back-filling agent. However, we were never able to observe a redox couple for SaXPD from a wide range of concentrations (data not shown). Surfaces were verified for integrity using Redmond red and methylene blue, however no protein signal ever emerged. Attempts were made to observe the direct surface reduction of the [4Fe-4S] cluster. Using HOPG without back-filling agent or DNA, we observed a redox signal at approximately -200 mV vs. NHE, which has been previously reported as the 2+/1+ couple. (Figure 2.15) Because of the difficulties in working with this surface, we abandoned attempts to observe the DNA-mediated signal from SaXPD on HOPG.

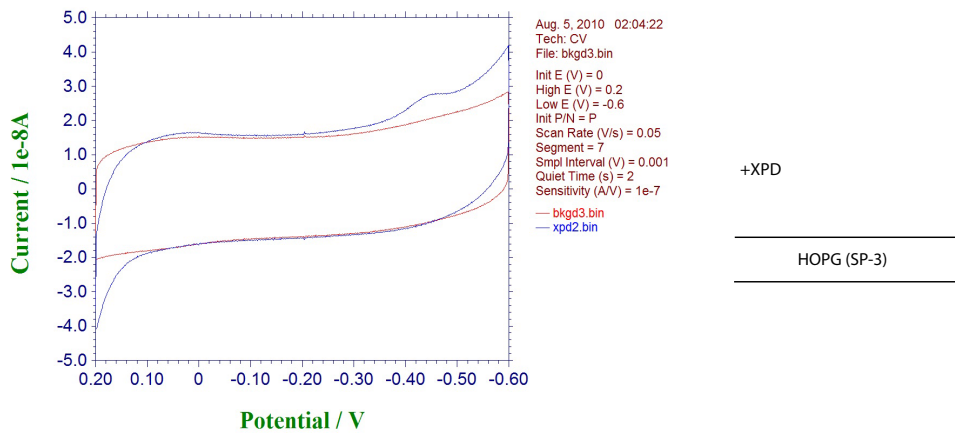


Figure 2.15. CV of SaXPD on bare HOPG. The 2+/1+ irreversible couple can be observed at -450 mV vs. Ag/AgCl.

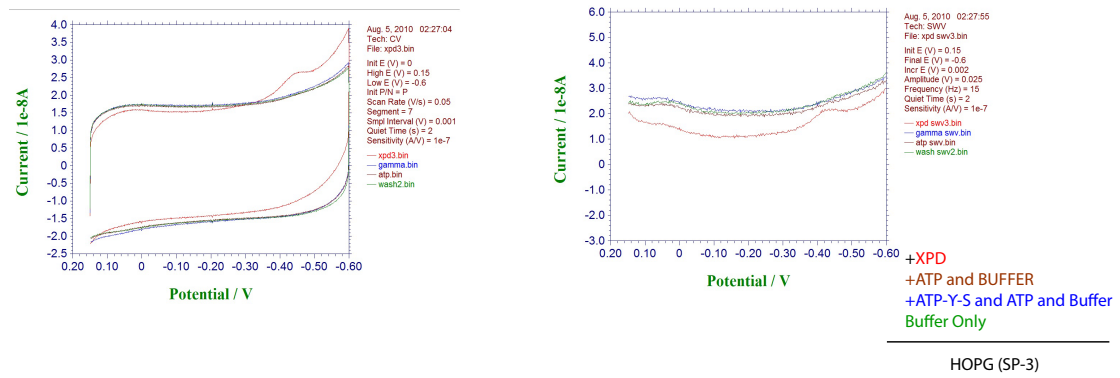


Figure 2.15 Electrochemistry of SaXPD on bare HOPG. CV and Square Waves of SaXPD on bare HOPG (SP-3) showing that none of the individual components such as ATP (brown), ATP- γ -S (blue), or buffer (green) contribute to the irreversible peak observed at -450 mV vs. Ag/AgCl.

Light-activated ATP activation with SaXPD

One of the limitations of our electrochemical ATPase assay is that we must incubate the protein with ATP and it can, and presumably does, hydrolyze the ATP instantaneously. To observe a synchronous ATP-dependent signaling event, we allowed SaXPD to incubate in the dark (to prevent uncaging) with DMPE-ATP, a light-activated caged ATP. Upon irradiation, the DMPE group was removed and ATP exposed. As shown in Figure 2.16, upon irradiation, we saw a large increase in the electrochemical signal. However, this signal is large, erratic, and decays quickly. This experiment was repeated with only DMPE-ATP on a DNA-modified electrode and upon irradiation a similar effect was observed. Therefore, the photo release of the DMPE provides a redox active molecule that interferes with monitoring of the SaXPD DNA-mediated signal. Identification of a photo protected ATP that is not redox active would enable the observation of synchronous signaling by the SaXPD helicase.

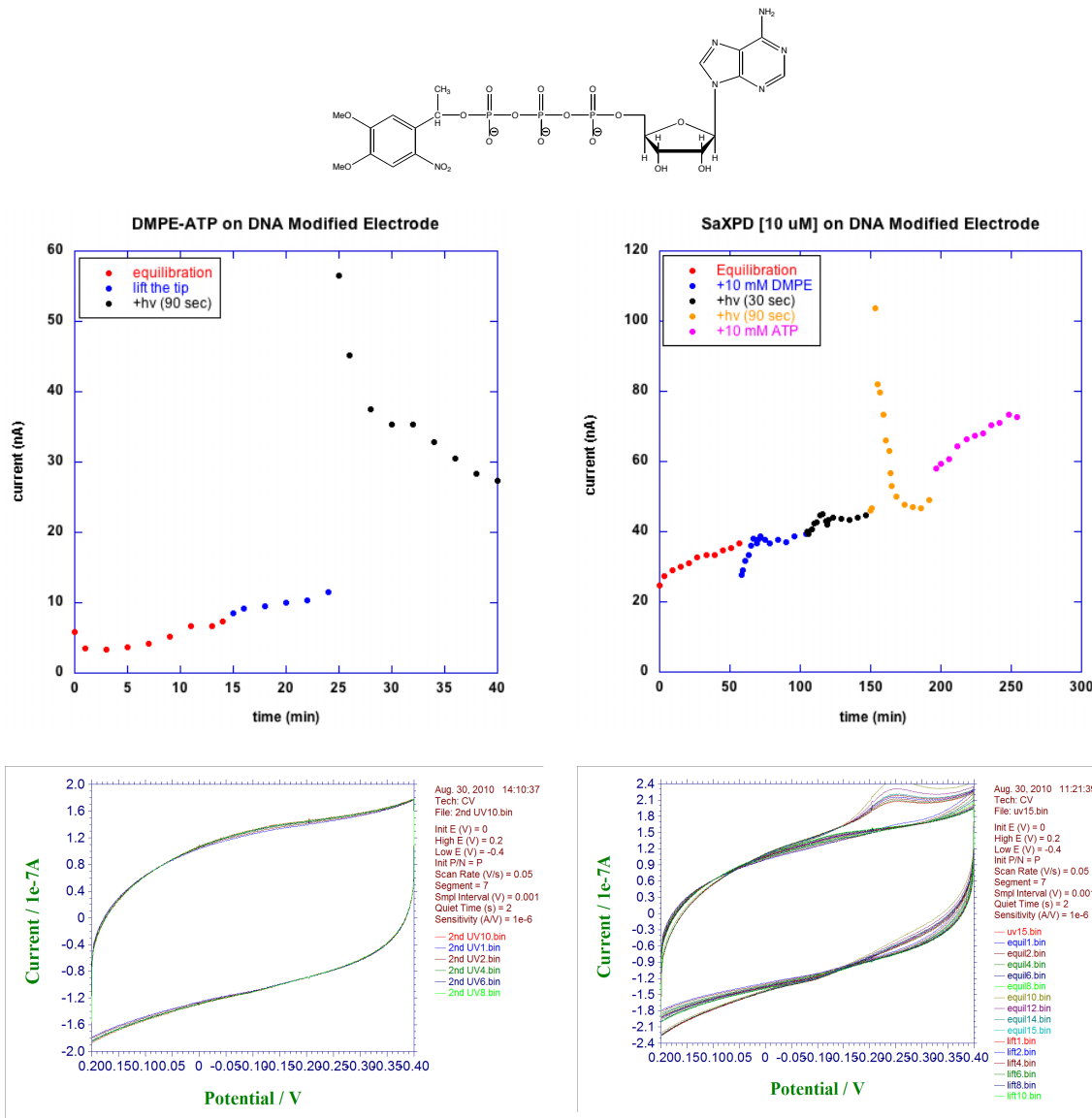


Figure 2.16 Light-activated ATP electrochemistry. (Top) Chemical structure of the DMPE-ATP used in all light-activated ATP studies. (Top right) Plot of current versus time for DMPE on a DNA-modified electrode. Note that as the DMPE-equilibrates on the electrode a small current is observed, followed by a large spike when the ATP is activated with 254 nm light (black curve). (Top Right) When protein is incubated on the surface with 10 mM DMPE, the signal is larger, and attributed to the [4Fe-4S] cluster, however upon photoactivation (orange), a large redox peak is activated due to the DMPE group. (Bottom Left) CVs for DNA-modified electrod when UV light is exposed to the surface. Note that no redox active peaks are present. (Bottom Right) CVs of DMPE on a DNA modified electrode. Note that, upon photorelease of the DMPE group, a large irreversible redox couple emerges. Decoupling this redox peak from the [4Fe-4S] cluster is a challenge and will not be pursued

Conclusions

XPD, a critical helicase for NER, contains a redox-active [4Fe-4S] cluster that is sensed electronically as a reporter of ATPase/helicase activity. The DNA-bound redox potential is similar to previously reported BER proteins. Here, DNA electrochemistry provides a sensitive means for detecting ATP-dependent signaling that may be generally useful in screening the activity of DNA-binding proteins containing redox centers. The activity can be distinguished between the WT protein and ATP-deficient activity of the G34R mutant, as well as between the native and non-native DNA substrates. Furthermore, attempts were made to coordinate ATP signaling using a light-activated ATP, which was redox active. Additionally, these results prompt the question as to how this electronic signaling of XPD activity might be utilized *in vivo*, and further, to which proteins XPD may be signaling inside the cell. Various repair and replication proteins, including FancJ and Dna2, which act in maintaining genomic stability, also have an associated [4Fe-4S] cluster.^{27,28} We suggest that it will be important to test other proteins acting at the interface of repair with major DNA processes of replication and transcription for their CT ability.

References

- (1) Eisen, J. A.; Hanawalt, P. C. *Mutat. Res.* **1999**, *435*, 171.
- (2) Fry, R. C.; Begley, T. J.; Samson, L. D. *Annu. Rev. Microbiol.* **2005**, *59*, 357.
- (3) David, S. S.; O'Shea, V. L.; Kundu, S. *Nature* **2007**, *447*, 941.
- (4) Sancar, A. *Annu. Rev. Biochem.* **1996**, *65*, 43.
- (5) Fuss, J. O.; Tainer, J. A. *DNA Repair (Amst)* **2011**, *10*, 697.
- (6) de Laat, W. L.; Jaspers, N. G.; Hoeijmakers, J. H. *Genes Dev.* **1999**, *13*, 768.
- (7) Lehmann, A. H. *Genes Dev* **2001**, *15*, 15.
- (8) Liu, H.; Rudolf, J.; Johnson, K. A.; McMahon, S.A.; Oke, M.; Carter, L.; McRobbie, A. M.; Brown, S. E.; Naismith, J. H.; White, M. F. *Cell* **2008**, *133*, 801.
- (9) Wolski, S. C.; Kuper, J.; Hanzelmann, P.; Truglio, J. J.; Croteau, D. L.; Van Houten, B.; Kisker, C. *PLoS Biol.* **2008**, *6*, e149.
- (10) Fan, L.; Fuss, J. O.; Cheng, Q. J.; Arvai, A. S.; Hammel, M.; Roberts, V. A.; Cooper, P. K.; Tainer, J. A. *Cell* **2008**, *133*, 789.
- (11) Rudolf, J.; Makrantoni, V.; Ingledew, W. J.; Stark, M. J.; White, M. F. *Mol Cell* **2006**, *23*, 801.
- (12) Pugh, R. A.; Honda, M.; Leesley, H.; Thomas, A.; Lin, Y.; Nilges, M. J.; Cann, I. K.; Spies, M. *J. Biol. Chem.* **2008**, *283*, 1732.
- (13) Genereux, J. C.; Boal, A. K.; Barton, J. K. *J. Am. Chem. Soc.* **2010**, *132*, 891.
- (14) Genereux, J. C.; Barton, J. K. *Chem. Rev.* **2010**, *110*, 1642.
- (15) Slinker, J. D.; Muren, N. B.; Renfrew, S. E.; Barton, J. K. *Nat. Chem.* **2011**, *3*, 230.

- (16) Boon, E. M.; Ceres, D. M.; Drummond, T. G.; Hill, M. G.; Barton, J. K. *Nat. Biotechnol.* **2000**, *18*, 1096.
- (17) Boal, A. K.; Barton, J. K. *Bioconjugate Chem.* **2005**, *16*, 312.
- (18) Boal, A. K.; Yavin, E.; Lukianova, O. A.; O'Shea, V. L.; David, S. S.; Barton, J. K. *Biochemistry* **2005**, *44*, 8397.
- (19) Gorodetsky, A. A.; Boal, A. K.; Barton, J. K. *J Am. Chem. Soc.* **2006**, *128*, 12082.
- (20) Boal, A. K.; Genereux, J. C.; Sontz, P. A.; Gralnick, J. A.; Newman, D. K.; Barton, J. K. *Proc. Natl. Acad. Sci. U.S.A.* **2009**, *106*, 15237.
- (21) Romano, C. A.; Sontz, P. A.; Barton, J. K. *Biochemistry*, **2011**, *50*, 6133.
- (22) Bard, A. J.; Faulkner, L. R. *Electrochemical Methods – Fundamental and Application*, 2nd ed.; John Wiley & Sons, New York, **2000**; pp 580-631.
- (23) Drummond, T. G.; Hill, M. G.; Barton, J. K. *J. Am. Chem. Soc.* **2004**, *126*, 15010.
- (24) Eckstein, F. *Angew. Chem., Int. Ed.* **1983**, *22*, 423.
- (25) Singleton, M. R.; Dillingham, M. S.; Wigley, D. B. *Annu. Rev. Biochem.* **2007**, *76*, 23.
- (26) Ha, T.; Rasnik, I.; Cheng, W.; Babcock, H. P.; Gauss, G. H.; Lohman, T. M.; Chu, S. *Nature* **2002**, *419*, 638.
- (27) Wu, Y.; Suhasini, A. N.; Brosh, R. M. Jr., *Cell Mol. Life Sci.* **2009**, *66*, 1209.
- (28) Vaithiyalingam, S.; Warren, E. M.; Eichman, B. F.; Chazin, W. J. *Proc. Natl. Acad. Sci. U.S.A.* **2010**, *107*, 13684.

Chapter 3

Charge transfer properties of mutants related to the human diseases xeroderma pigmentosum, cockayne syndrome, and trichothiodystrophy in the [4Fe-4S] cluster-containing helicase XPD from *Sulfolobus acidocaldarius*

T.P.M. and Winnie Wang performed electrochemistry. J.O.F. and J.P.I. purified protein and performed biochemical characterizations.

Introduction

DNA charge transfer (CT) is the phenomenon by which electrons are transferred through the π -stacked bases of DNA (1). This process is exquisitely sensitive, as perturbations to individual base pairs alter the geometry of the π -stack dramatically, thereby attenuating the conductivity of the DNA “wire.” However, nicks in the sugar phosphate backbone do not affect this process (2). Double-stranded DNA in a variety of conformations, including G-quadruplexes and Holliday junctions, has been shown to conduct charge (3-6). Recently, a model was proposed whereby redox-active proteins utilize DNA-mediated CT to localize near the site of DNA lesions because of the attenuation of CT at these sites. In the model system, MutY and EndoIII, two base excision repair (BER) proteins from *E. coli*, are activated towards oxidation upon DNA binding. Protein oxidation releases an electron to a distally bound protein, which, upon reduction, dissociates from the DNA. However, if an intervening lesion is present, this electron transport process can no longer occur, and the repair proteins remain bound to the DNA and eventually progress towards the lesion (7-10).

To observe this model in an *in vitro* system, mutants of endonuclease III (EndoIII) with varying CT proficiencies were identified (11). CT proficiency was measured on DNA-modified electrodes. An atomic force microscopy assay (AFM) that measures protein distribution onto DNA strands that are either completely well-matched or contain a single C:A mismatch showed that the mutants with enhanced CT proficiency increased the redistribution of these proteins towards sites of DNA damage, while mutations that were CT-deficient showed a reduced preference towards lesions (11). This assay

demonstrated the importance of protein signaling via DNA-mediated CT for redox-active proteins to localize at lesions.

Sulfolobus acidocaldarius (Sa)XPD has recently been identified as a [4Fe-4S] cluster-containing protein (12-14), which binds DNA and exhibits a DNA-bound redox potential of 80 mV versus NHE, similar to the BER proteins previously described (15). This protein was furthermore found to exhibit an ATP-dependent increase in electronic signaling. XPD is essential for nucleotide excision repair (NER) and XPD deletions are inviable in mice (16, 17). Mutations in XPD are linked to the diseases xeroderma pigmentosum, trichothiodystrophy, and cockayne syndrome. In patients, these mutations lead to progeria and often cancers (16, 18-22). Many of these mutant proteins have been studied in cellular extracts from patients, but, the activities of the individual protein mutants have yet to be assayed (18, 20). While it is a thermophile, SaXPD is a good model system, as many of the mutations found in the human XPD protein share homology with SaXPD (14, 22).

In this work, we describe both the biochemical and electrochemical characterization of single-point mutants of SaXPD that are disease related in humans. We further explore how electrochemical signaling in each of these mutants may contribute to the deficiencies that lead to human disease.

Materials and Methods

Chemicals were purchased from Sigma Aldrich. All reagents for DNA synthesis were purchased from Glen Research. Gold on mica was purchased from Agilent Technologies.

Protein purification

The *Sulfolobus acidocaldarius* XPD expression construct as described was modified to improve expression by removing a frame-shifting ATG start codon between the RBS and the correct start codon (14). Mutants were then generated using quikchange XL II kit (Stratagene) and verified by sequencing. All proteins were expressed in BL21 Rosetta2 *E. coli* cells (Invitrogen) grown in Terrific Broth at 37°C for 3 hours after induction with 0.2 mM IPTG. Cells were resuspended in 20 mM MES (pH 6.0), 100 mM NaCl, 1 mM DTT, 1 mM EDTA and lysed by sonication and constant cell disruptor (Constant Systems) at 20,000 psi. After centrifugation at 29,000 RCF for 30 min, the supernatant was heat treated (65°C, 20 min), centrifuged as before, and incubated with Capto DEAE (GE Healthcare) for 10-20 min at room temperature. The flow-through was collected by gravity and loaded onto a 5 mL HiTrap Heparin (GE Healthcare) column at 2 mL/min. Bound protein was washed (7 column volumes) with lysis buffer and eluted with a linear gradient (7 column volumes) to 45% high salt buffer (20 mM MES pH 6, 1 M NaCl, 1 mM DTT, 1 mM EDTA). SaXPD-containing fractions (~36% high salt buffer) were pooled, concentrated using Amicon Ultra Ultracel-10k regenerated cellulose spin filters, and fractionated on a HiLoad 16/60 Superdex200 (GE Healthcare) size exclusion column at 1 mL/min in 10.8% high salt buffer (200 mM NaCl final). SaXPD-containing fractions were pooled, concentrated as above to 2-12 mg/mL by OD₂₈₀, and

frozen. All cell and protein manipulations were carried out at 4°C unless otherwise noted, buffers were filtered and degassed, and purification was carried out in one day when possible to limit oxygen exposure.

Prior to electrochemical measurements, proteins were dialyzed against the protein buffer (20 mM Phosphate, 100 mM NaCl, 1 mM EDTA, 5% glycerol, pH 7.5) to remove residual DTT. The concentration of individual proteins was determined by UV-Vis using $\epsilon=17,000 \text{ M}^{-1}$ at 410 nM for the [4Fe-4S] cluster (Figure 3.1). The majority of the protein work was conducted in an oxygen-free environment to prevent degradation of the [4Fe-4S] cluster.

ATPase assay

ATPase activity was measured by monitoring production of free phosphate catalyzed by the hydrolysis of ATP using the Biomol Green Reagent (Enzo Life Sciences). In a 96-well plate, 50 μL of 20 nM ssDNA, 50 μM ATP, 25 nM Rad3 was incubated in assay buffer (50 mM Tris pH 8.0, 0.1 mg/mL BSA, 2 mM MgCl₂) for 60 minutes at 30°C. Reactions were quenched with 100 μL of Biomol Green Reagent, incubated at room temperature to allow the reagent to develop, and absorbances were measured using a plate reader with 630 nm filter cut-off. ATPase activity was determined by comparing absorbance values against a standard curve.

Helicase Assay

Cy5- and Iowa Black Dark-modified DNAs were ordered from IDT DNA (Coralville, IA). DNA was annealed in phosphate buffer (20 mM phosphate, 50 mM NaCl, pH 7.5). Duplexes were quantified by UV-visible spectroscopy and diluted to reach a final concentration of 1 μM . Using a Bio-Rad 96-well plate fluorescent

themocycler reader, 30 μ L reactions of 5 nM duplex, 500 μ M ATP, and 300 nM Rad3 were incubated in assay buffer and monitored over one hour with scans taken every 30 seconds. Reactions were initiated by addition of ATP. Helicase activity was measured and fit to first-order kinetics to determine rate constants.

DNA-binding experiments

Fluorescence anisotropy was measured using a Flexstation 3 instrument. Rad3-DNA interactions were proved in a reaction mixture of assay buffer with 10 nM fluorescein-labeled DNA (IDT DNA) in 20 μ L reactions using the substrate 5'(fam)CACGTTGACTACCGTC -3'. The protein-DNA mixture was incubated at 30°C for 20 minutes, and fluorescence was monitored at 520 nm for in 30-second intervals for 5 minutes. Polarization data was measured in triplicate and fit to a 4-parameter hill coefficient to determine ssDNA binding constants using kaleidagraph.

DNA synthesis

DNA was synthesized as previously described. Standard phosphoramidites were used on an ABI 3400 DNA synthesizer with modifications from Glen Research. DNA was purified by reverse-phase HPLC, and solvent removed through lyophilization. Disulfide-modified DNA was resuspended in 400 μ L reduction buffer (50 mM Tris, pH 8.0) and reduced with 10 mg of DTT. DNA quantification was based on UV-visible absorbances at 260 nm.

DNA-modified electrochemistry

Duplex DNA [50 μ M] with a 5' ssDNA overhang was annealed in degassed phosphate buffer (50 mM phosphate, 100 mM NaCl, 1 mM EDTA, pH 7.5) and allowed to self-assemble on a gold-on-mica surface overnight (Agilent technologies). Excess

DNA was washed a minimum of three times from the surface with phosphate buffer. The surface was then backfilled with a solution of 1 μ M mercaptohexanol in protein buffer (200 mM NaCl, 50 mM Tris, pH 8.0, 1 mM EDTA and 5% glycerol). Protein was added to the electrode housing, and electrochemistry was performed using a CH Instruments 600 potentiostat and a 3-electrode set-up with a Ag/AgCl reference electrode, platinum auxiliary, and DNA-modified electrode as the working surface. All measurements were performed in a glovebag with 2% hydrogen and 98% nitrogen to prevent degradation of the protein cluster and minimize the presence of oxygen.

For data analysis, current values were obtained by averaging the reductive sweep of a CV after linear base line corrections. After equilibration on the surface, a linear fit was used as the background current. The value of the current was then subtracted from the background current to obtain the difference in current. This value was then normalized to the surface by dividing by the background current to obtain the % difference in current. From the % difference in current data, 1st order kinetics were plotted to fit the parameters yield=1-e^{-kt}.

Results

SaXPD single point mutations: biochemical and electrochemical characterization

SaXPD protein mutants were overexpressed and purified. Individual mutations were made on a plasmid through site-directed mutagenesis. Proteins were dialyzed against protein buffer (200 mM NaCl, 1 mM EDTA, 20 mM Triza-HCl pH 8.0) to remove residual DTT. Helicase, ATPase, and DNA-binding activities were assayed to determine the activities of each protein mutant (Table 3.1). All mutants show ssDNA binding constants between 60 – 80 nM. ATPase activity was observed in the WT and Y104A mutants, while no activity was observed for the R460P and G34R mutants. The L325V, R460W, and K84C mutants retained 43%, 11%, and 49% of WT ATPase activity, respectively. None of the mutants exhibited helicase activity comparable to the WT protein. However, the L325V, R460W, and Y104A mutants retained 66%, 64%, and 49% of WT helicase activity, respectively, while the R460P, G34R, and K84C mutants showed less than 10% of WT activity (Table 3.1).

Prior to electrochemical experiments, the protein was quantified by UV-Vis using the absorbance at 410 nm, indicative of the [4Fe-4S] cluster (Figure 3.1). A structure of the SaXPD protein with the relevant single point mutations is shown in Figure 3.3B. We have developed an electrochemical assay for ATPase activity using DNA-modified electrodes. To verify the ATPase activity of these newly-generated disease-related mutants, proteins were incubated on a DNA-modified electrode, and various concentrations of ATP or ATP- γ -S were added. When ATP- γ -S was added, no increase in current was observed, as ATP- γ -S is a more slowly hydrolysable ATP analogue. However, upon 5 mM ATP addition, an increase in the electrochemical signal intensity

was observed (Figure 3.2A). The ATPase and helicase deficient G34R mutant shows no noticeable increase, while the Y104A mutant (which is not a disease-related mutant) exhibits kinetics similar to the WT protein. The K84C mutant, which is helicase proficient but ATPase deficient, shows an electronic signal increase between the WT and G34R mutant upon addition of 5 mM ATP (Table 3.1, Figure 3.2A).

To determine the efficiency of DNA-mediated charge transfer for each of these individual mutants, each protein (~10 μ M) was incubated on a DNA-modified electrode, and cyclic voltammograms (CVs) were taken every 3 minutes. The surface was rinsed, and subsequently scanned to verify that any residual protein was removed. This process was repeated for each of the protein mutants. While the magnitudes of the currents varied, each protein retained the same mid-point redox potential of ~80 mV versus NHE. Current intensities were determined for each of the protein mutants and normalized to [4Fe-4S] cluster content (Figure 3.2D). All mutants made have been implicated in human disease, with the exception of the Y104A mutant, which was generated to explore the CT pathway in the protein. This mutant exhibited an electrochemical signal much larger than that of the WT protein (approximately 2-5 times larger). Similarly, the K84H mutant, a mutant implicated in disease, exhibits a signal larger than WT (Figure 3.2D). The G34R mutant, which is ATPase and helicase deficient, exhibits a signal comparable to the WT protein (Figure 3.2D). As predicted in our model for communication between proteins, a larger redox signal would translate into more efficient CT between proteins.

We have identified a variety of protein mutants implicated in either TTD, XP, or XP and CS with ATPase and helicase activities, DNA binding affinities, and TFIIH complex forming abilities comparable to WT. However, when placed on our DNA-

modified electrodes, the R460P, R460W, L325V, and A511R mutants exhibit protein signals two to three times lower than that of the WT protein. While these proteins have some variation in ATPase and helicase activity (Table 3.1), their activities are within that of the WT protein. The only difference appears to be the protein mutants' ability to signal one another by DNA-mediated CT. This electrochemical defect represents the intriguing possibility that could explain why these mutants lead to human disease.

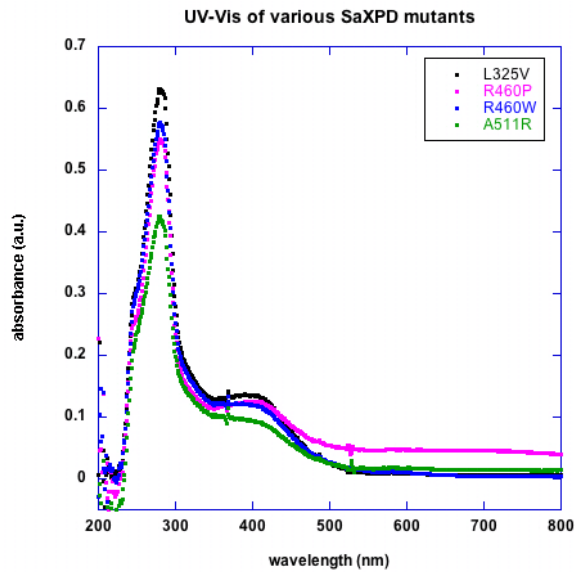


Figure 3.1. UV-Vis of various SaXPD mutants. L325V (black), R460P (purple), R460W (blue), and A511R (green) all show a characteristic absorbance at 410 nm, indicative of a [4Fe-4S] cluster. Based on this absorbance, a concentration can be determined using $\epsilon = 17,000 \text{ M}^{-1}$

Mutant	Human	Electrochemical signal intensity (relative to wt)	Helicase bp/min (%wt)	ATPase mol/sec (%wt)	ssDNA Kd (nM) (%wt)
WT	--	--	10.7 ± 0.95 (100%)	0.81 ± 0.03 (100%)	66.0 ± 5.4 (100%)
L325V	L461V	0.31 ± 0.07	7.13 ± 0.32 (66%)	0.35 ± 0.02 (43%)	69.3 ± 7.8 (95%)
R460W	R616W	0.26 ± 0.06	6.83 ± 0.10 (64%)	0.092 ± 0.005 (11%)	66.7 ± 10 (99%)
R460P	R616P	0.39 ± 0.07	0.75 ± 0.42 (7%)	0.012 ± 0.003 (1.4%)	79.3 ± 2.7 (80%)
G34R	G47R	1.19 ± 0.13	0.98 ± 0.53 (9%)	0.002 ± 0.001 (0%)	66.8 ± 2.7 (99%)
K84C	R112C	3.87 ± 0.81	0.90 ± 0.42 (8%)	0.39 ± 0.05 (49%)	79.8 ± 0.35 (79%)
Y104A	H155	5.94 ± 1.42	5.3 ± 0.42 (49%)	0.89 ± 0.12 (110%)	60.7 ± 6.4 (108%)

Table 3.1. Biochemical activity of single SaXPD mutants. CT signal proficiency, helicase, ATPase, and ssDNA binding for the various SaXPD mutants and their corresponding human mutations shown. Data from (23) or obtained from the Tainer lab.

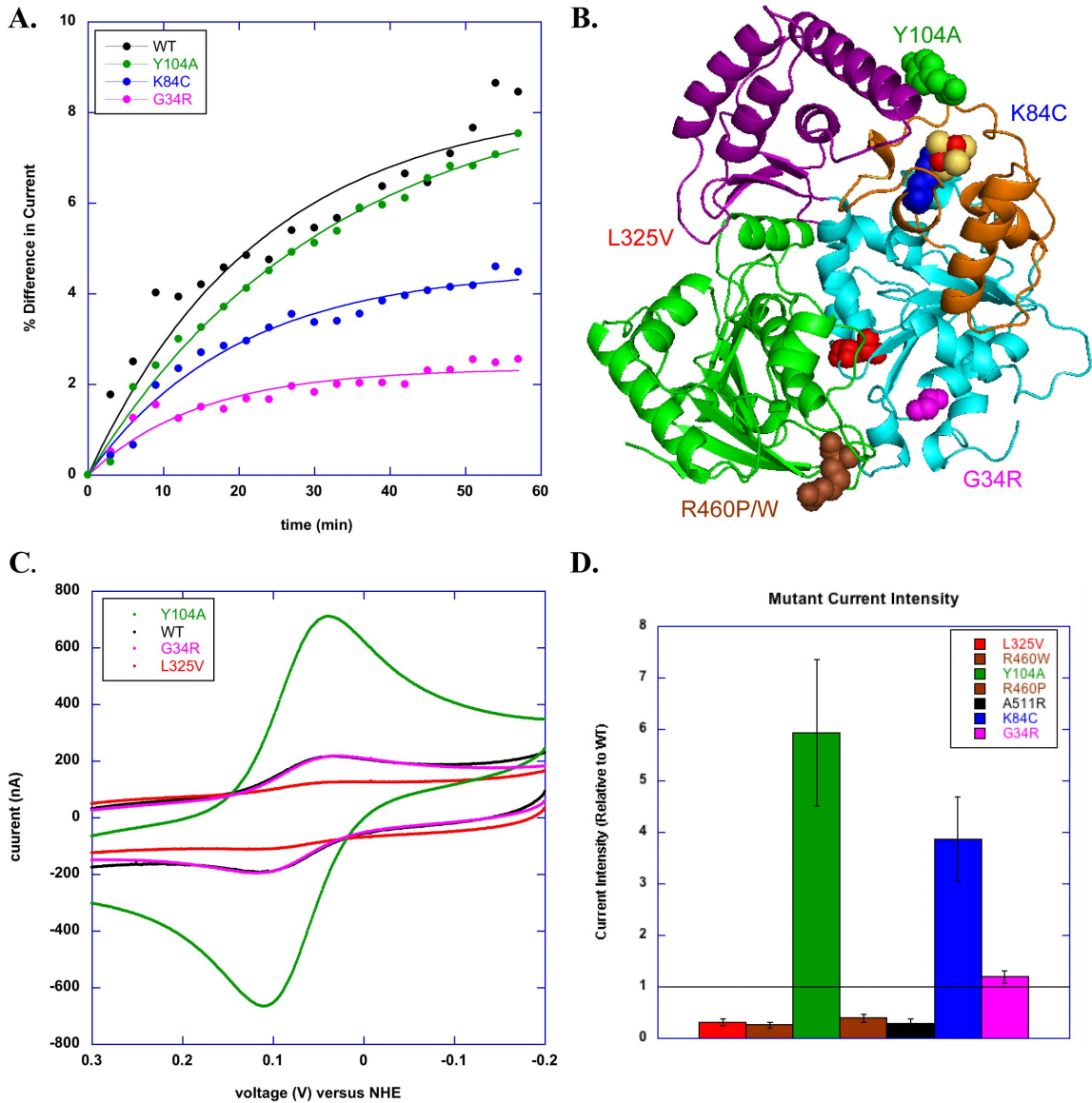


Figure 3.2. Electrochemical signal for various SaXPD single mutants. A. ATPase activity of WT, Y104A, K84C, and G34R SaXPD on a DNA modified electrode after 5 mM ATP addition. B. Crystal structure of SaXPD with mutations highlighted as colored spheres. C. CV of various SaXPD mutants Y104A (green), WT (black), G34R (pink), and L325V (red) after 90 minutes on the DNA-modified electrodes. D. Quantification of the various SaXPD electrochemical signals on the same DNA modified electrode compared to WT SaXPD signal.

Double mutant electrochemistry to restore CT to single point mutants

Mutations in SaXPD are thought to be conserved between archaea, yeast, and humans, and our electrochemical data suggested that CT-deficiency may be related to disease. With the intent to restore CT to the CT-deficient disease-related mutants, L325V, R460P, R460W, we combined the enhanced CT-proficient Y104A mutation with each of these single point mutants. The newly generated Y104A/L325V, Y104A/R460P, and Y104A/R460W double mutants were then quantified by UV-Vis, and their electrochemical signals were normalized to [4Fe-4S] cluster content. The protein mutants were incubated on a DNA-modified electrode for 90 minutes, with CV scans taken every 3 minutes. The CV was then background corrected and quantified to obtain a value for the current. These signals were then averaged and compared to the WT signal, and error was determined from the deviation at each timepoint. Relative current intensity is shown in Figure 3.3 and is normalized to the WT signal. Each of the double mutants exhibited a redox signal lower than not only the WT protein, but also the single CT-deficient L325V mutant. As a control the Y104A and L325V single point mutations were also assayed and displayed an enhanced and reduced signal, respectively. These results suggest that, while each single mutant has a particular property of interest, the combination of two mutations does not lead to a combined restorative effect.

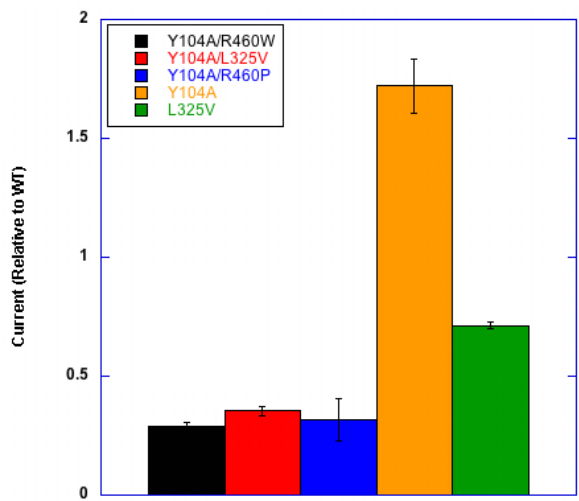


Figure 3.3. Double mutant SaXPD electrochemistry. Relative current intensity for the SaXPD double mutants, Y104A (yellow), L325V (green), Y104A/R460W (black), Y104A/L325V (red), and Y104A/R460P (blue) SaXPD protein mutants on a DNA-modified electrode.

Modeling a double mutant to restore CT to the deficient L325V mutant in SaXPD

The SaXPD crystal structure provides a wealth of information about protein tertiary structure, as well as potential interactions between neighboring amino acid residues. From models based on the crystal structure, it appears that a leucine (Figure 3.4 A, orange spheres) to valine (Figure 3.4 B, green spheres) mutation at position 325 creates a steric clash with methionine 331 (Figure 3.4, red spheres). This interaction could explain the CT-deficiency of the L325V mutant, as the residues surrounding the mutation may have altered positions in order to accommodate the steric clash. Based on this interaction, the methionine was reduced to an alanine to generate the combined L325V/M331A double mutant (Figure 3.5A).

Prior to all electrochemistry experiments, protein mutant concentrations were quantified based on their absorbance at 410 nm. These mutants were incubated on a DNA-modified electrode for 90 minutes, with CV scans taken every 3 minutes. On the electrode, these mutants all exhibited a DNA-bound redox potential of 80 mV versus NHE. The WT protein exhibited an average current intensity of 67.6 ± 6.4 nA. The L325V mutant showed a current intensity of 69.7 ± 3.8 nA compared to 49.6 ± 3.4 nA for the M331A mutant. The L325V/M331A double mutant exhibited an intensity of 85 ± 6.1 nA on the same surface (Figure 3.5c). The L325V and L325V/M331A were purified using a new purification protocol independent of the WT SaXPD and, as a result, may lead to different CT proficiencies because of impurities associated with the newer purification or decreased binding in the WT protein over time.

Finally, these mutants were electronically assayed for their ATPase activity as previously reported. Briefly, the protein was allowed to incubate for 90 minutes on the

electrode. ATP- γ -S, a slowly hydrolysable ATP analogue, was added to the electrode first to verify that the signal does not increase with the addition of the ATP-mimic. Increasing amounts of ATP were then added during 60-minute intervals, with CVs taken every 3 minutes. Finally, a large amount of ATP- γ -S was added to verify that any signal increases were due to ATP hydrolysis. Figure 3.5D shows the effect of 5 mM ATP addition on the electrochemical signal for each of these mutants. Both the WT and L325V mutant have electronic ATPase activity consistent with *in vitro* assays (Table 3.1). However, the L325V/M331A mutant shows a diminished ATPase activity comparable to the G34R mutant (Figure 3.2A). The M331A mutant lacks both ATPase and helicase activity *in vitro* (data not shown), which potentially explains why the L325V/M331A mutation shows minimal electronic ATPase activity.

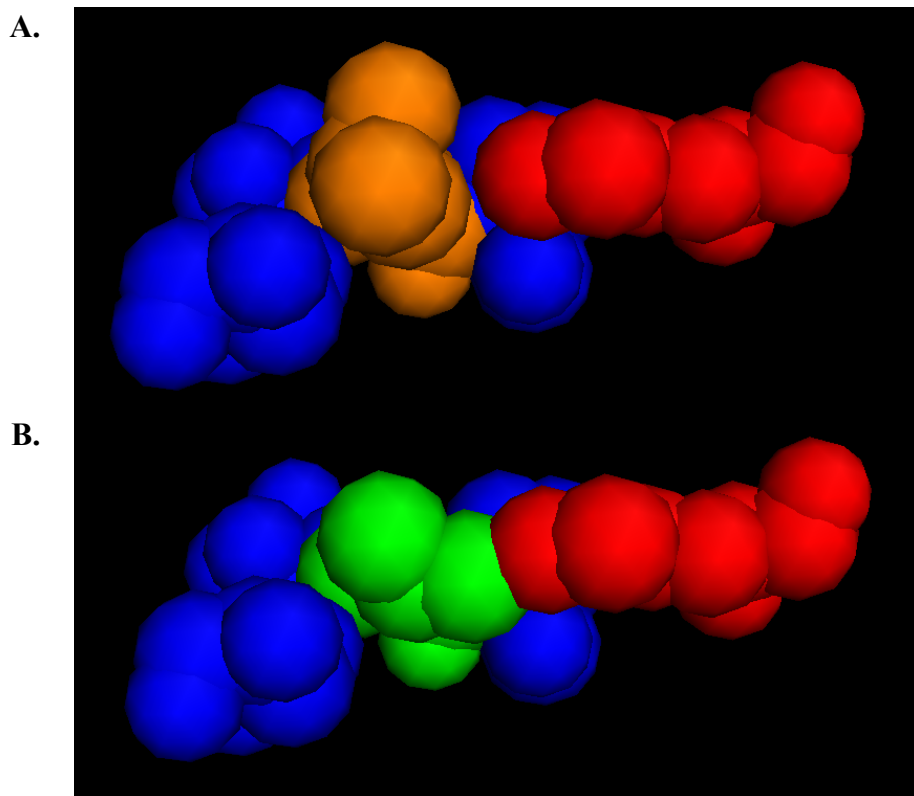


Figure 3.4 Pymol model of SaXPD for L325V mutation. A. WT SaXPD crystal structure with L325 (orange) and M331 (red) residues highlighted. B. SaXPD crystal structure with L325V (green) and M331 (red) residues highlighted. Both structures are from PDB ID 3CRV.

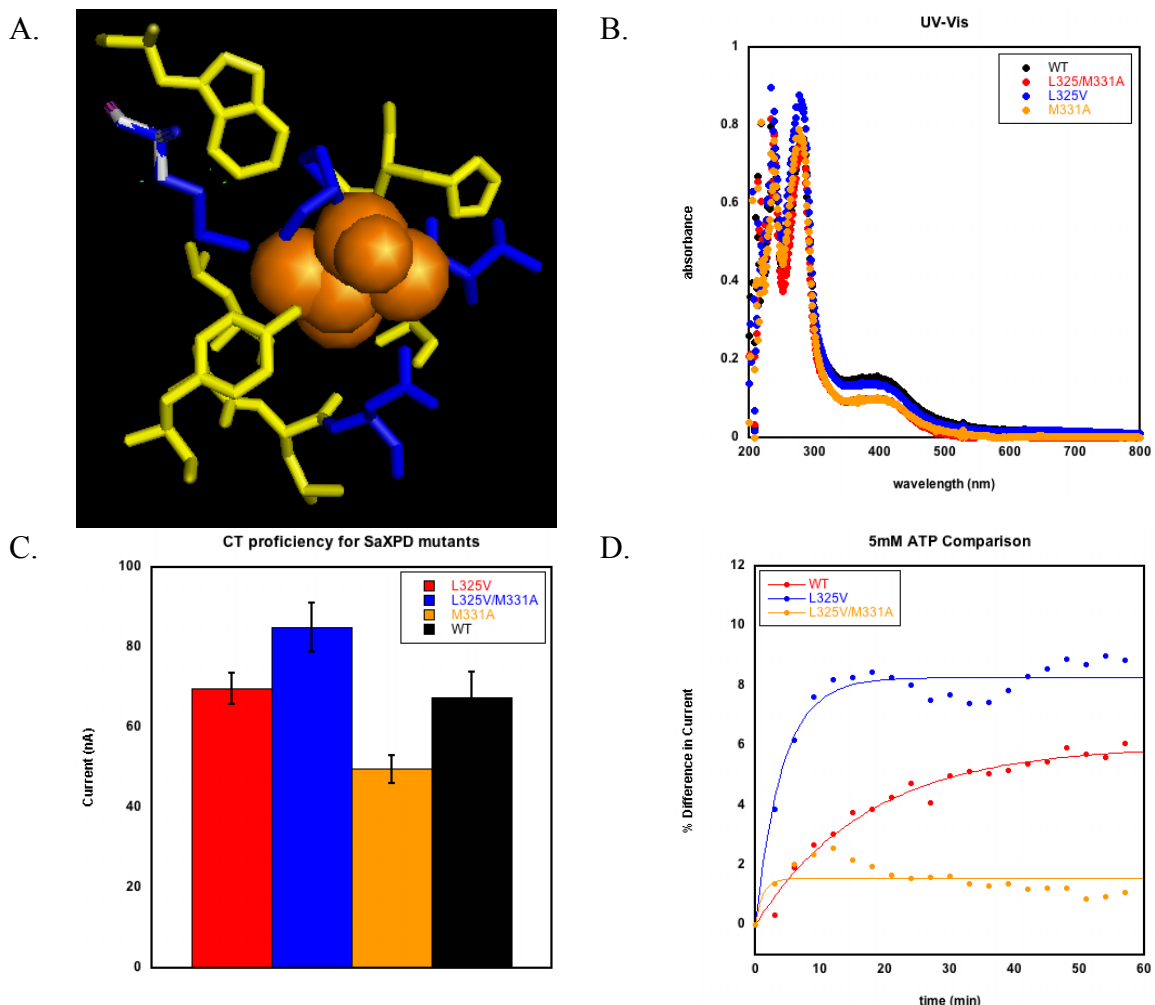


Figure 3.5 Modeled repair of L325V SaXPD mutation. A. Crystal structure of SaXPD (PDB ID 3CRV) with L325V (orange) mutations. Interactive residues are shown in yellow and blue. An M331A mutation (blue and gray) is shown where the methionine is reduced to an alanine to prevent steric interactions with L325V. B. UV-Vis of the WT (black), L325V/M331A (red), L325V (blue), and M331A (yellow) SaXPD mutants using the 410 nm absorbance for quantification. C. Average current signal for the SaXPD L325V (red), L325V/M331A (blue), M331A (yellow), and WT (black) mutants after 90 minute incubation on a DNA-modified electrode. The signal for the double mutants is approximately 10% larger than the single L325V mutant. D. Percent difference in current over time for the various SaXPD mutants upon 5 mM ATP addition.

Discussion

The XPD family of helicases is essential for nucleotide excision repair (NER). These proteins are well conserved between species, and mutations from human XPD that lead to disease are found in *S. acidocaldarius* XPD. Using DNA-modified electrodes, we assayed the single point disease-relevant G34R, K84C, L325V, R460P, R460W, and A511R mutants as well as the artificially designed Y104A mutant. These mutants all contain a [4Fe-4S] cluster similar to the WT protein, as evidenced by UV-Visible spectroscopy. When characterized biochemically, the G34R, R460P, and A511R mutants lack both ATPase and helicase activity, which are required for NER. However, the K84C, L325V, R460W, and Y104A mutants exhibit activities significantly closer to the WT protein. Mutations affecting the biochemical activity of XPD explain how these mutants lead to the human diseases associated with XP proteins. However, the reason why K84C, L325V, and R460W all lead to disease are as yet unknown.

On a DNA-modified electrode all protein mutants exhibited a DNA-bound redox potential of 80 mV versus NHE. When assayed electronically for ATPase activity, the WT, Y104A, and L325V showed similar activity, while the ATPase deficient G34R, R460P, and A511R mutants showed minimal ATPase activity. The K84C mutation, which is helicase deficient but ATPase proficient, showed mediocre activity. Therefore, our electronic DNA-mediated ATPase assay agrees with other *in vitro* ATPase assays. This assay does not require labeling of DNA or the protein and simply monitors increases in electronic signaling.

Protein coupling into the DNA π-stack is another mechanism by which proteins can utilize these redox-active [4Fe-4S] clusters to communicate with one another. For each of these mutants, we additionally compared the signals from each of the individual

protein mutants. Both the WT and G34R mutant showed similar signals, but the disease-relevant L325V, R460P, R460W, and A511R mutants exhibited attenuated redox signals compared to the WT protein. Poor coupling into the DNA π -stack potentially explains how mutants such as L325V and R460W, which both have ATPase and helicase activity, lead to disease.

To determine if multiple mutations lead to additive effects on DNA CT, double mutants of a CT-enhanced Y104A mutant with each of the CT-deficient L325V, R460W, and R460P mutations were made. When assayed electrochemically, these mutations exhibited signals lower than any of the single point mutations. Therefore, in this system, additive effects were not observed when combining CT-enhanced mutations with those that are CT-deficient.

Based on the SaXPD crystal structure, a steric interaction was identified in the L325V mutant with M331. Steric interactions can cause local structure disruption, which can orient the cluster further from the DNA, thus attenuating coupling between the [4Fe-4S] cluster and the π -stack. To reduce this interaction, an L325V/M331A double mutant was generated. When assayed for electronic ATPase activity, this mutant exhibited negligible activity. The M331A mutation lacks both ATPase and helicase activity, which explains why when combined with L325V, this double mutant lacks activity. However, when assayed for electronic signaling, this mutant exhibits a 10% higher electronic signal compared to the single L325V mutation. These results are inconclusive, because the L325V mutation no longer appears to be CT-deficient compared to the WT protein, possibly due to a new purification scheme or diminished DNA binding of the WT protein

over time. However, the L325V/M331A mutant exhibits a larger redox signal compared to the single L325V mutant, so the *in vivo* effects of this double mutant are unknown.

Biochemically, double mutants appear to have non-additive effects. In fact, the Y104A/L325V, Y104A/R460P, and Y104A/R460W double mutants exhibited a destabilization. However, mutations in SaXPD appear to have a large effect on CT proficiency for the disease-related mutations. For each of these mutants, we were able to observe both electronic signals and electronic ATPase activity that correlated well with solution-based ATPase assays. Our electrochemical results provide an explanation for how mutations proficient in both ATPase and helicase activity can lead to disease. The L325V and R460W mutants, which are both biochemically active, show reduced electronic signaling. These mutations would therefore be interesting to study *in vivo* using a system more closely related to humans, such as the yeast *Saccharomyces cerevisiae* with the XPD homologue Rad3.

References

1. Kelley, S. O., and Barton, J. K. (1999) Electron transfer between bases in double helical DNA, *Science* 283, 375-381.
2. Liu, T., and Barton, J. K. (2005) DNA electrochemistry through the base pairs not the sugar-phosphate backbone, *J Am Chem Soc* 127, 10160-10161.
3. Nunez, M. E., Holmquist, G. P., and Barton, J. K. (2001) Evidence for DNA charge transport in the nucleus, *Biochemistry* 40, 12465-12471.
4. Nunez, M. E., Noyes, K. T., and Barton, J. K. (2002) Oxidative charge transport through DNA in nucleosome core particles, *Chem Biol* 9, 403-415.
5. Delaney, S., and Barton, J. K. (2003) Charge transport in DNA duplex/quadruplex conjugates, *Biochemistry* 42, 14159-14165.
6. Odom, D. T., Dill, E. A., and Barton, J. K. (2001) Charge transport through DNA four-way junctions, *Nucleic Acids Res* 29, 2026-2033.
7. Boal, A. K., Yavin, E., Lukianova, O. A., O'Shea, V. L., David, S. S., and Barton, J. K. (2005) DNA-bound redox activity of DNA repair glycosylases containing [4Fe-4S] clusters, *Biochemistry* 44, 8397-8407.
8. Yavin, E., Boal, A. K., Stemp, E. D., Boon, E. M., Livingston, A. L., O'Shea, V. L., David, S. S., and Barton, J. K. (2005) Protein-DNA charge transport: redox activation of a DNA repair protein by guanine radical, *Proc Natl Acad Sci U S A* 102, 3546-3551.
9. Boal, A. K., Genereux, J. C., Sontz, P. A., Gralnick, J. A., Newman, D. K., and Barton, J. K. (2009) Redox signaling between DNA repair proteins for efficient lesion detection, *Proc Natl Acad Sci U S A* 106, 15237-15242.

10. Genereux, J. C., Boal, A. K., and Barton, J. K. (2010) DNA-mediated charge transport in redox sensing and signaling, *J Am Chem Soc* 132, 891-905.
11. Romano, C. A., Sontz, P. A., and Barton, J. K. (2011) Mutants of the base excision repair glycosylase, endonuclease III: DNA charge transport as a first step in lesion detection, *Biochemistry* 50, 6133-6145.
12. Wolski, S. C., Kuper, J., Hanzelmann, P., Truglio, J. J., Croteau, D. L., Van Houten, B., and Kisker, C. (2008) Crystal structure of the FeS cluster-containing nucleotide excision repair helicase XPD, *PLoS Biol* 6, e149.
13. Pugh, R. A., Honda, M., Leesley, H., Thomas, A., Lin, Y., Nilges, M. J., Cann, I. K., and Spies, M. (2008) The iron-containing domain is essential in Rad3 helicases for coupling of ATP hydrolysis to DNA translocation and for targeting the helicase to the single-stranded DNA-double-stranded DNA junction, *J Biol Chem* 283, 1732-1743.
14. Liu, H., Rudolf, J., Johnson, K. A., McMahon, S. A., Oke, M., Carter, L., McRobbie, A. M., Brown, S. E., Naismith, J. H., and White, M. F. (2008) Structure of the DNA repair helicase XPD, *Cell* 133, 801-812.
15. Mui, T. P., Fuss, J. O., Ishida, J. P., Tainer, J. A., and Barton, J. K. (2011) ATP-stimulated, DNA-mediated redox signaling by XPD, a DNA repair and transcription helicase, *J Am Chem Soc* 133, 16378-16381.
16. Lehmann, A. R. (2001) The xeroderma pigmentosum group D (XPD) gene: one gene, two functions, three diseases, *Genes Dev* 15, 15-23.

17. Rudolf, J., Makrantoni, V., Ingledew, W. J., Stark, M. J., and White, M. F. (2006) The DNA repair helicases XPD and FancJ have essential iron-sulfur domains, *Mol Cell* 23, 801-808.
18. Dubaele, S., Proietti De Santis, L., Bienstock, R. J., Keriel, A., Stefanini, M., Van Houten, B., and Egly, J. M. (2003) Basal transcription defect discriminates between xeroderma pigmentosum and trichothiodystrophy in XPD patients, *Mol Cell* 11, 1635-1646.
19. de Boer, J., Andressoo, J. O., de Wit, J., Huijmans, J., Beems, R. B., van Steeg, H., Weeda, G., van der Horst, G. T., van Leeuwen, W., Themmen, A. P., Meradji, M., and Hoeijmakers, J. H. (2002) Premature aging in mice deficient in DNA repair and transcription, *Science* 296, 1276-1279.
20. Taylor, E. M., Broughton, B. C., Botta, E., Stefanini, M., Sarasin, A., Jaspers, N. G., Fawcett, H., Harcourt, S. A., Arlett, C. F., and Lehmann, A. R. (1997) Xeroderma pigmentosum and trichothiodystrophy are associated with different mutations in the XPD (ERCC2) repair/transcription gene, *Proc Natl Acad Sci U S A* 94, 8658-8663.
21. Suhasini, A. N., and Brosh, R. M., Jr. (2013) DNA helicases associated with genetic instability, cancer, and aging, *Adv Exp Med Biol* 767, 123-144.
22. Brosh, R. M., Jr. (2013) DNA helicases involved in DNA repair and their roles in cancer, *Nat Rev Cancer* 13, 542-558.
23. Fan, L., Fuss, J. O., Cheng, Q. J., Arvai, A. S., Hammel, M., Roberts, V. A., Cooper, P. K., and Tainer, J. A. (2008) XPD helicase structures and activities:

insights into the cancer and aging phenotypes from XPD mutations, *Cell* 133,
789-800.

Chapter 4

*In vivo and in vitro consequences of disease-related mutants in the [4Fe-4S] cluster-containing Rad3 helicase from *Saccharomyces cerevisiae**

T.P.M. and Andy Zhou purified proteins, performed yeast experiments, and protein electrochemistry.

Introduction

DNA is constantly being damaged by exogenous sources, and a complete understanding of the proteins involved in DNA repair is essential. Damage leading to mutations, premature aging, or even cancer is repaired by a variety of pathways, including base excision repair (BER), mismatch Repair (MMR), double strand break repair (DSBR), and nucleotide excision repair (NER). Proteins must quickly and efficiently localize to the site of damage and coordinate repair (1, 2). Each of these individual repair processes is well characterized, with models to describe the repair events (3-7).

The XPD family of proteins is well conserved, with homologues found throughout the eukaryotes. XPD is a SF2b 5'-3' helicase that is part of TFIIH required for NER (8-13). Mutations in human XPD result in the fatal diseases xeroderma pigmentosum, cockayne syndrome, and/or trichothiodystrophy (5, 14). It is somewhat surprising that one gene can lead to so many different disease states, but not that helicases play such a large role in DNA repair (14-16). Recently, XPD from three different thermophiles was crystallized and shown to contain a redox-active [4Fe-4S] cluster (17-19). The XPD protein from *Sulfolobus acidocaldarius* exhibits ATP-dependent DNA-mediated signaling via the cluster, which may also be involved in signaling to other proteins for DNA repair (20). Researchers further characterized the activity of the human disease-related mutants. Unsurprisingly, most disease-related mutants exhibited either ATPase or helicase deficiencies. A majority of the knowledge of the XPD protein function is based on either purified homologous thermophilic proteins, cellular extracts from human cell lines, or other eukaryotes (8-12, 21, 22).

Redox-active metalloproteins have recently been implicated in DNA repair, as the BER glycosylases, Endonuclease III and MutY, as well as the NER helicase XPD have been shown to contain a redox-active [4Fe-4S] cluster with a reversible DNA-bound potential of ~80 mV versus NHE (20, 23, 24). A model was proposed whereby these proteins can communicate with one another through DNA-mediated charge transport (CT), where electron transfer can occur through the π -stacked bases of undamaged DNA. In the case of a lesion, DNA CT does not occur, thus facilitating the localization of proteins near the site of DNA damage (23, 25, 26). In an AFM assay measuring the redistribution of these [4Fe-4S] cluster-containing proteins, it was observed that these proteins redistribute towards mismatched sites, a type of lesion that attenuates CT. However, with CT-deficient mutants, no such redistribution occurs (25-28). Furthermore, DNA-mediated CT has been shown in mitochondria and nucleosomes, and is involved with the transcription factor SoxR(24, 29).

The thermophilic protein system is useful for determining the individual effects of mutations in SaXPD; however, the SaXPD protein is less similar to human XPD than the *S. cerevisiae* homolog Rad3 (19). The crystal structures of SaXPD have provided a wealth of information, but Rad3 at 90 kDa is much more similar in size to human XPD (89 kDa) than SaXPD (68 kDa). SaXPD lacks about 200 amino acids that are found in ScRad3. Additionally, yeast more closely resemble human cells and would provide greater insight into the biochemical activities and fundamental basis for human diseases caused by the XPD protein compared to the thermophilic bacteria. Fewer techniques exist for genetic manipulations in *S. acidocaldarius* compared to the well-studied yeast *S. cerevisiae*. Many disease-relevant mutants have been explored in cellular extracts, with

XPD in complex with TFIIH, but few studies have explored the purified protein to verify its activity as native to Rad3 (9, 11, 30, 31). Here we report a new purification from *E. coli*, as well as some characterization of the G47R, I463V/del716-730 (I463V/Δ), R618P, R618W, and C665R mutations, which have been identified in XP-patients (7, 21, 22). Furthermore, we developed a haploid yeast *S. cerevisiae* strain to determine the *in vivo* effects associated with Rad3 mutations. To further understand their role in this disease, we quantitatively analyze the ATPase activity, helicase activity, DNA binding, NQO survival, and DNA-bound electrochemistry of these mutants.

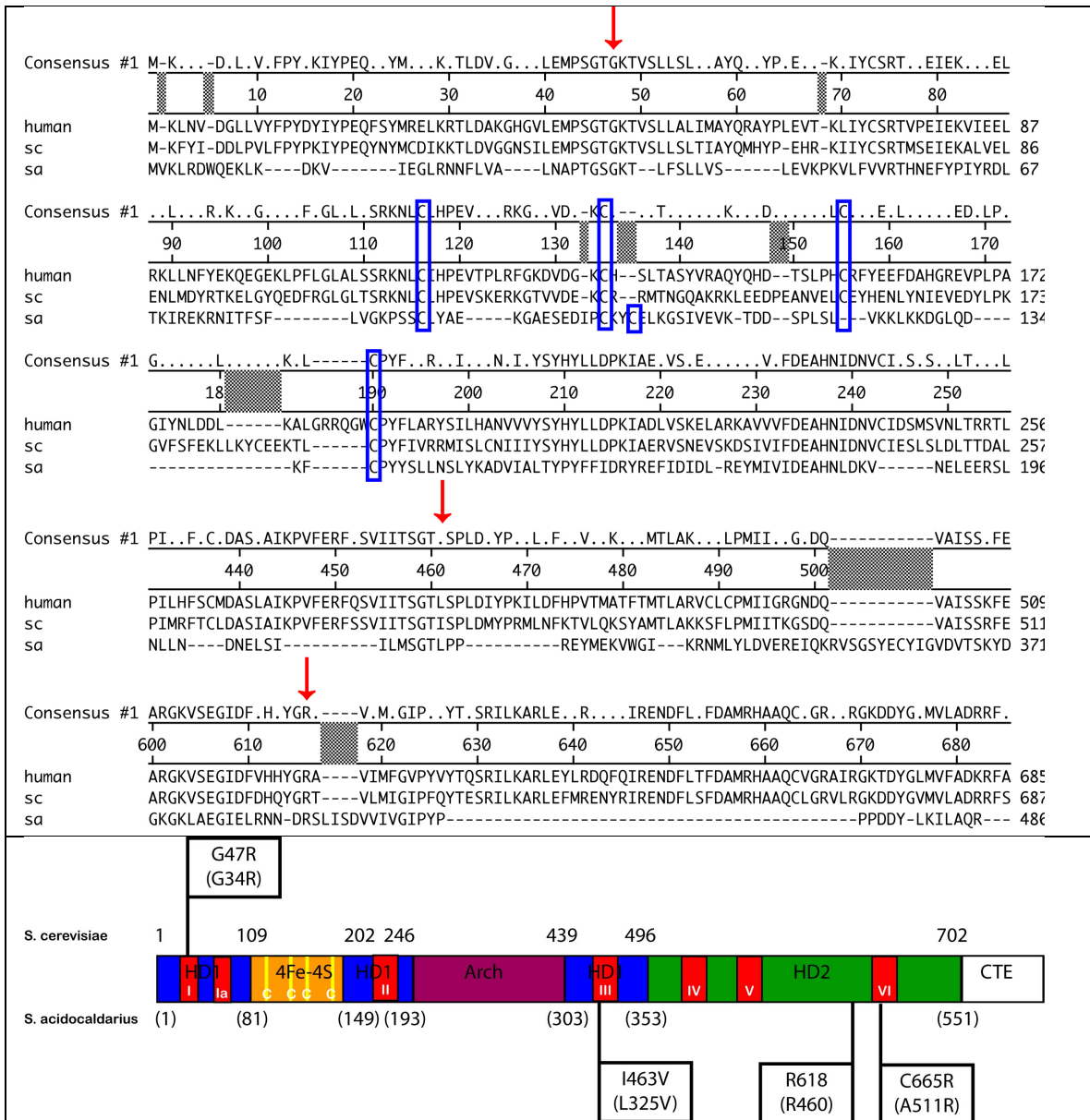


Figure 4.1. Alignment of XPD-family of helicases. (Top) Sequence alignment of *Homo sapien* (human) XPD, *Saccharomyces cerevisiae* (sc) Rad3, and *Sulfolobus acidocaldarius* (sa) XPD. Shown in blue boxes are the conserved cysteines that bind the 4Fe-4S cluster, while the red arrows show mutations associated with human disease. (Bottom) Cartoon schematic of the Rad3 protein based on sequence alignment from SaXPD. Mutations known either lead to XP, CS, TTD are shown in the boxes. Figure adapted from (19).

Materials and Methods

Chemicals were purchased from Sigma Aldrich. All reagents for DNA synthesis were purchased from Glen Research. Gold-on-mica was purchased from Agilent Technologies. All yeast media was purchased from Clontech.

Protein purification

Plasmids harboring the appropriate copy of the Rad3 gene were transformed into *E. coli* BL21(DE3)pLysS cells (Agilent) and plated onto LB+Chlr+Amp plates. Bacteria were grown in 2L batches of TB + chloramphenical (25 mg/mL) + ampicillin (100 mg/mL) at 37°C for 5-6 hours until they reached OD₆₀₀ ~ 0.6. The temperature was immediately dropped to 16°C, and cells were induced with 200 μM IPTG for 20-22 hours. Cells were pelleted and rinsed with 1X cold PBS and stored at -80°C until used.

Cells were resuspended in 1% HisTrap Buffer (20 mM Tris pH 8.0, 500 mM NaCl, 0.5 mM immidazole) with Protease Complete tablets (1 per 50 mL buffer) (Roche) using a homogenizer, and cells were lysed by microfluidization. Cleared cell lysates were loaded onto a pre-equilibrated HisTrap column (GE Life Sciences) and eluted by a linear elution gradient of 1-100% HisTrap Buffer B (20 mM Tris pH 8.0, 500 mM NaCl, 500 mM immidazole, 0.5 mM DTT) over 6 column volumes. Fractions were pooled and loaded onto a pre-equilibrated HiPrep 26/10 desalting column with 20% Anion Exchange Buffer (20 mM Tris pH 8.0, 200 mM NaCl, 1 mM EDTA, 2 mM DTT). The buffer exchanged protein was then loaded onto a pre-equilibrated Heparin column (GE life sciences) and eluted by linear gradient of 20-100% Anion Exchange Buffer B (20 mM Tris pH 8.0 1 M NaCl, 1 mM EDTA, 2 mM DTT). Fractions were pooled and concentrated using Amicon 100K MWCO filter units at 4,000 x g. The concentrated

product was loaded onto a Superdex200 gel filtration column with gel filtration buffer (20 mM Tris pH 8.0, 500 mM NaCl, 1 mM EDTA, 2 mM DTT) and eluted. Rad3-containing fractions were pooled and concentrated by Amicon 100K MWCO filter units and buffer exchanged into protein storage buffer (20 mM Tris pH 8.0, 200 mM NaCl, 1 mM EDTA, 5% glycerol). Final fractions were quantified by UV-visible spectroscopy and stored at -80°C until needed. The identity of the protein was confirmed by running a 7.5% SDS-PAGE gel, Trypsin digest MS/MS (Caltech, PPMAL), and activity assays.

Site-directed mutagenesis

Site-directed mutagenesis (SDM) was performed per the manufacturers instructions (Agilent Technologies). The following primers were used to generate the appropriate mutations in both the 7AC plasmid for protein purifications and the PRS313 plasmids for *in vivo* assays (Table 3.1). Plasmids were transformed into *E. coli* and plated onto selective media. Individual colonies were grown and mini-prepped. Mutations were verified by sequencing (Laragen Inc.).

ATPase assay

ATPase activity was measured by monitoring production of free phosphate catalyzed by the hydrolysis of ATP using the Biomol Green Reagent (Enzo Life Sciences). In a 96-well plate, 50 µL of 20 nM ssDNA, 50 µM ATP, 25 nM Rad3 was incubated in assay buffer (50 mM Tris pH 8.0, 0.1 mg/mL BSA, 2 mM MgCl₂) for 60 minutes at 30°C. Reactions were quenched with 100 µL of Biomol Green Reagent, incubated at room temperature to allow the reagent to develop, and absorbances were measured using a plate reader with 630 nm filter cut-off. ATPase activity was determined by comparing absorbance values against a standard curve.

Helicase Assay

Cy5-and Iowa Black Dark (IBRQ)-modified DNAs were ordered from IDT DNA (Coralville, IA).

The strands used were: 5'- (Cy5) CCTCGAGGGATCCGTCTAGCAAGC - 3' and 5'-GCTCGAGTCTAGACTGCAGTTGAGAGCTTGCTAGGACGGATCCCTCGAGG (IBRQ) -3'. DNA was annealed in phosphate buffer (20 mM phosphate, 50 mM NaCl, pH 7.5). Duplexes were quantified by UV-visible spectroscopy and diluted to reach a final concentration of 1 μ M. Using a Bio-Rad 96-well plate fluorescent themocycler reader, 30 μ L reactions of 5 nM duplex, 500 μ M ATP, and 10-300 nM Rad3 were incubated in assay buffer and monitored over one hour, with scans taken every 30 seconds. Reactions were initiated by addition of ATP. Helicase activity was measured and fit to first-order kinetics to determine rate constants.

DNA-binding experiments

Fluorescence anisotropy was measured using a Flexstation 3 instrument. Rad3-DNA interactions were probed in a reaction mixture of assay buffer with 10 nM fluorescein-labeled DNA (IDT DNA) in 20 μ L reactions using the substrate 5'(fam)CACGTTGACTACCGTC -3'. The protein-DNA mixture was incubated at 30°C for 20 minutes, and fluorescence was monitored at 520 nm for in 30-second intervals for 5 minutes. Polarization data was measured in triplicate and fit to a 4-parameter hill coefficient to determine ssDNA binding constants using kaleidagraph.

***S. cerevisiae* Rad3 knockout generation**

The diploid Δ Rad3 knockout was obtained from the yeast knockout collection (Thermo Scientific). This was transformed with the complementation plasmid containing

the Rad3 gene on PRS316 plasmid. Individual colonies were sporulated and dissected. After performing tetrad analysis, an individual colony capable of growing in SD-URA, geneticin, YPD, and not in the presence of 5-fluoro-orotic acid was stored as the parent yeast knockout strain.

Yeast transformations and plasmid shuffle

Mutations in the PRS313-based plasmids harboring the RAD3 gene were introduced by SDM. The parent yeast strain was grown to an OD₆₀₀ ~ 0.6 in SD-URA. Cells were then pelleted for 30 seconds at 8,000 RPM. The cells were rinsed with water and re-suspended in 160 µL LiOAc buffer (100 mM LiOAc, 10 mM TRIS-HCl pH 7.5, 1 mM EDTA, 1 M sorbitol) and shaken at 30°C for one hour. Next, 2.5 µL of 10 mg/mL salmon sperm DNA (Sigma) was added with 4 µL of mini-prepped DNA (~100 mg/mL) and incubated at 30°C for 30 minutes without shaking. 400 µL of PEG buffer (40% PEG 4000, 100 mM LiOAc, 10 mM Tris HCl, pH 7.5, 1 mM EDTA) was added and incubated at 30°C for 20 minutes without shaking. Finally, yeast were heat shocked at 42°C for 5 minutes and plated 200 µL onto selective media plates (SD –URA – HIS).

Individual colonies were grown in SD-URA-HIS overnight to reach saturation. Next, 40 µL was used to inoculate a 4-mL SD-HIS culture. After 6-8 hours, a 4 mL culture of SD –HIS + FOA was inoculated and allowed to grow overnight. The culture was plated onto SD-HIS plates, and colonies were verified for plasmid shuffle by testing growth in geneticin, YPD, SD-HIS, 5-fluoro-orotic acid, and lack of growth in SD-URA.

Growth curves

All growth curves were performed in a similar fashion. Overnight cultures were grown to stationary phase and used to inoculate a 4 mL culture (1/100th dilution).

Cultures were shaken at 200-220 rpm and grown at 30°C. At indicated time points, an aliquot was removed and diluted accordingly to obtain an OD₆₀₀ using a Cary UV-Visible spectrophotometer.

Colony counting

The typhoon counts colonies through the coomasie setting in fluorescence mode, and colonies counted are consistent with manual counting. Overloaded plates cannot be differentiated, but colony counts between 0 and 200-300 colonies are accurately counted with the software. Typical software parameters are 9000, 9, 19, 500 with splitting colonies set to a factor of 9, giving counts consistent with the manual counts.

UV-survival

Briefly, an overnight culture of an individual colony was grown in SD – HIS to reach stationary phase. A 2 mL culture of 1×10^7 cells/mL (OD₆₀₀ = 0.6) was made and transferred to a small 2 mL petri dish, followed by immediate irradiation. 100 µL of the culture was used to create 10-fold serial dilutions, which were plated onto pre-warmed SD –His plates and incubated at 30°C for 72 hours in the dark, followed by imaging. Colonies were counted, and survival was determined based on the number of viable colonies.

Spotting assays were performed in a similar manner. Serially diluted cultures (5 µL) were plated onto pre-warmed SD –HIS plates and irradiated with 254 nm light. Images were taken after 72 hours of growth at 30°C in the dark.

NQO-survival

Individual colonies were grown to saturation and serially diluted in water. These were then plated on the appropriate SD-HIS + NQO plates and incubated at 30°C for 72-

96 hours. Once colonies were formed, they were counted. Spotting assays were performed in a similar manner. Serially diluted cultures (5 μ L) were plated onto pre-warmed SD-HIS +NQO plates. Images were taken after 72 hours of growth at 30°C in the dark.

Growth curves were obtained starting with saturated cultures, which were used to inoculate (100x) 4 mL of SD-HIS. At the indicated times, anywhere from 50-400 μ L of culture were measured using a Cary spectrophotometer to measure absorbance at 600 nm. These values were then plotted and fit to a 4-parameter hill equation to obtain a $t_{1/2}$.

DNA synthesis

DNA was synthesized as previously described. Standard phosphoramidites were used on an ABI 3400 DNA synthesizer with modifications from Glen Research. DNA was purified by reverse-phase HPLC and solvent removed through lyophilization. Disulfide modified DNA was resuspended in 400 μ L reduction buffer (50 mM Tris, pH 8.0) and reduced with 10 mg of DTT. DNA quantification was based on UV-visible absorbances at 260 nm.

DNA-modified electrochemistry

50 μ M duplex DNA was annealed in degassed phosphate buffer (50 mM phosphate, 100 mM NaCl, 1 mM EDTA, pH 7.5) and allowed to self-assemble on a gold-on-mica surface overnight (Agilent technologies). Excess DNA was washed a minimum of three times from the surface with phosphate buffer. The surface was then backfilled with a solution of 1 μ M mercaptohexanol in protein buffer (200 mM NaCl, 50 mM Tris, pH 8.0, 1 mM EDTA and 5% glycerol). Protein was added to the electrode housing, and electrochemistry was performed using a CH Instruments 600 potentiostat and a 3-

electrode set-up with a Ag/AgCl reference electrode, platinum auxiliary, DNA-modified electrode, and the working surface. All measurements were performed in a glovebag to prevent degradation of the protein cluster and minimize the presence of oxygen.

Results

Isolation of haploid *S. cerevisiae* with a Rad3 knockout for survival studies

An *S. cerevisiae* heterozygous diploid Rad3 knockout was obtained from the yeast knockout (YKO) collection (Thermo Scientific). A plasmid encoding the Rad3 gene was then transformed into the diploid strain. Successful transformations were isolated and grown on SD – URA – HIS, and twelve colonies were sporulated and dissected. Each tetrad was plated on SD –URA, YPD, geneticin, and FOA plates. Tetrad analysis of individual spores identified an individual haploid strain that had Rad3 knocked out and replaced by a kanamycin gene in the genome (Figure 4.2). This was evident by a spore capable of growing on SD – URA, YPD, geneticin, but not on FOA plates.

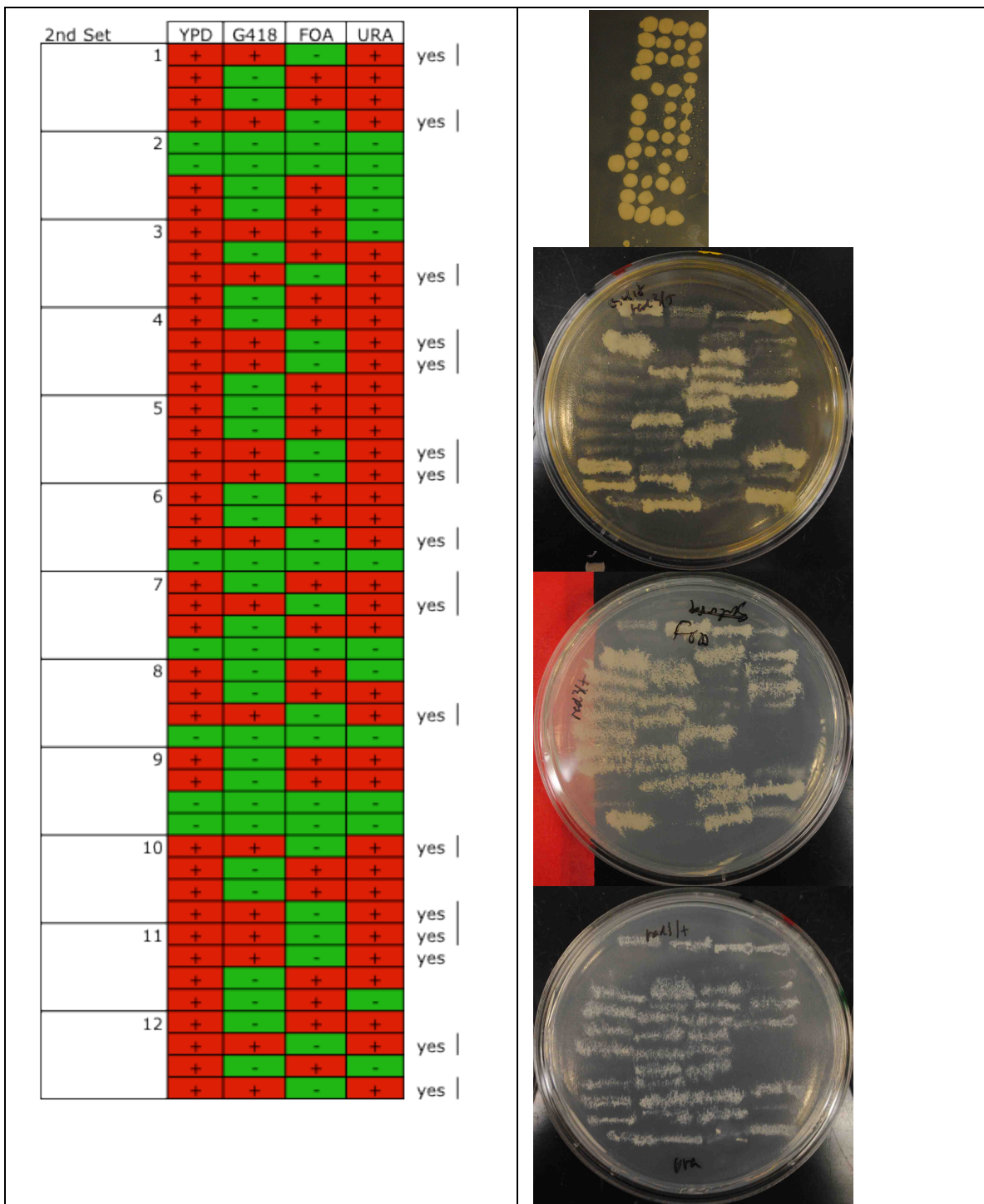


Figure 4.2. Tetrad analysis for generating Rad3 knockout *S. cerevisiae*. Tetrad analysis for 12 individual sporulated colonies on either YPD, G418, FOA or URA. “+” Indicates that the yeast survived, while “-“ indicates that the yeast did not survive on the YPD (top right), geneticin (top middle, right), FOA (bottom middle, right), and SD – URA (bottom, right) plates.

Characterization of Rad3 knockouts

Based on disease-related mutations in human XPD, a series of haploid yeast strains have been isolated (Table 4.1), in which the only difference is the copy of Rad3 that is maintained on the plasmid. In each strain, the gene encoding for Rad3 has been deleted from the genome and been replaced by a kanamycin gene (Table 4.1). The initial strain of *S. cerevisiae* generated is complemented by WT Rad3 on a PRS316 plasmid, which encodes for the URA3 gene and allows for growth in SD – URA. A plasmid shuffle is used to change the copy of Rad3 in the yeast strain. First, a transformation of the mutant Rad3 on a PRS 313 plasmid, which encodes the HIS gene, is accomplished. This leaves copies of both the PRS313 and the PRS316 plasmids in the cell. By changing the media to SD-HIS, the PRS316 plasmid leaves the cell. This is followed by a selection using SD-HIS + FOA, an auxotrophic selection that kills any strain containing the original PRS316 plasmid (Figure 4.4). Individual colonies are then isolated and verified to have the plasmids shuffled by growing in selective medias. If the transformation is successful, mutants will grow in G418 (indicating that the Rad3 gene has been deleted from the genome), SD-HIS (indicating the presence of PRS313), and SD-HIS+FOA (indicating the presence PRS 313 and absence of PRS316). The strains will be incapable of growing in SD-URA (indicating absence of PRS316) as well as SD-URA-HIS (indicating that only the PRS313 plasmid is present).

Mutations for each Rad3 strain were introduced by site-directed mutagenesis on the PRS313 plasmid. Most of the disease-relevant mutations were well conserved between SaXPD, ScRad3, and HsXPD, but a few mutations exist only in ScRad3 and HsXPD due to the complex nature of the eukaryotic proteins. In both *Sulfolobus*

acidocaldarius and humans, the L325 (Sa) and L461 (human) correspond to I463 (Sc). Furthermore, in human patients, the L461V mutation is often accompanied with a deletion of amino acid 716-730 in the c-terminal region. A site-directed mutagenesis method was used to generate the corresponding I463V/del716-730 (I463V/Δ) mutation in ScRad3.

To verify that Rad3 is essential for survival, each strain was grown in both SD-HIS and SD-HIS+FOA. If the original WT plasmid is present, the strain will show reduced growth in SD-HIS+FOA. This only occurs in strains that lack a viable copy of Rad3. In this case, the cell would adapt to survive in the presence of FOA. As shown in Figure 4.5, all strains grow similarly to the WT strain in both SD-HIS and SD-HIS+FOA, with the exception of the empty plasmid. This indicates that all mutant copies of ScRad3 generated are viable.

Growth curves were performed on each strain to verify that mutations in Rad3 do not lead to any growth defects *in vivo*. The majority of the strains grow at a rate within that of the WT Rad3 strain, however the R618P and the empty plasmid strains grow significantly slower (Figure 4.5, purple and green curves). The empty plasmid does not grow as well because Rad3 is an essential gene. The growth defect in R618P suggests that this mutation in Rad3 significantly alters the survival characteristics of this yeast strain. The strain not only grows slowly, but also reaches a lower cell density ($OD_{600} \sim 5.0$) compared to the WT strain ($OD_{600} = \sim 6.0$).

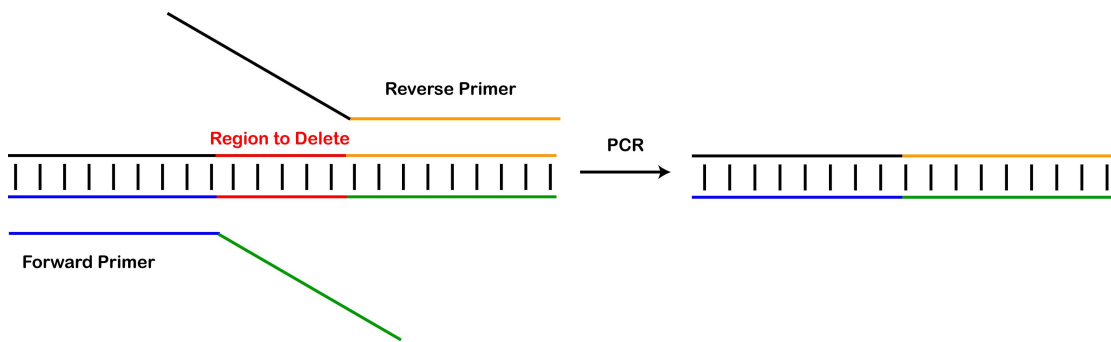


Figure 4.3 PCR based SDM strategy for the deletion of regions of a plasmid.

Forward and reverse primers were designed to delete the region in red. Primers were designed to be homologous to the forward region (blue) and the tail region (green) on the forward primer and complementary to the orange region and black regions on the reverse primer.

Yeast Strain	Rad3 Copy	SaXPD Mutation
A-1*	WT	L325I
B-1	I463V	L325V
C-1	G47R	G34R
E-1	C665R	A511R
F-1	(p)	--
G-1	I463V/M468A	L325V/M331A
H-1	I463F	L325F
I-1	I463L	WT
J-1	I463V/del716-730	L325V/del
K-1	WT/del716-730	WT/del
L-1	R618P	R460P
M-1	R618W	R460W
N-1	I463V/M468A/del716-730	L325V/M331A/del
O-1	R618A	R460A
P-1	R618E	R460E
Q-1	R618L	R460L
R-1	R618Y	R460Y

Table 4.1. Yeast strains generated with variants in Rad3 compared to SaXPD alignment. *Note, that in SaXPD L325 aligns with I463 in ScRad3.

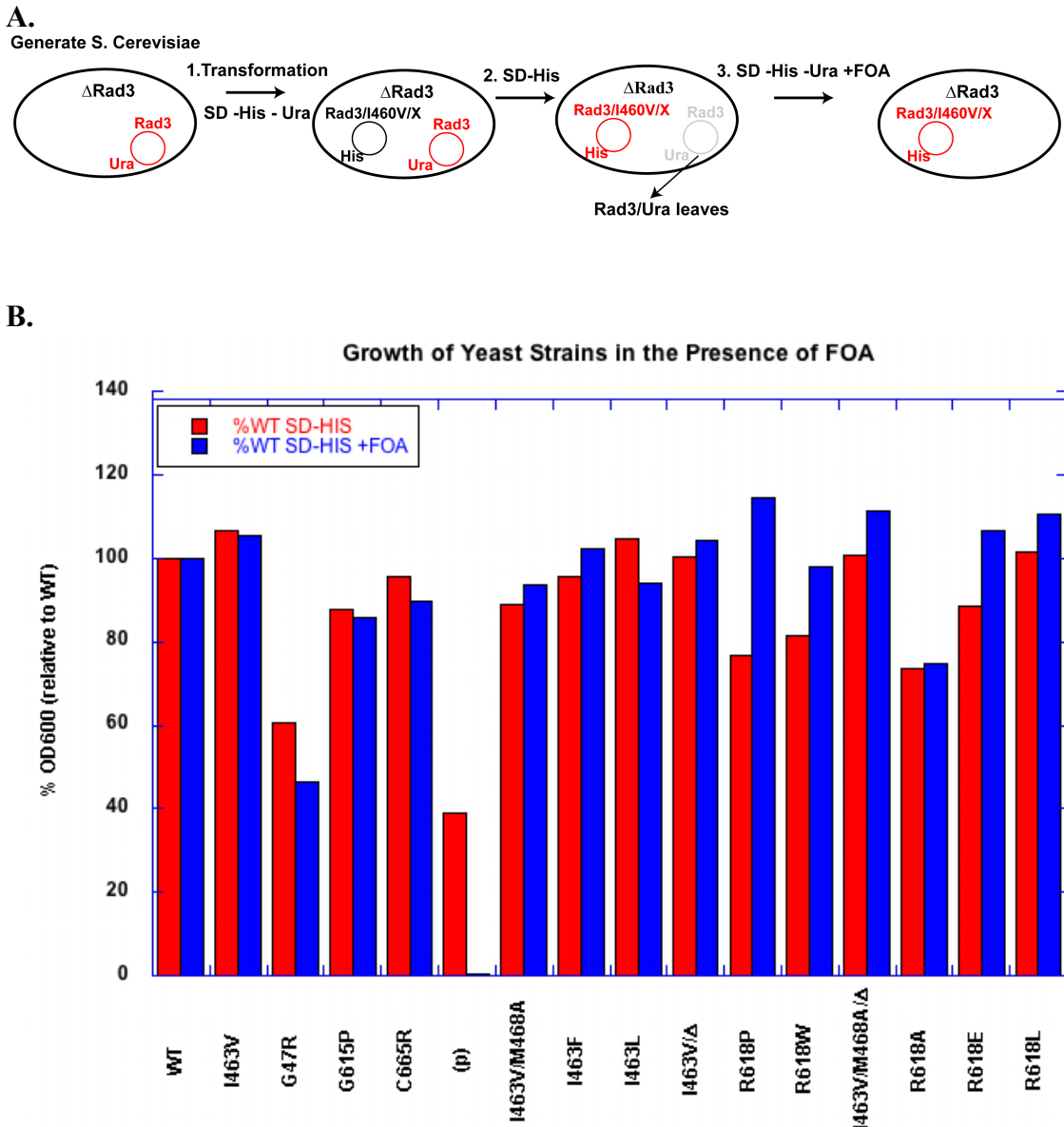


Figure 4.4 Rad3 mutant viability by the plasmid shuffle. (A) Cartoon Schematic for plasmid shuffle to isolate *S. cerevisiae* containing mutants of Rad3. Briefly, WT Rad3 is encoded on a plasmid containing the URA3 gene into haploid yeast with Rad3 deleted from the genome. Mutants of Rad3 are encoded onto a plasmid encoding the HIS gene and transformed into the original cells. The media is then shifted to only SD-HIS to remove the original plasmid and then counter-selected in FOA to ensure the removal of the WT copy of Rad3. (B) OD₆₀₀ measurements of individual yeast strains grown in both SD-HIS and SD-HIS + FOA (normalized to WT). The strain containing the empty plasmid is inviable when grown in the presence of FOA, confirming the fact that Rad3 is an essential gene. All of the other individual point mutations are viable.

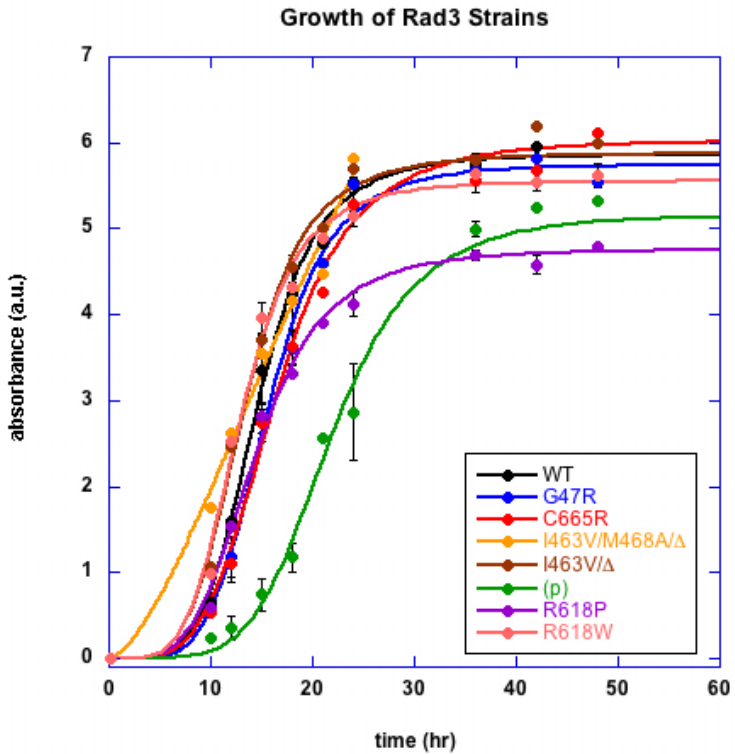


Figure 4.5. Growth curves of Rad3 strains in SD-HIS. Strains were monitored for growth by absorbance OD₆₀₀.

UV-Survival assay

An easily-generated NER product is the cyclopyrimidine dimer (CPD), which can be formed by irradiating DNA at 254 nm. Even a single CPD dimer can have disastrous downstream consequences (2, 3). The yeast genome is approximately 12,000,000 base pairs (32). UV damage generates approximately 6700 CPDs per 60 J/m² of 254 nm UV-light (33). Based on this, we calculated the number of CPDs generated during irradiation. Assuming an average distribution of damage, we then determined the average distance between dimer sites (Figure 4.6). Under conditions of high irradiation (200 J/m²) the average distance between dimers is only 700 base pairs.

To understand how the Rad3 mutations perform *in vivo* in response to NER damage, we performed a UV-survival assay measuring survival after 200 J/m² UV-light on the WT, G47R, I463L, I463V, and I463V/Δ mutant strains. The G47R strain shows no noticeable growth (Figure 4.7). The WT Rad3 shows survival at 12.7 ± 0.7%, whereas a simple I463L mutation leads to a small increase in viability 19.3 ± 2.0%. In contrast, when mutated to a valine, a known disease mutation in humans when combined with a c-terminal deletion, the strain survives only 11.2 ± 0.3% when UV-irradiated. The I463V/M468A mutant, which exhibited mildly improved CT (Chapter 3), survives at about 14.3 ± 0.6%, better than both the WT and I463V mutant strains (Figure 4.7). Perhaps by generating large amounts of DNA damage we have amplified the small differences between these strains.

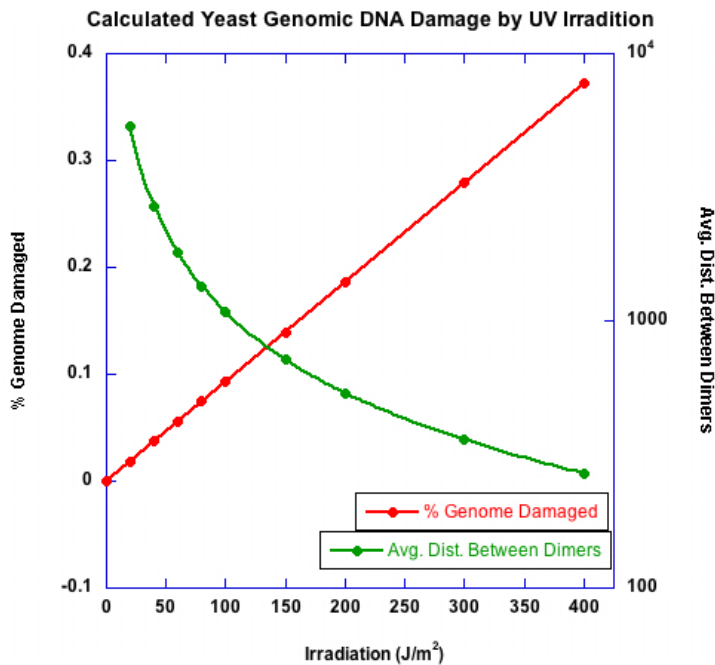


Figure 4.6. Calculated thymine dimer damage in yeast *S. cerevisiae*. Calculation based on 6700 thymine dimers generated per 60 J/m² UV irradiation with a yeast genome of 12 million basepairs. In red is the % of genome expected to be damaged given the amount of irradiation, while in green is the average distance between dimers based on the number of damage sites and total size of the genome.

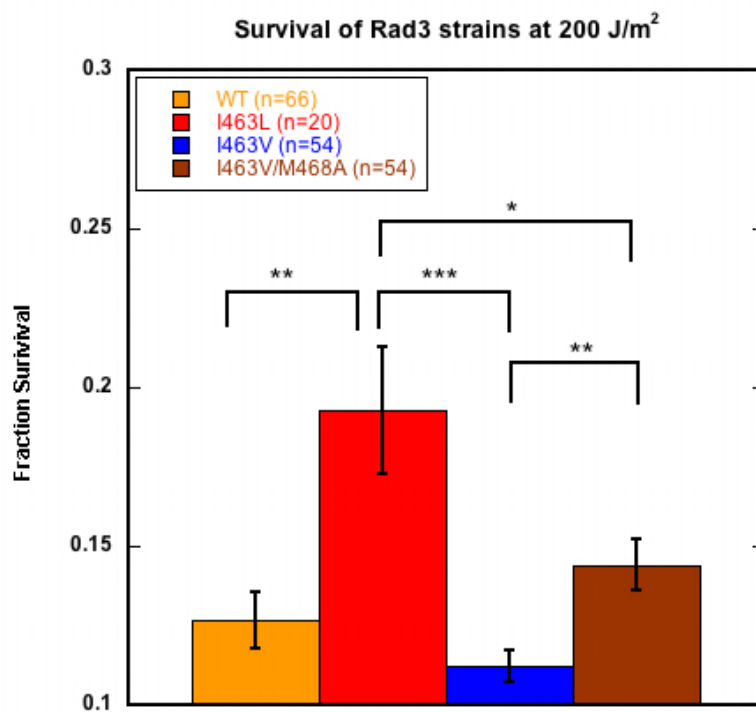


Figure 4.7. UV-survival of Rad3 strains at 200 J/m². Survival of WT (orange), I463L (red), I463V (blue) and I463V/M468A (brown) yeast strains after 200 J/m² UV dosage. Fraction survival is measured relative to the unchallenged samples. Standard error is shown and based on the number of individual samples measured. For p-values, * = p <0.05; ** = p <0.01; *** = p <0.001

NQO-Surival Assay

4-Nitroquinoline 1-Oxide (NQO), a UV mimic that generates quinol-base adducts that must be repaired by NER, was used to chemically mimic the UV-survival assay, as a chemical damaging agent provides more control over the amount of damage the cells receive. Using the WT, G47R, I463V/Δ, R618P, R618W, and C665R mutant yeast strains, survival was measured when grown in the presence of 20 ng/mL, 100 ng/mL, and 200 ng/mL NQO (Figure 4.8). The G47R, R618P, and C665R mutant strains show no noticeable growth at 20 ng/mL NQO. At 200 ng/mL NQO the WT strain survives at $1.5 \pm 0.38\%$, while the I463V/Δ and R618W strains survive at $0.23 \pm 0.01\%$ and $0.32 \pm 0.09\%$, respectively. These mutations all show growth defects *in vivo* relative to the WT strain.

To investigate the kinetics of repair, growth of these mutant strains was measured in the presence of 20 ng/mL NQO. When the strains are not challenged with NQO, they all reach log phase within 14-16 hours (Figure 4.9). In the case of the WT, I463V/Δ and R618W strains a shift in $t_{1/2}$ of about 1-2 hours occurs when grown in 20 ng/mL NQO. However, the G47R, R618P, and C665R strains show shifts of about 30 hours, indicating attenuated growth. Based on alignment with the SaXPD and HsXPD proteins, these mutants are expected to be ATPase and helicase deficient. Therefore, these growth defects are likely a result of their diminished biochemical activity. Because all of our biochemical knowledge of Rad3 either comes from SaXPD or XPD cell lysates, it is essential to obtain the Rad3 protein to verify this biochemical deficiency.

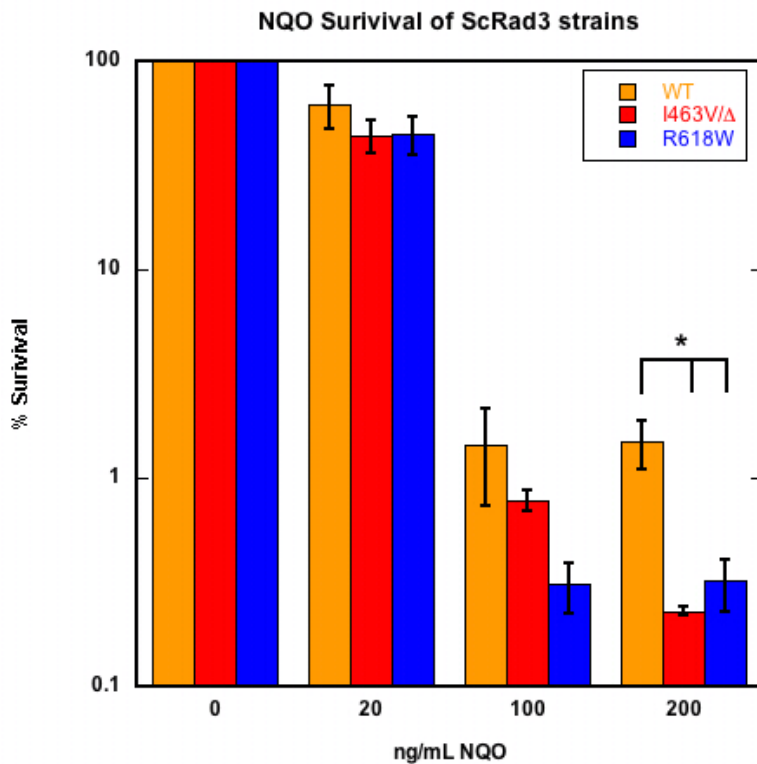


Figure 4.8 NQO-survival assay of Rad3 mutants. WT (orange), I463V/Δ, and R618W *S. cerevisiae* Rad3 mutant strains are shown. Viable colonies were counted and compared to the plates lacking NQO to produce survival percentages. The G47R, R618P, and C665R mutant strains show no noticeable growth. In both cases at 200 ng/mL NQO the mutant forms of Rad3 do not survive as well as WT. * p <0.05

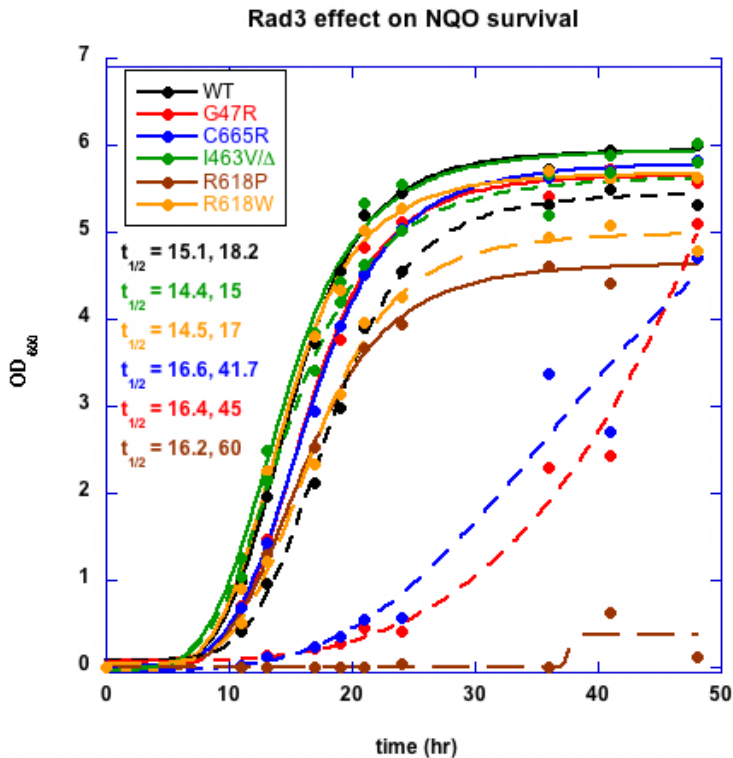


Figure 4.9 Effect of NQO on growth for Rad3 strains. OD₆₀₀ was measured for WT (black), R618P (red), and R618W (blue) Rad3 mutant strains. The dashed lines represent strains where NQO was added at 200 ng/mL. In the WT and R618W strains, the $t_{1/2}$ changes from 15.1 to 18.2 hours and 14.5 to 17.0 hours, respectively, while in the case of R618P, this changes from 16.2 to 60 hours, suggesting that NQO plays a devastating effect in R618P.

Mutations at R618 in *S. cerevisiae* Rad3 show variable growth in response to NQO

The R618P and R618W Rad3 mutations exhibit very different growth phenotypes. Recently, a cerebro-oculo-facio-skeletal syndrome patient was found to have an R618Q found in their XPD gene (34). To determine how these mutation affect growth, we modeled various amino acid substitutions using the SaXPD crystal structure (Figure 4.10). Five amino acid substitutions were made that have an effect on either charge, aromaticity, or sterics. By replacing the arginine with a leucine (slightly hydrophobic), glutamate (negatively charged), alanine (loss of side chain), or tyrosine (aromatic), we expected to observe variances in survival. We hypothesized that the negatively charge glutamate should repel DNA binding and therefore have reduced viability, while the aromatic tyrosine should behave similarly to WT.

In an NQO-survival assay (Figure 4.11), each disease-related strain shows attenuated growth relative to the WT strain. The G47R, R618P, and C665R strains show less than 0.0001% growth on plates containing 20 ng/mL NQO. When examining the mutations at R618 we found that survival is in the order of proline < glutamate < alanine < tryptophan < tyrosine ≈ leucine ≈ arginine (WT). This is likely due to the large structural changes associated with proline, as well as the change in charge by introducing the negatively charged glutamate. Alanine removes any side chain functionality, which presumably disrupts the protein-fold. This residue is therefore important, as subtle changes drastically affect survival in these yeast strains.

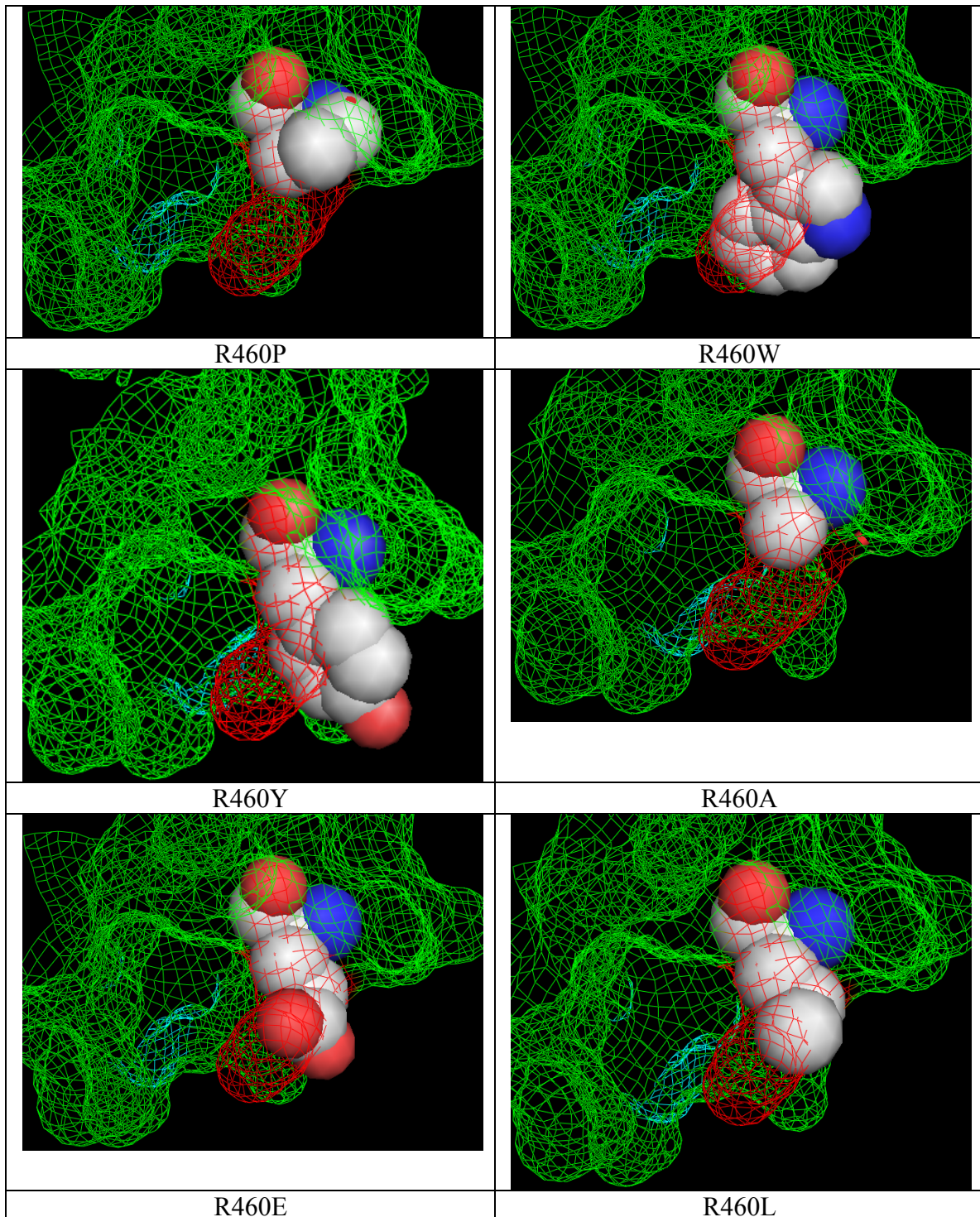


Figure 4.10 Pymol representations of mutations at the R460 position in SaXPD. In red mesh is the original leucine, while the colored spheres represent the mutations indicated. Based on the SaXPD crystal structure (PDB ID 3CRV), the analogous mutations were made in Rad3.

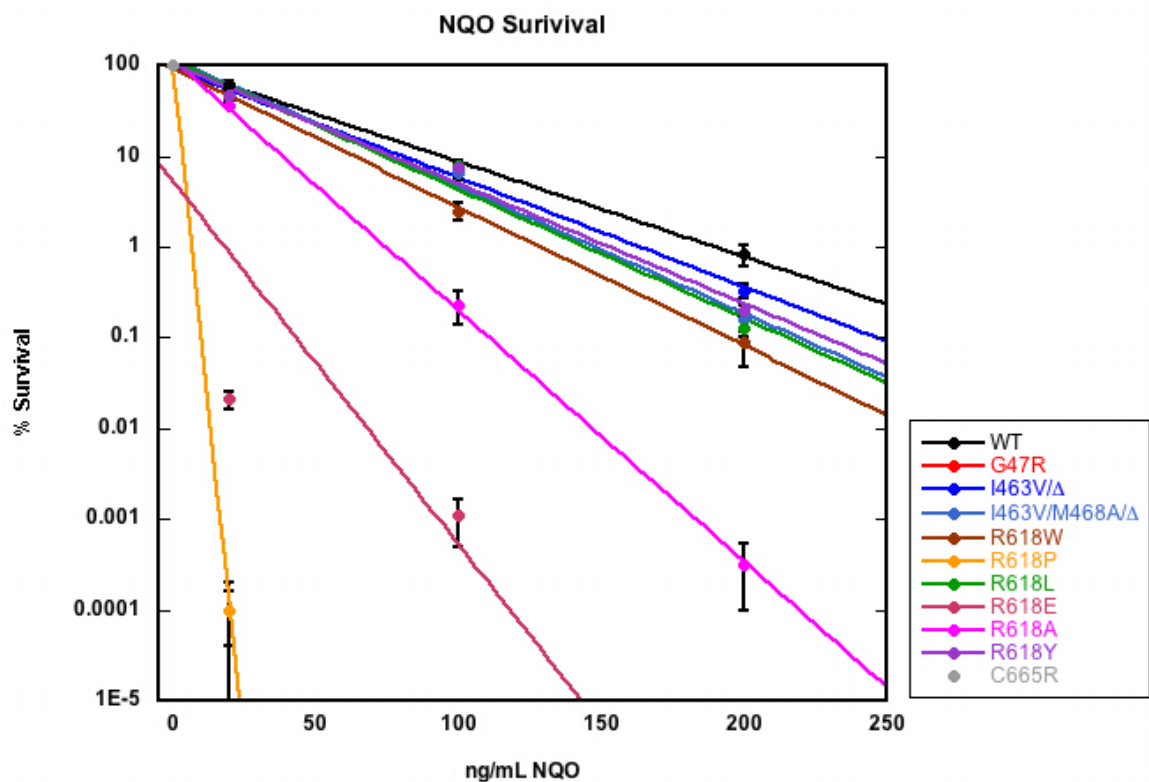


Figure 4.11. NQO survival assay for WT (black), G47R (red), R618W (brown), R618P (brown), R618L (green), R618E (mauve), R618A (fuscia), R618Y (purple), I463V/Δ (blue), I463V/M468A/Δ (light blue), and C665R (gray) Rad3 strains. Note that for G47R, R618P, and C665R, minimal growth was observed at 20 ng/mL.

Effect of Rad3 mutants in survival from non-NER DNA damaging agents

Spot assays provide a quick and easy means for assaying viability for a variety of targets. Typical substrates for NER are bulky lesions such as thymine dimers or quinoline adducts to guanine and adenine in the DNA. Methyl methanesulfonate (MMS) methylates DNA and leads to a double strand break; camptothecin (CPT) is a natural product that induces a covalent crosslink between DNA and topoisomerase I. This lesion must be end resected and also leads to double strand breaks and collapsed replication forks; hydroxyurea (HU) inhibits DNA replication and leads to stalled replication forks. The chemical structures of these DNA damaging agents are shown Figure 4.12. Rad3 may be responsible for repairing lesions not previously linked to NER. To test the ability of Rad3 mutants to repair DNA damage, spot assays were performed with either CPT, MMS, or HU(35) (Figure 4.12). In the presence of HU, which inhibits DNA synthesis, all mutations show attenuated growth. When grown in the presence of MMS, the G47R mutation shows attenuated growth.

To observe the kinetics of repair, growth curves of the WT and G47R Rad3 mutant strains were grown in the presence of the DNA damaging agents. As shown in Figure 4.13, WT Rad3 exhibits only small changes in growth rates for NQO, MMS, and CPT, but shows a slower rate of growth in the presence of HU. The ATPase/helicase deficient G47R mutant exhibits different growth patterns in the presence of these DNA damaging agents. When the G47R strain is challenged with NQO, an NER damage agent, $t_{1/2}$ changes by over 40 hours (from 16 to 42 hours). HU slows the growth of the G47R strain similarly to the WT strain, suggesting that they act similarly on stalled DNA replication forks. However, when MMS or CPT were added, the G47R strain has a shift in $t_{1/2}$ of 8 and 3 hours respectively, a result not found with the WT strain. The change in

growth rate can be attributed to Rad3 assisting in the repair of these lesions. It is highly likely that the helicase activity of the protein can be utilized in opening DNA around the sites of lesions.

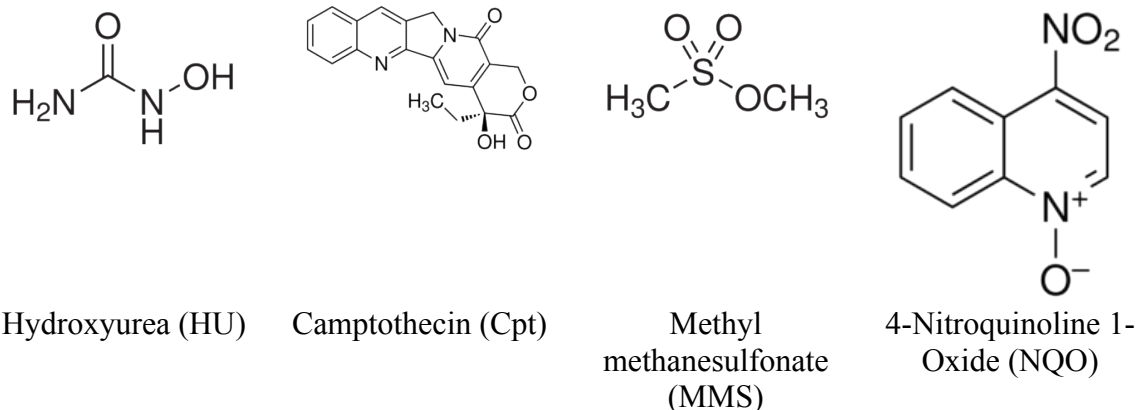
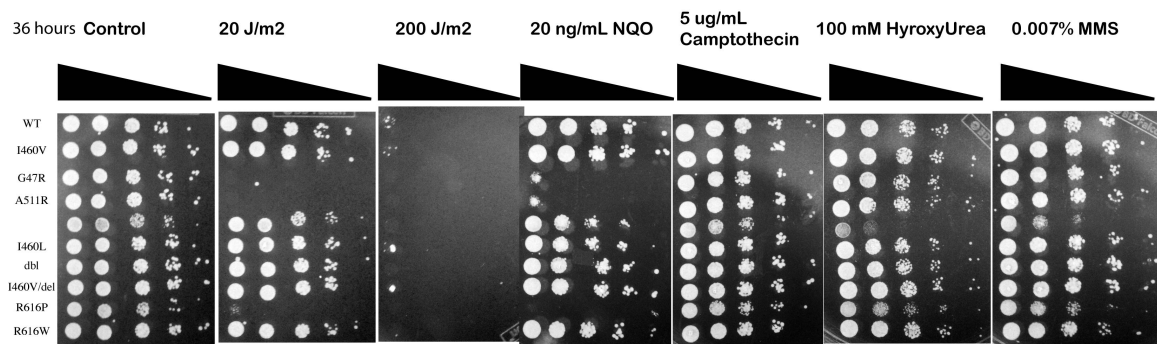
A**B.**

Figure 4.12. Spot assay for Rad3 mutant strains with DNA damaging agents. **A.** The chemical structures of the DNA damaging agents. **B.** 10-fold dilution spot assays for strains indicated on SD-HIS plates with appropriated DNA damaging agent. Images were taken 36 hours after plating or exposure.

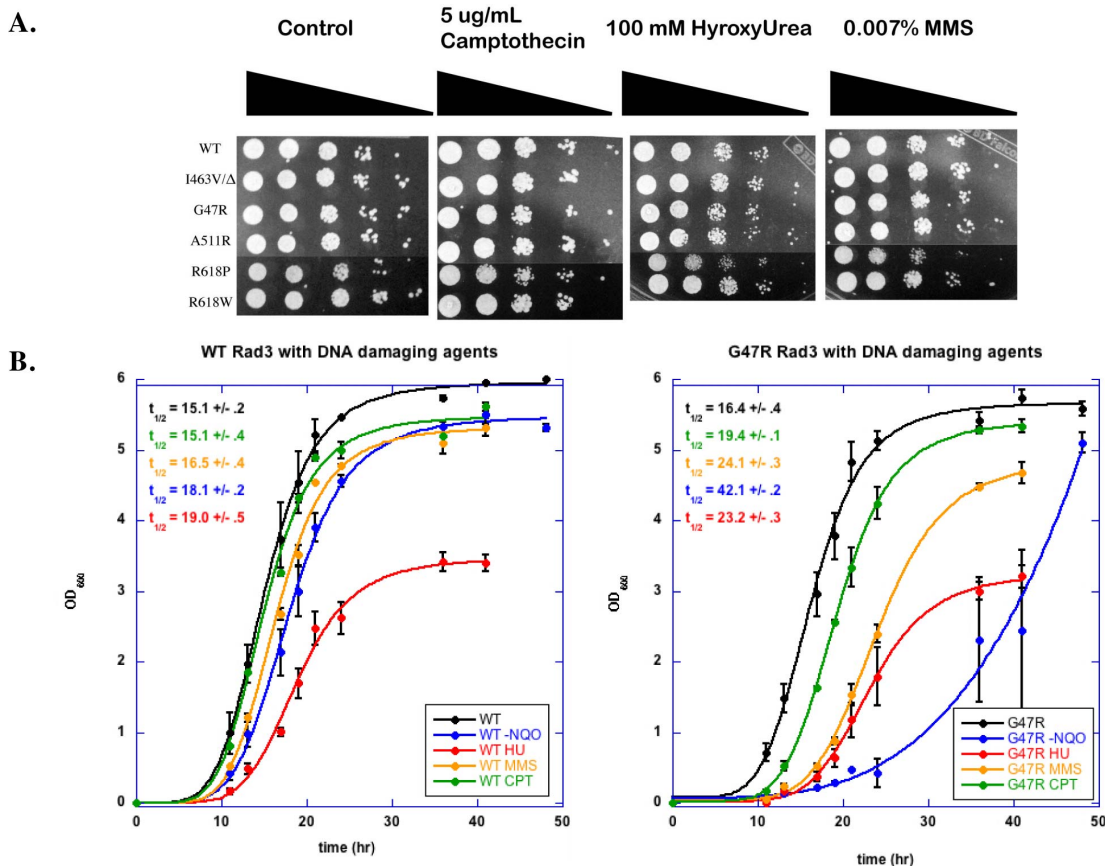


Figure 4.13 Effect of DNA damaging agents on Rad3 mutant *S. cerevisiae* strains. A. Serial dilutions of Rad3 mutant *S. cerevisiae* strains with mutations as indicated. Each mutant was 10-fold diluted on SD-HIS plates with either CPT (5 μ g /mL), 100 mM HU, or 0.007% MMS. **B.** Growth curves of WT (left) or G47R (right) Rad3 *S. cerevisiae* strain in SD-HIS (black) with 20 ng/mL NQO (blue), 100 mM HU (red), 0.007% MMS (yellow), or 5 μ g/mL CPT (green). Data are fitted to a 4-parameter hill equation, and $t_{1/2}$ is shown for each of the strains.

qPCR to monitor transcription of DNA repair genes in Rad3 mutations of *S. cerevisiae*

Quantitative PCR (qPCR) is a powerful tool to measure transcription in an organism. Briefly, mRNA transcripts are isolated from each of the strains of *S. cerevisiae* with a Rad3 mutant. These are then reverse transcribed into cDNA to produce stable copies of the mRNA transcripts, which are amplified using Sybr Green Mix (Roche) and analyzed as previously discussed. The genes of interest are shown in Table 4.2, with primers listed in Appendix 1. Genes were selected because of their interactions with Rad3 or their proposed role in DNA repair, especially proteins that have been shown to contain a [4Fe-4S] cluster such as Pol1, 2 and Pol3. It is therefore crucial to understand how mutant forms of Rad3 affect regulation of the key genes involved in DNA repair.

Gene transcription levels were monitored in strains with or without NQO (200 ng/mL) for 10 minutes. The samples were normalized to the Alg9 reference gene. Changes are shown as a heat map for each of the *S. cerevisiae* Rad3 strains (Figure 4.14). Isa1, Isa2 Met18, Pol2, Pol3, Rad1, and Rad3 transcription levels remain constant, even when challenged with NQO. However, Pol1 and Rfc1 show increases across all strains, likely because Rfc1 and Pol1 are required at the initial stages of DNA repair. Finally, the Rad2 gene, the XPG nuclease responsible for cleaving an NER substrate, appears to be up-regulated by at least a factor of 1.2 in the G47R, I463V/Δ, R618P, and WT strains. DNA repair genes are therefore not heavily up-regulated in response to DNA damage; in fact, mutant forms of Rad3 have little to no effect on these DNA repair genes.

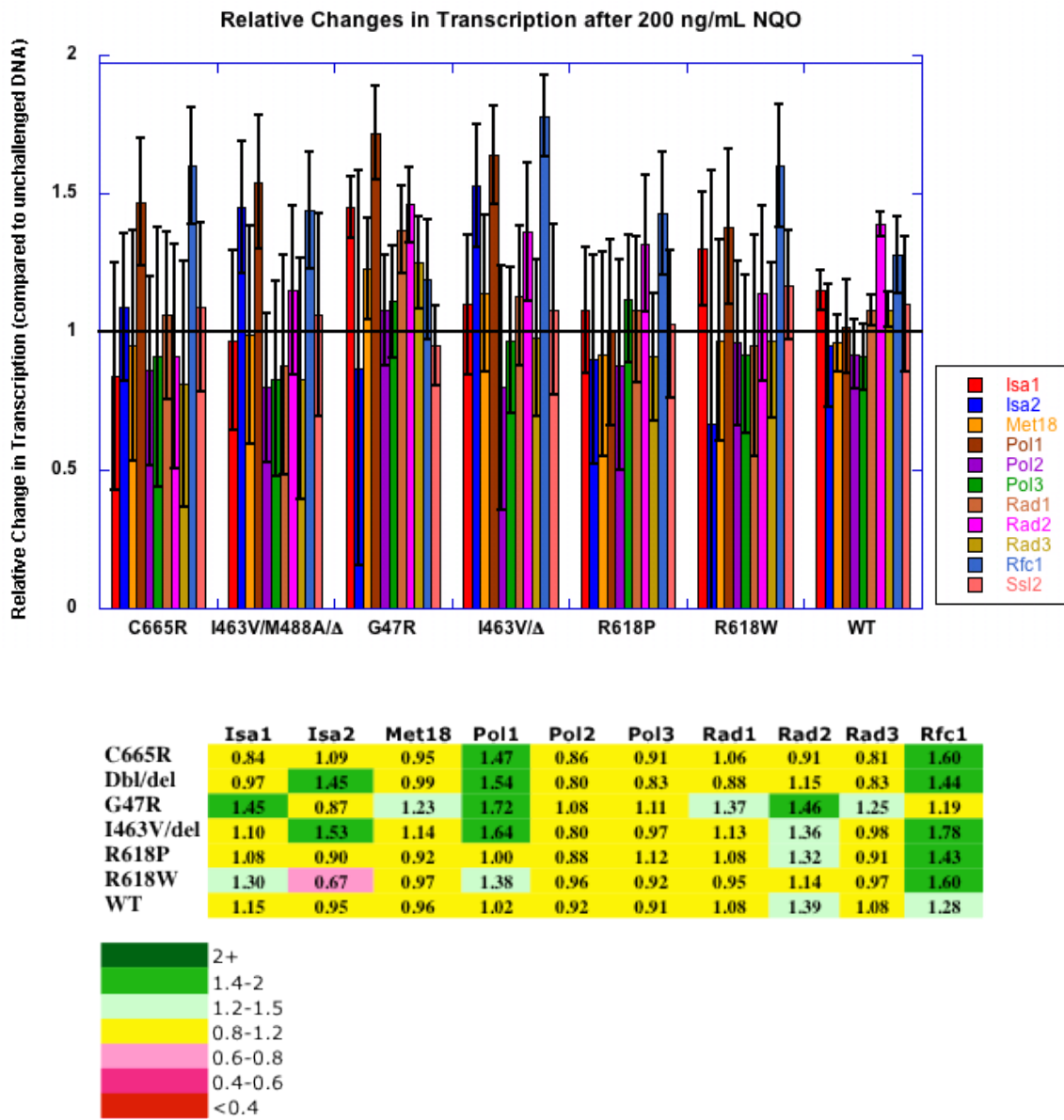


Figure 4.14. qPCR of DNA repair genes in mutant Rad3 *S. cerevisiae* strains. qPCR of genes involved in DNA repair in response to a 10 minute dose of 200 ng/mL NQO. (Top) Relative changes in transcription level for each of the Rad3 strains after NQO addition. (Bottom) Heatmap showing trends of Pol1 and Rfc1 upregulation in Rad3 strains, while little to no upregulation is observed when DNA damage is induced. Upregulated genes are shown in green, while down-regulated genes are shown in red.

Gene	Protein/Function
Ssl2	XPB (helicase)
Rad1	XPF homolog
Rad2	XPG homolog
Met18	MMS19 ortholog
Rad50	
Isa1	Protein required for maturation of mitochondrial [4Fe-4S] proteins; functions in a complex with Isa2p and possibly Iba57p; isa1 deletion causes loss of mitochondrial DNA and respiratory deficiency; depletion reduces growth on nonfermentable carbon sources; functional ortholog of bacterial A-type ISC proteins
Isa2	Protein required for maturation of mitochondrial [4Fe-4S] proteins; functions in a complex with Isa1p and possibly Iba57p; localizes to the mitochondrial intermembrane space, overexpression of ISA2 suppresses grx5 mutations
Pol1	DNA Polymerase α
Pol2	DNA Polymerase ϵ
Pol3	DNA Polymerase δ
Pol30	PCNA
Rfc1	RPA component
Act1	Actin
Alg9	Mannosyltransferase
Tfc1	Subunit of RNA polymerase III
Pda1	Subunits of Pyruvate Dehydrogenase
Rad3	XPD (helicase)

Table 4.2. *S. cerevisiae* genes involved in DNA repair. Table summarizing the targets for a qPCR experiment designed to assess the changes in transcription when various Rad3 mutant strains are challenged with NQO (200 ng/mL).

Isolation of *S. cerevisiae* Rad3

Our *in vivo* results indicate that mutations in the Rad3 protein have detrimental effects on viability of *S. cerevisiae*. While some studies describe the biochemical activity of Rad3 from a purified cell lysate and with purified analogous thermophilic proteins, few have examined the biochemical activity of mutant Rad3 proteins. To understand the biochemical properties of Rad3 from *S. cerevisiae*, we developed a new purification of the protein. Increased production of the protein was attempted by varying time, temperature, and IPTG amount, which is used to induce overexpression. Small induction trials were performed by incubating at either 16°C, 22°C, or 37 °C. Cells were induced with either 100, 200, 400, or 1000 µM IPTG, and time points were taken between 0 and 16 hours (data not shown). In all constructs, little to no overexpression of ScRad3 was observed (Figure 4.15, cell lysate lane). However, through a 4-column purification using a histrap, desalting column, heparin column, and size exclusion column, a band corresponding to ScRad3 was isolated. This band elutes with a retention volume of ~120 mLs, which is early for a protein that is 135 kDa (Figure 4.15). This means that the protein may be forming aggregates or binding to other proteins as it elutes. Aggregation and other protein binding increases the radius of the protein, allowing it to pass through the gel filtration column easily. Minimizing interactions with other proteins and preventing aggregation is the next step in obtaining purified ScRad3.

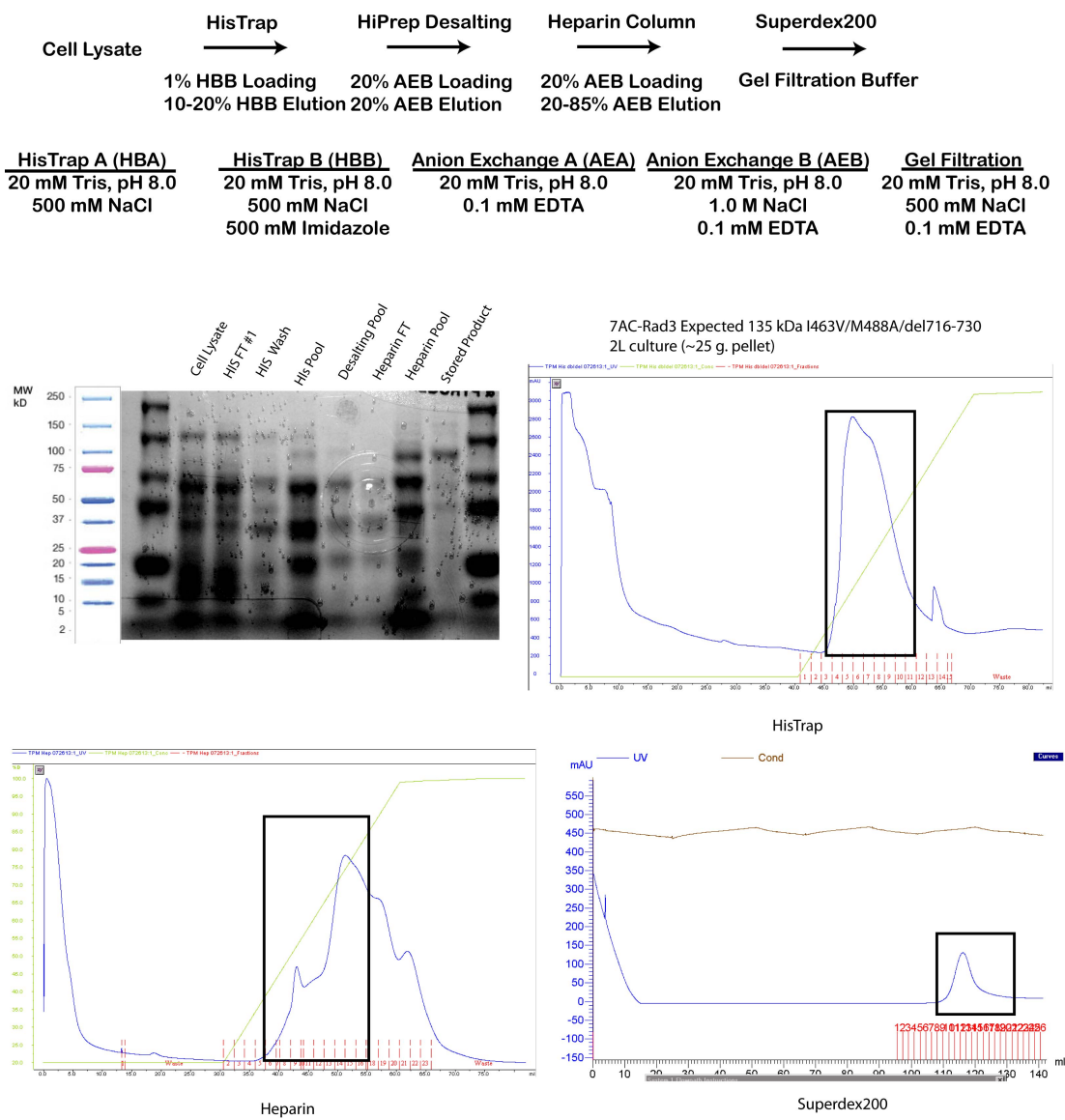


Figure 4.15. Representative protein purification for ScRad3 . (Top) Flow diagram depicting columns attempted in this purification. (Bottom) 7.5% SDS-PAGE gels of fractions indicated. FPLC traces of fractions indicated. Boxed area indicates pooled fractions.

Biochemical characterization of *S. cerevisiae* Rad3

Rad3 mutants were generated by using site-directed mutagenesis and isolated and purified from *E. coli*. Mutants were characterized by UV-Vis to both verify the presence of a [4Fe-4S] cluster and quantify the protein. Figure 4.16 shows a representative UV-Vis trace of WT ScRad3. Protein identities were verified by trypsin digest and MS/MS (PPMAL Caltech). Purity was estimated by the A₂₆₀/A₂₈₀ ratio, which is indicative of nucleic acid contamination. For all mutants, the ratio was less than unity (less than 5% nucleic acid contamination). Concentrations were additionally confirmed by a BCA assay (Bio-Rad).

ATPase activity was verified using a BIOMOL green assay (Enzo Life Sciences), which measures the production of free phosphate. Each protein mutant was incubated in ATPase buffer in either the presence or absence of ssDNA in a 96-well plate. The reactions were incubated at 30°C for 60 minutes and quenched with Biomol green reagent. Colorimetric response was compared to a standard curve to determine the amount of ATP consumed. Figure 4.17 shows ATPase activity of ScRad3, SaXPD and no protein immediately after Rad3 purification. ScRad3 hydrolyzes 52% of the available ATP, while SaXPD hydrolyzes 89% of available ATP. A similar ATPase assay was performed after generating various ScRad3 mutants. The C665R mutant has no detectable ATPase activity, while the G47R, R618P, R618W, and I463V/Δ mutations have 38%, 29%, 57%, and 38% of WT ATPase activity, respectively. However, each of the mutants has diminished ATPase activity (less than 10% of available ATP) (Figure 4.18). Therefore, at -80°C the protein is unstable in the storage buffer and loses ATPase activity.

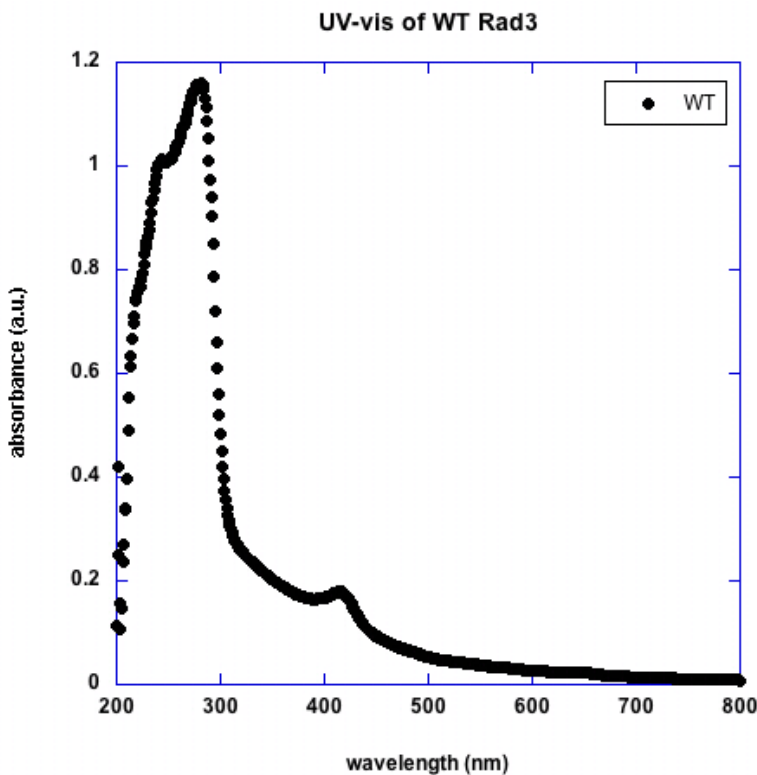


Figure 4.16. Representative UV-vis spectra of ScRad3. Absorbance at 410 nm is used for quantification using $\epsilon = 17,000 \text{ M}^{-1}$.

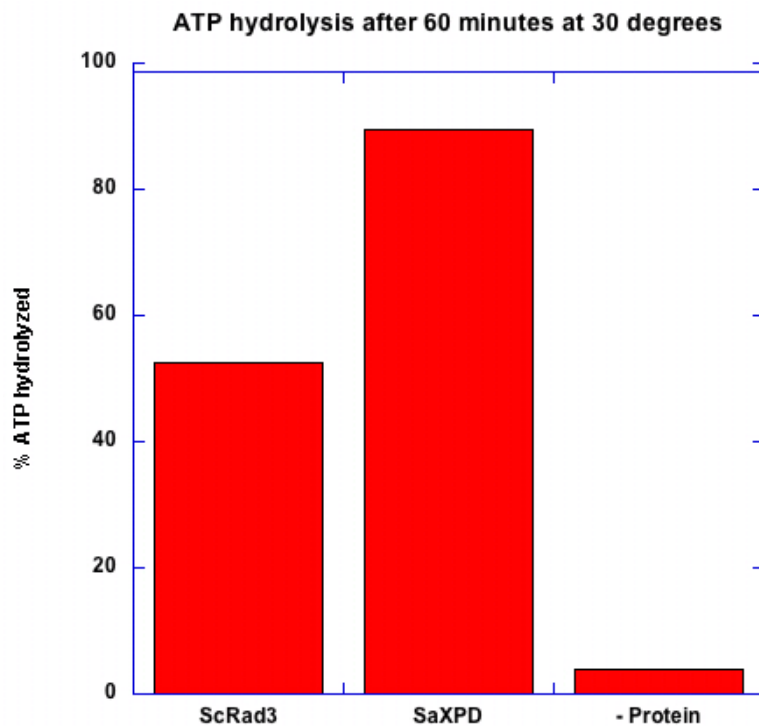


Figure 4.17 ATPase activity of ScRad3, SaXPD. ATPase activity measured after 60 minute incubation at 30°C.

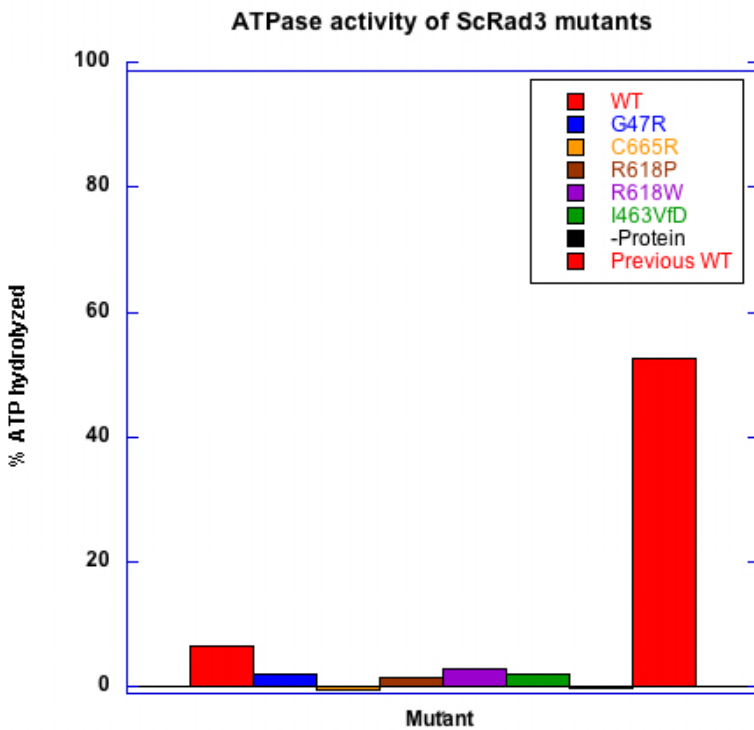


Figure 4.18. ATPase activity of Rad3 mutants after storage. 1 pmol Rad3 was incubated with 2500 pmol of ATP. Release of free phosphate was measured with BioMol green. ScRad3 WT (red), G47R (blue), C665R (orange), R618P (brown), R618W (purple), I463V/ Δ (green) mutants, and no protein (black) were incubated at 30°C for 60 minutes. In red is the previously shown value for WT ScRad3 (Figure 3.20).

Helicase activity more definitively confirms Rad3 activity compared to ATPase activity, as there are only a few helicases in the cell. A fluorescent helicase assay was designed using a Cy5 fluorophore and Iowa Black quencher. When the duplex is annealed, little to no fluorescence is observed. However, upon unwinding of the strands by the helicase, the Cy5 signal is observed. As shown in Figure 4.19, without the addition of protein, a negligible amount of fluorescence increase is observed. As a control, a melting temperature is measured after all assays. In the case of no unwinding (duplex only), a melting transition is observed at approximately 72°C. However, when the substrate is fully unwound, as with Rad3 addition (black line) or ssDNA with a fluorophore (red curve), there is a linear decrease in fluorescence. As a control, we also observed SaXPD helicase activity; as SaXPD is a thermophile, it functions at higher temperatures. Minimal unwinding is observed at room temperature, but as the temperature is increased a new melting temperature at ~52°C is observed (Figure 4.19).

Figure 4.1 shows helicase activity for each of the ScRad3 mutants. Activity was measured as a function of fluorescence over 60 minutes. The WT, R618W, and I463V/Δ unwind the entire substrate, 102%, 110%, and 92.5%, respectively, while the G47R, C665R, and R618P show diminished helicase activity, less than 50% (Table 4.3). This could be a result of protein aggregation or other proteins present that have the ability to unwind DNA.

A titration was performed to determine the DNA-binding constant for ScRad3 to ssDNA using fluorescent DNA. A representative titration is shown in Figure 4.20. All protein mutants bind with low nM affinity ($K_d \sim 40-125$ nM), as helicases are required to open duplex DNA and must bind tightly to DNA.

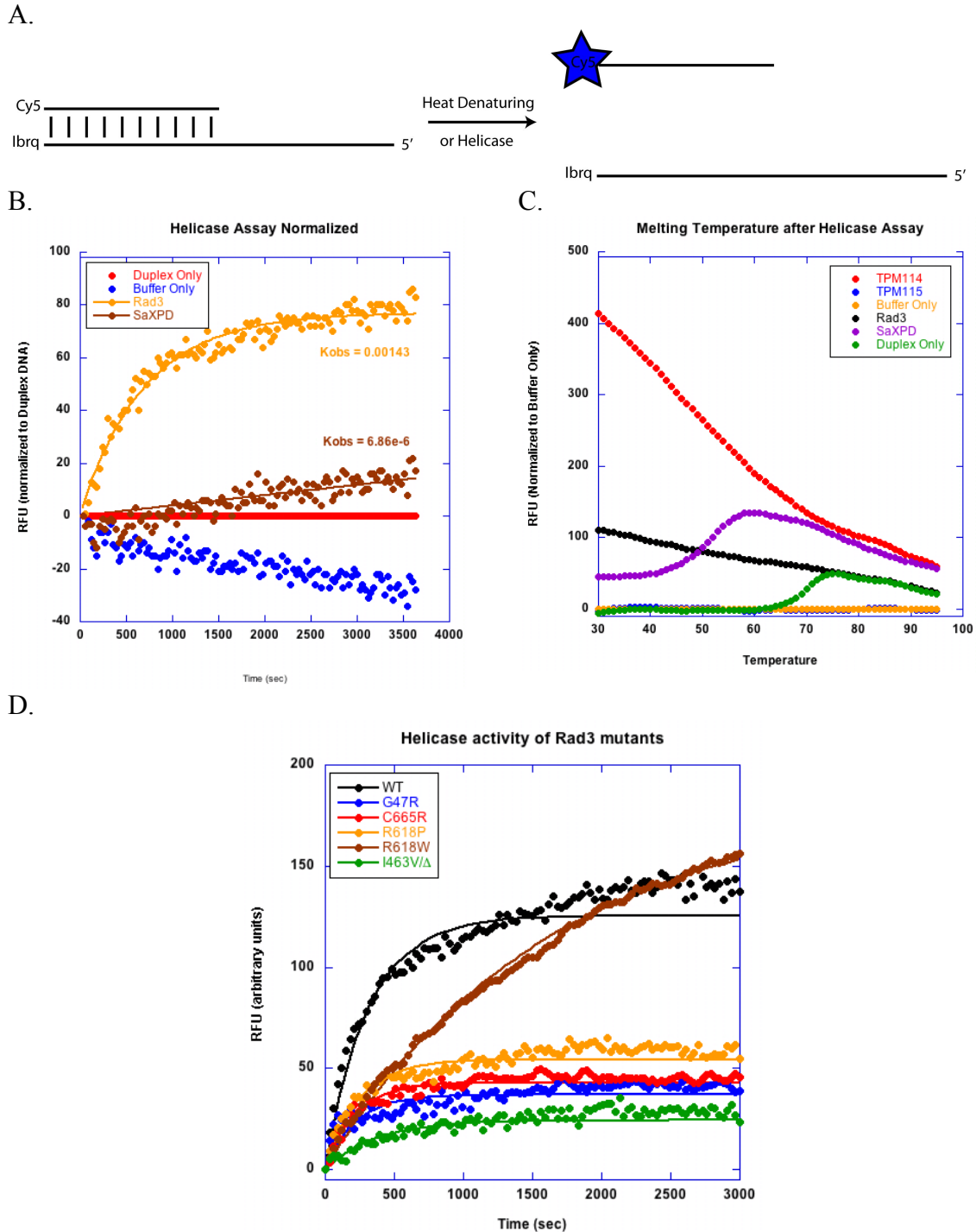


Figure 4.19. Fluorescent helicase activity of Rad3 mutants. (Top) Cartoon schematic of fluorescent helicase assay. (Bottom) Time course experiments for Rad3 mutants incubated with the substrate shown above. Note that only for active helicases do we observe activity.

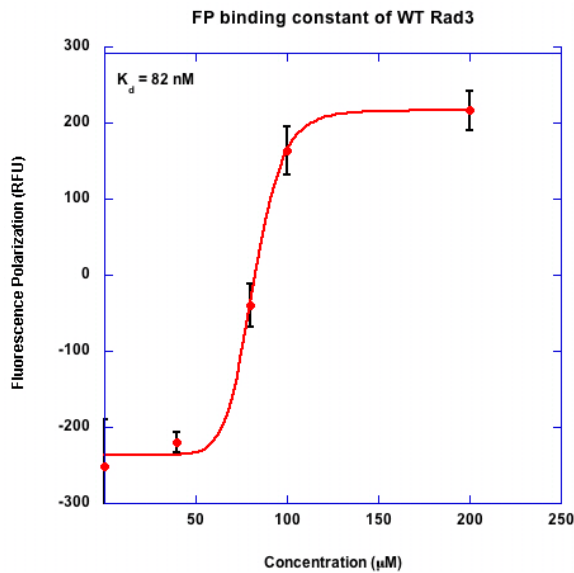


Figure 4.20. Representative FP binding data for Rad3 to fluorophore DNA. Protein was titrated and quantified over a period of 2 minutes. The FP data was fit to a 4-paramenter hill equation to obtain a binding constant to ssDNA.

<i>S. cerevisiae</i> Rad3				<i>S. acidocaldarius</i> XPD(19)			
Mutation	ATPase activity [mol/sec]	Helicase activity [% unwound]	ssDNA Kd [nM]	Mutation	ATPase activity [mol/sec]	Helicase activity [bp/min]	ssDNA Kd [nM]
WT	0.039 (100%)	102 ± 1.5	80 ± 7	WT	1.24 ± 0.03	20.5 ± 0.7	66 ± 55
G47R	0.016 (38%)	50.2 ± 0.7 (49%)	109 ± 27	G34R	0 ± 0.01 (0%)	0.83 ± 0.1 (4%)	67 ± 10
C665R	N.D.	70.6 ± 0.8 (69%)	125 ± 51	A511R	N.D.	N.D.	62
R618P	0.011 (29%)	50.9 ± 1.33 (50%)	68 ± 13	R460P	0.028 ± 0.0004 (2%)	2.78 ± 0.1 (14%)	79 ± 3
R618W	0.021 (53%)	110 ± 2.3 (108%)	100 ± 10	R460W	0.66 ± 0.03 (53%)	19 ± 4.3 (93%)	67 ± 10
I463V/Δ	0.016 (38%)	92.5 ± 1 (91%)	48 ± 6	L325V	1.24 ± 0.03 (100%)	20.5 ± 0.7 (100%)	69 ± 8

Table 4.3. Relative biochemical activities of ScRad3 and SaXPD. In parentheses is activity relative to WT.

Electrochemical Characterization of Rad3 on DNA-modified electrodes

A major unexplored area of research for [4Fe-4S] cluster-containing proteins is their redox activity when bound to DNA. We interrogated the ability of the Rad3 protein to perform DNA-mediated redox chemistry. Using a DNA-modified electrode (Figure 4.22), known concentrations of Rad3 based on 410 nm absorbance were incubated and currents were measured. *S. cerevisiae* Rad3 exhibits a reversible redox-active signal with a midpoint potential of 90 mV vs. NHE, consistent with previously-studied DNA repair proteins. As the protein was incubated on the surface, the redox signal increased linearly with time, suggesting that this process is slow and likely diffusion-limited. The signal is, in fact, diffusion limited, as evidenced by the linear relationship between the midpoint redox potential and the square root of scan rate, consistent with the previously studied proteins in our lab. This signal is reversible, with a ratio of ipc/ipa = 1 for scan rates of 10-200 mV/sec (Figure 4.21). Together, these data indicate that the redox signal observed from Rad3 on a DNA-modified electrode is DNA-mediated and identical to the previously studied BER and NER proteins.

To assay the CT proficiency of the Rad3 mutants, each mutant was incubated on a DNA-modified electrode for 90 minutes. CVs were taken every 3 minutes, and currents were measured from the reductive sweep. As shown in Figure 25, all of the proteins have a redox proficiency similar to that of the WT protein, at approximately ~90 mV versus NHE. The G47R mutant, which is helicase and ATPase deficient, has a relative current intensity (1.26 ± 0.07) similar to that of the WT protein, suggesting that its role in disease is a direct result of its inability to perform basic biochemical functions. Our other mutants, C665R, R618P, and R618W, have redox signals that are 0.82 ± 0.04 , 0.86 ± 0.06 , and 0.76 ± 0.07 respectively, which are comparable to that of the WT protein.

These signals are much smaller than previously reported proteins, likely due to the impurities associated with protein purification. In particular, the formation of aggregates as well as other binding partners could be the cause of this problem and should be further optimized.

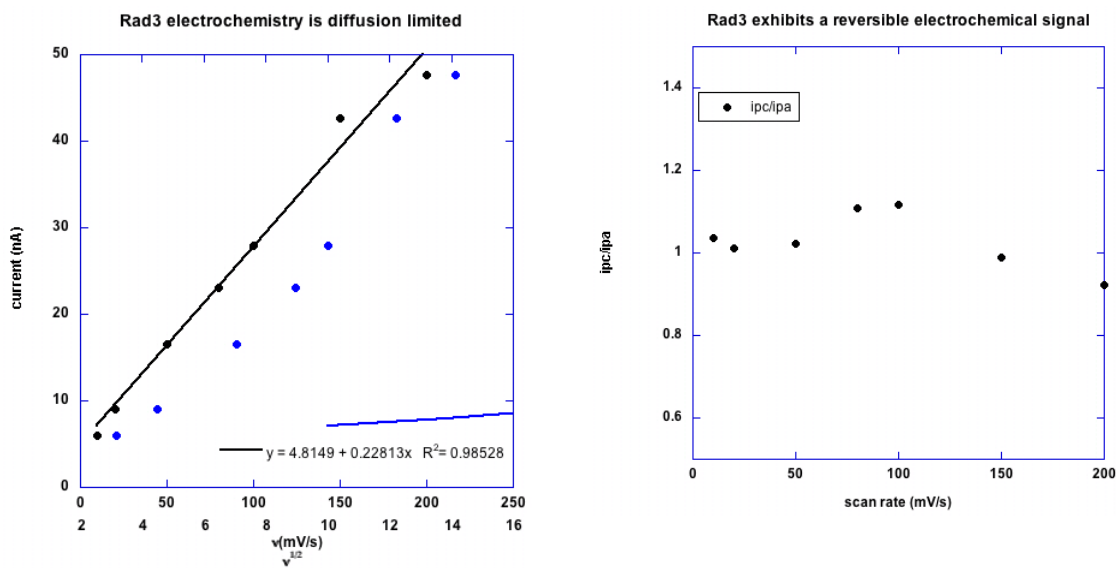


Figure 4.21. Electrochemistry of Rad3 protein on a 5' ssDNA overhang DNA-modified electrode. (Left) plot of current versus scan rate and square root of scan rate. The linear relationship suggests that this process is diffusion limited, consistent with previous reports for [4Fe-4S] cluster-containing proteins. (Right) Plot of ipc/ipa, showing that this reaction is fully reversible over the scan rates presented.

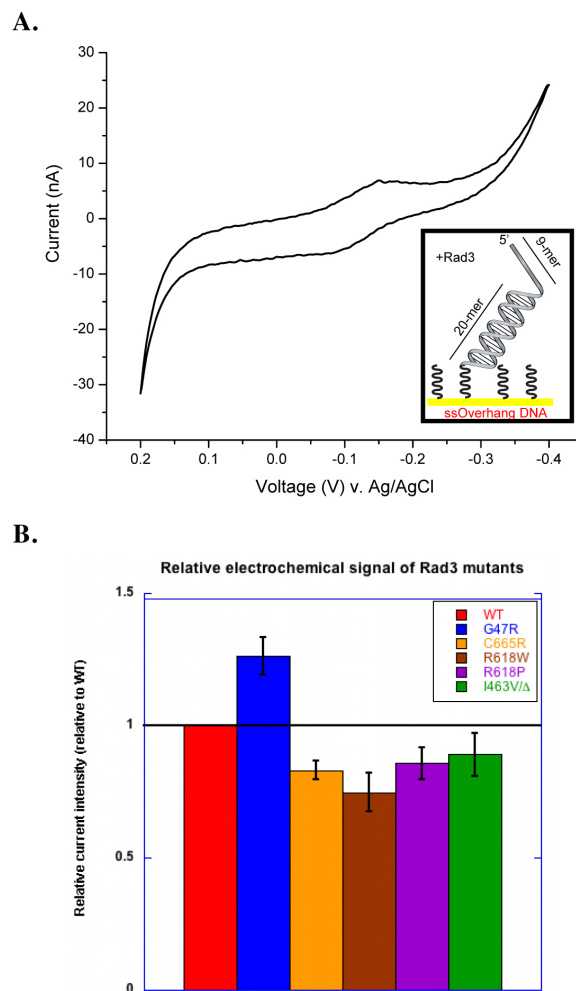


Figure 4.22. Electrochemistry of Rad3 proteins. A. Background corrected CV of WT Rad3 protein. B. Relative current intensity for protein mutants compared to WT Rad3.

Discussion

The XPD family of helicases is essential for nucleotide excision repair (NER). These proteins are well conserved between species, and mutations found in *S. acidocaldarius* XPD are also found in human XPD. Many mutations that lead to XP-related diseases are found in the thermophilic SaXPD, which is a difficult organism to work with and not an ideal model for human XPD. Conversely, the model organism *S. cerevisiae* has been extensively studied, and a host of biomolecular tools exist for genetic manipulation. Rad3 is the yeast homologue of SaXPD and HsXPD, and most of our understanding of the protein is from cellular extracts and early studies of the protein. Besides being a more direct homologue, *S. cerevisiae* cells more closely mimic human cells and provide an excellent model for direct comparisons. Obtaining this protein enables the determination of the effect these disease-related mutations have biochemically, which explains their role in disease.

Rad3 was expressed and purified in *E. coli* and found to contain a redox active [4Fe-4S] cluster. No overexpression was observed, however purification of the MBP-tagged Rad3 was achieved through a combination of four columns to yield 2 mg/mL protein. XPD-conserved Rad3 protein mutants were generated. These G47R, I463V/Δ, R618P, R618W and C665R mutations all contain [4Fe-4S] clusters, as monitored by UV-visible spectroscopy. DNA binding constants show that the protein binds ssDNA in the range of 40 – 125 nM, consistent with the previously-purified SaXPD protein. Initial ATPase and helicase activities follow similar trends to previously reported SaXPD activities, but must be confirmed, as protein stability in the storage buffer appears to be questionable.

Saccharomyces cerevisiae more closely resembles human cell lines than the archaeal *S. acidocaldarius*; we have developed a Rad3 knockout strain that allows for easy manipulation of the copy of Rad3 by taking advantage of a plasmid shuffle. Both an NQO- and UV-survival assay were developed to measure how NER damage affects Rad3 mutant strain growth. In both cases, the mutant Rad3 strains survived less than the WT Rad3 strain, but to varying degrees. We observed the helicase and ATPase deficient (based on SaXPD biochemistry) G47R, C665R and R618P mutants' inability to survive when challenged with both NQO and UV-light, presumably due to their inability to repair the damaged DNA. For each of these survival assays, we only saw major differences between the strains when using high dosages of DNA damage (200 J/m² and 200 ng/mL NQO). Perhaps by overwhelming the cell, deficiencies in each of the Rad3 mutants were accentuated.

The R618W disease-related mutant, which has helicase activity, exhibited only a mild sensitivity to these DNA damaging agents, suggesting that helicase activity is essential for survival. Over time, R618W showed repair on the order of WT strain, evidenced by a shift in $t_{1/2}$ of only 2 hours when challenged with 20 ng/mL NQO. However, the R618P mutant strain showed an erratic shift of nearly 45 hours, demonstrating that the R618P protein is not only slower to repair but also inviable over the time-course of the survival assay. Mutations were made at this position and found to survive in the order of proline < glutamate < alanine < tryptophan < tyrosine ≈ leucine ≈ arginine (WT) in an NQO-survival assay. Substitution with aromatic residues such as tryptophan and tyrosine yield mutants that maintain survival, while substitution with destabilizing residues such as proline and glutamate yield inviable strains. Mutations at

this position are found in a variety of patients, including a R618Q mutation found in a recently diagnosed patient (36). This residue may play an important role in defining the disease state.

Previous reports involving the organism *S. pombe* suggest that the I463V/Δ mutation in Rad15, the equivalent of XPD, is lethal (22). This mutation is also found in human patients. However, in our model system, we observed viability closely mimicking the WT strain, suggesting that not all mutations are conserved between the model organisms. This mutant preliminarily is both helicase and ATPase proficient and is not a causative mutation in the human disease. While this mutant has been identified in XP-patients, it likely only leads to the disease when coupled with additional mutations.

Using Rad3 mutant strains, we observed how mutations in this protein affect growth rates and survival *in vivo* when the *S. cerevisiae* strains are challenged with a variety of DNA damage agents not traditionally associated with NER. The ATPase/helicase deficient G47R mutation shows a much slower growth rate in the presence of MMS and CPT, while no such change occurs with the WT strain, suggesting a role in DNA repair for Rad3 beyond that of the traditional NER substrates. The role of the Rad3 helicase likely extends beyond to stalled DNA replication forks as well with methylated DNA. Both of these substrates are important for cellular survival, suggesting a significant role for Rad3 in DNA repair.

Finally, in an attempt to observe how mutations in Rad3 regulate DNA repair genes, qPCR was performed to monitor 12 unique genes. When challenged with 200 ng/mL NQO, no strain-specific up-regulation of the polymerases, NER nucleases, MMS19 orthologues, or FeS cluster machinery loading proteins is observed. However,

Rfc1 and Pol1 are up-regulated in most strains, suggesting an important role for re-starting DNA synthesis. This appears to be a general trend and not specific to mutations in Rad3.

Obtaining pure ScRad3 further allowed us to monitor the DNA-mediated redox chemistry of the [4Fe-4S] cluster. When using a DNA-modified electrode with a 5' ssDNA overhang, we observed a reversible midpoint redox potential of ~85 mV versus NHE for each of the protein mutants. None of these proteins showed a shift in their redox potential; mutants were also incubated on these electrodes and, when normalized for cluster content, exhibited redox signals comparable to one another. This redox signaling is extremely useful for signaling between DNA repair proteins, and could potentially be a mechanism through which Rad3 communicates with other DNA repair proteins.

We have described the rapid purification and characterization of the *Saccharomyces cerevisiae* Rad3 protein from *E. coli*. Rad3, the XPD homologue of *S. cerevisiae*, is responsible for repairing bulky DNA adducts through the NER pathway. The G47R, R618P, and C665R mutations that are responsible for disease in humans are confirmed to be inviable in our yeast strains when challenged with the DNA damaging agent NQO. We have also studied the mutant R618W, which leads to a helicase active but ATPase deficient Rad3 that is still viable, albeit with a 10-fold decrease in viability when challenged with 200 ng/mL NQO. The I463V/Δ mutation, which leads to disease in humans and inviability in the yeast organism *S. pombe*, is viable in our assays and exhibits survival comparable to the WT Rad3 strain. We explored the effect of mutations at R618, which suggest that strongly destabilizing mutations lead to inviability, while

aromatic changes are viable in the presence of DNA damage. We also observed the DNA-bound redox potential of each of the protein mutants, something that is unique to [4Fe-4S] cluster-containing proteins. Each of the proteins exhibits a similar DNA-bound potential. Obtaining purified Rad3 enabled quick and efficient characterization of mutants that are believed to be involved in XP-related disease and allows for a strict characterization of the protein. Future work will involve determining optimal protein storage conditions, characterizing the protein, and understanding the electrochemistry in ScRad3. However, our *in vivo* system enables easy manipulation of Rad3 in a haploid *S. cerevisiae* strain to better understand how Rad3 mutations affect survival and growth rates. We observed that mutants of Rad3 are sensitive to MMS and CPT, two DNA damaging agents not previously thought of in NER. Finally, redox signaling by Rad3 may serve as a unique tool for DNA repair proteins to communicate with each other, as do other proteins implicated in DNA repair, such as the polymerases, primase, and FancJ, which have been shown to contain [4Fe-4S] clusters (37-42).

References

1. Hoeijmakers, J. H. (2009) DNA damage, aging, and cancer, *N Engl J Med* 361, 1475-1485.
2. Hoeijmakers, J. H. (2001) Genome maintenance mechanisms for preventing cancer, *Nature* 411, 366-374.
3. Prakash, S., and Prakash, L. (2000) Nucleotide excision repair in yeast, *Mutat Res* 451, 13-24.
4. David, S. S., O'Shea, V. L., and Kundu, S. (2007) Base-excision repair of oxidative DNA damage, *Nature* 447, 941-950.
5. Cleaver, J. E., Lam, E. T., and Revet, I. (2009) Disorders of nucleotide excision repair: the genetic and molecular basis of heterogeneity, *Nat Rev Genet* 10, 756-768.
6. Kunkel, T. A., and Erie, D. A. (2005) DNA mismatch repair, *Annu Rev Biochem* 74, 681-710.
7. de Boer, J., Andressoo, J. O., de Wit, J., Huijmans, J., Beems, R. B., van Steeg, H., Weeda, G., van der Horst, G. T., van Leeuwen, W., Themmen, A. P., Meradji, M., and Hoeijmakers, J. H. (2002) Premature aging in mice deficient in DNA repair and transcription, *Science* 296, 1276-1279.
8. Guzder, S. N., Qiu, H., Sommers, C. H., Sung, P., Prakash, L., and Prakash, S. (1994) DNA repair gene RAD3 of *S. cerevisiae* is essential for transcription by RNA polymerase II, *Nature* 367, 91-94.
9. Harosh, I., Naumovski, L., and Friedberg, E. C. (1989) Purification and characterization of Rad3 ATPase/DNA helicase from *Saccharomyces cerevisiae*, *J Biol Chem* 264, 20532-20539.

10. Sung, P., Prakash, L., Weber, S., and Prakash, S. (1987) The RAD3 gene of *Saccharomyces cerevisiae* encodes a DNA-dependent ATPase, *Proc Natl Acad Sci U S A* 84, 6045-6049.
11. Sung, P., Prakash, L., Matson, S. W., and Prakash, S. (1987) RAD3 protein of *Saccharomyces cerevisiae* is a DNA helicase, *Proc Natl Acad Sci U S A* 84, 8951-8955.
12. Higgins, D. R., Prakash, S., Reynolds, P., Polakowska, R., Weber, S., and Prakash, L. (1983) Isolation and characterization of the RAD3 gene of *Saccharomyces cerevisiae* and inviability of rad3 deletion mutants, *Proc Natl Acad Sci U S A* 80, 5680-5684.
13. Egly, J. M., and Coin, F. (2011) A history of TFIIH: two decades of molecular biology on a pivotal transcription/repair factor, *DNA Repair (Amst)* 10, 714-721.
14. Lehmann, A. R. (2001) The xeroderma pigmentosum group D (XPD) gene: one gene, two functions, three diseases, *Genes Dev* 15, 15-23.
15. Suhasini, A. N., and Brosh, R. M., Jr. (2013) DNA helicases associated with genetic instability, cancer, and aging, *Adv Exp Med Biol* 767, 123-144.
16. Brosh, R. M., Jr. (2013) DNA helicases involved in DNA repair and their roles in cancer, *Nat Rev Cancer* 13, 542-558.
17. Wolski, S. C., Kuper, J., Hanzelmann, P., Truglio, J. J., Croteau, D. L., Van Houten, B., and Kisker, C. (2008) Crystal structure of the FeS cluster-containing nucleotide excision repair helicase XPD, *PLoS Biol* 6, e149.

18. Liu, H., Rudolf, J., Johnson, K. A., McMahon, S. A., Oke, M., Carter, L., McRobbie, A. M., Brown, S. E., Naismith, J. H., and White, M. F. (2008) Structure of the DNA repair helicase XPD, *Cell* 133, 801-812.
19. Fan, L., Fuss, J. O., Cheng, Q. J., Arvai, A. S., Hammel, M., Roberts, V. A., Cooper, P. K., and Tainer, J. A. (2008) XPD helicase structures and activities: insights into the cancer and aging phenotypes from XPD mutations, *Cell* 133, 789-800.
20. Mui, T. P., Fuss, J. O., Ishida, J. P., Tainer, J. A., and Barton, J. K. (2011) ATP-stimulated, DNA-mediated redox signaling by XPD, a DNA repair and transcription helicase, *J Am Chem Soc* 133, 16378-16381.
21. Dubaele, S., Proietti De Santis, L., Bienstock, R. J., Keriel, A., Stefanini, M., Van Houten, B., and Egly, J. M. (2003) Basal transcription defect discriminates between xeroderma pigmentosum and trichothiodystrophy in XPD patients, *Mol Cell* 11, 1635-1646.
22. Taylor, E. M., Broughton, B. C., Botta, E., Stefanini, M., Sarasin, A., Jaspers, N. G., Fawcett, H., Harcourt, S. A., Arlett, C. F., and Lehmann, A. R. (1997) Xeroderma pigmentosum and trichothiodystrophy are associated with different mutations in the XPD (ERCC2) repair/transcription gene, *Proc Natl Acad Sci U S A* 94, 8658-8663.
23. Boal, A. K., Yavin, E., Lukianova, O. A., O'Shea, V. L., David, S. S., and Barton, J. K. (2005) DNA-bound redox activity of DNA repair glycosylases containing [4Fe-4S] clusters, *Biochemistry* 44, 8397-8407.

24. Lee, P. E., Demple, B., and Barton, J. K. (2009) DNA-mediated redox signaling for transcriptional activation of SoxR, *Proc Natl Acad Sci U S A* **106**, 13164-13168.
25. Kelley, S. O., and Barton, J. K. (1999) Electron transfer between bases in double helical DNA, *Science* **283**, 375-381.
26. Boal, A. K., Genereux, J. C., Sontz, P. A., Gralnick, J. A., Newman, D. K., and Barton, J. K. (2009) Redox signaling between DNA repair proteins for efficient lesion detection, *Proc Natl Acad Sci U S A* **106**, 15237-15242.
27. Romano, C. A., Sontz, P. A., and Barton, J. K. (2011) Mutants of the base excision repair glycosylase, endonuclease III: DNA charge transport as a first step in lesion detection, *Biochemistry* **50**, 6133-6145.
28. Yavin, E., Boal, A. K., Stemp, E. D., Boon, E. M., Livingston, A. L., O'Shea, V. L., David, S. S., and Barton, J. K. (2005) Protein-DNA charge transport: redox activation of a DNA repair protein by guanine radical, *Proc Natl Acad Sci U S A* **102**, 3546-3551.
29. Merino, E. J., and Barton, J. K. (2008) DNA oxidation by charge transport in mitochondria, *Biochemistry* **47**, 1511-1517.
30. Pugh, R. A., Honda, M., Leesley, H., Thomas, A., Lin, Y., Nilges, M. J., Cann, I. K., and Spies, M. (2008) The iron-containing domain is essential in Rad3 helicases for coupling of ATP hydrolysis to DNA translocation and for targeting the helicase to the single-stranded DNA-double-stranded DNA junction, *J Biol Chem* **283**, 1732-1743.

31. Seong, K. M., Lee, S. H., Kim, H. D., Lee, C. H., Youn, H., Youn, B., and Kim, J. (2011) Expression, purification, and characterization of putative *Candida albicans* Rad3, the product of orf19.7119, *Biochemistry (Mosc)* 76, 666-676.
32. Goffeau, A., Barrell, B. G., Bussey, H., Davis, R. W., Dujon, B., Feldmann, H., Galibert, F., Hoheisel, J. D., Jacq, C., Johnston, M., Louis, E. J., Mewes, H. W., Murakami, Y., Philippsen, P., Tettelin, H., and Oliver, S. G. (1996) Life with 6000 genes, *Science* 274, 546, 563-547.
33. Budd, M. E., and Campbell, J. L. (1995) DNA polymerases required for repair of UV-induced damage in *Saccharomyces cerevisiae*, *Mol Cell Biol* 15, 2173-2179.
34. Graham, J. M., Jr., Anyane-Yeboa, K., Raams, A., Appeldoorn, E., Kleijer, W. J., Garritsen, V. H., Busch, D., Edersheim, T. G., and Jaspers, N. G. (2001) Cerebro-oculo-facio-skeletal syndrome with a nucleotide excision-repair defect and a mutated XPD gene, with prenatal diagnosis in a triplet pregnancy, *Am J Hum Genet* 69, 291-300.
35. Helleday, T., Petermann, E., Lundin, C., Hodgson, B., and Sharma, R. A. (2008) DNA repair pathways as targets for cancer therapy, *Nat Rev Cancer* 8, 193-204.
36. Falik-Zaccai, T. C., Erel-Segal, R., Horev, L., Bitterman-Deutsch, O., Koka, S., Chaim, S., Keren, Z., Kalfon, L., Gross, B., Segal, Z., Orgal, S., Shoval, Y., Slor, H., Spivak, G., and Hanawalt, P. C. (2012) A novel XPD mutation in a compound heterozygote; the mutation in the second allele is present in three homozygous patients with mild sun sensitivity, *Environ Mol Mutagen* 53, 505-514.

37. Zhang, J., Kasciukovic, T., and White, M. F. (2012) The CRISPR associated protein Cas4 Is a 5' to 3' DNA exonuclease with an iron-sulfur cluster, *PLoS One* 7, e47232.
38. Pokharel, S., and Campbell, J. L. (2012) Cross talk between the nuclease and helicase activities of Dna2: role of an essential iron-sulfur cluster domain, *Nucleic Acids Res* 40, 7821-7830.
39. White, M. F., and Dillingham, M. S. (2012) Iron-sulphur clusters in nucleic acid processing enzymes, *Curr Opin Struct Biol* 22, 94-100.
40. Weiner, B. E., Huang, H., Dattilo, B. M., Nilges, M. J., Fanning, E., and Chazin, W. J. (2007) An iron-sulfur cluster in the C-terminal domain of the p58 subunit of human DNA primase, *J Biol Chem* 282, 33444-33451.
41. Netz, D. J., Stith, C. M., Stumpfig, M., Kopf, G., Vogel, D., Genau, H. M., Stodola, J. L., Lill, R., Burgers, P. M., and Pierik, A. J. (2012) Eukaryotic DNA polymerases require an iron-sulfur cluster for the formation of active complexes, *Nat Chem Biol* 8, 125-132.
42. Vaithiyalingam, S., Warren, E. M., Eichman, B. F., and Chazin, W. J. (2010) Insights into eukaryotic DNA priming from the structure and functional interactions of the 4Fe-4S cluster domain of human DNA primase, *Proc Natl Acad Sci U S A* 107, 13684-13689.

Chapter 5

DNA Charge Transport as a First Step in Coordinating the Detection of Lesions by
Repair Proteins

Adapted from Sontz, P.A., Mui, T.P., Fuss, J.O., Tainer, J.A., and Barton, J.K. "DNA Charge Transport as a First Step in Coordinating the Detection of Lesions by Repair Proteins" Proc. Natl. Acad. Sci. USA **2012** 109, 6, 1856-1861

P.A.S performed AFM experiments. T.P.M. performed electrochemistry. J.O.F. purified SaXPD protein.

Introduction

Proteins involved in cellular repair pathways are charged with finding and correcting genomic lesions arising from a variety of sources including oxidative stress, UV radiation, and environmental mutagens (1). Specific repair proteins are allocated to target different types of DNA damage for a concerted attack. For example, the nucleotide excision repair (NER) pathway includes proteins that repair lesions that largely distort the helical structure of DNA in a variety of ways; dipyrimidine adducts and cis-platin crosslinks are two structurally distinct examples. In contrast, different base excision repair (BER) glycosylases remove specific base lesions; in *Escherichia coli*, for example, Endonuclease III (EndoIII) targets oxidized pyrimidines, while MutY repairs oxo-guanine-adanine mismatches (1-4).

As DNA facilitates charge transport (CT) over long molecular distances (5,6), and this charge transport chemistry is sensitive to a variety of lesions that perturb DNA base stacking (7, 8), our laboratory has proposed that repair proteins exploit this unique property of DNA to search for damage (9-11). Several DNA repair proteins contain redox-active [4Fe-4S] clusters that are not required for folding (12, 13), and examples of these proteins from the BER pathway, EndoIII and MutY, are activated toward oxidation as they bind DNA (14-16). While EndoIII effectively removes oxidized pyrimidines, the repair protein is found in very low copy number in *E. coli* (~500 copies per cell) (17, 18). Surprisingly, MutY, which removes adenine from 8-oxo-G:A mismatches, is found in even lower copy number, only ~30 copies per cell (19), which, along with the low selectivity of these proteins for their substrates relative to unmodified DNA, begs the question of how they can so effectively find and repair their target lesions in the genome.

Importantly, mutations in the human MutY homolog (hMYH) directly correlate to the development of colorectal cancer (20, 21).

We have recently examined whether DNA CT may play some role in how these BER proteins find their site (22, 23). Using DNA electrochemistry and AFM experiments, we have found that the ability of EndoIII mutants to localize in the vicinity of a base mismatch correlates with their ability to carry out DNA CT. Moreover, using a genetics assay, we found that EndoIII cooperates with MutY *in vivo* in finding MutY lesions, but that a CT-deficient mutant of EndoIII cannot similarly aid MutY (22).

Interestingly, more proteins involved in genome maintenance are being found to contain [4Fe-4S] clusters, many with no clear structural or enzymatic role for the clusters. One such protein is XPD, which is part of the transcription factor IIH (TFIIH) machinery and is involved in nucleotide excision repair (NER) (24, 25). Here we consider if XPD, which is not involved in BER, similarly utilizes DNA CT to localize in the vicinity of lesions, and whether signaling between different DNA-binding proteins can occur to coordinate the search for damage (26, 27).

XPD, an ATP-dependent 5'-3' helicase from the NER pathway, is a major component of TFIIH, the transcriptional and repair machinery that unwinds damaged DNA for lesion repair in NER (28, 29). Mutations in the human *XPD* helicase gene (ERCC2) lead to the genetic disorders trichothiodystrophy (TTD), Cockayne syndrome (CS), and xeroderma pigmentosum (XP) (28-31). There is now evidence that mutations specifically in the iron-sulfur cluster domain of XPD result in TFIIH instability, leading to TTD (28, 30). Similarly, mutations in the analogous region of the related *FancJ* gene (which also encodes a helicase with an iron-sulfur cluster) causes predisposition to early-

onset breast cancer (25, 32). We have demonstrated that the [4Fe-4S] cluster in *Sulfolobus acidocaldarius* (Sa)XPD is redox-active, with a redox potential equivalent to that of BER proteins EndoIII and MutY (~80 mV vs. NHE) (33). Moreover, as we describe here, a mutant of SaXPD, L325V (L461 in human XPD) is unable to mediate DNA CT electrochemically. Importantly, L325V aligns with mutated residues in human XPD and *Schizosaccharomyces pombe* Rad15 that lead to TTD, XP, and XP/CS (25, 31, 34).

Here we explore by AFM whether XPD can participate in DNA-mediated signaling to localize in the vicinity of a DNA mismatch. Similar to base lesions, a single base mismatch inhibits DNA CT but, importantly, is not a substrate for repair by XPD (35). In our model for a search facilitated by DNA CT (Figure 5.1), the search for DNA damage is initiated under oxidative stress by the one-electron oxidation of a DNA-bound protein by a guanine radical, taking the cluster from a 2+ oxidation state to a 3+ oxidation state. But it is DNA CT between two repair proteins that leads to the redistribution in the vicinity of a lesion. With a DNA-bound potential shifted negative as compared to free protein (14), the proteins are expected to have a lower affinity for DNA in their reduced form. Thus, DNA-mediated reduction of one protein by the other leads to the dissociation of the reduced protein from DNA, effectively giving overall dissociation of repair proteins away from a region of the genome without lesions. Our model relies on the sensitivity of CT to proper π -stacking of the bases between the donor protein and the distant acceptor protein (22, 23); if, instead, there is an intervening lesion, DNA-mediated CT does not occur, and the repair protein remains bound and can processively move to the lesion and carry out enzymatic repair. In this process, the repair proteins eventually

relocalize in the vicinity of lesions or any modification that inhibits DNA CT. As a result the overall search regime for the repair proteins is made smaller than the full genome: they preferentially localize where needed for repair.

Despite various studies of EndoIII and MutY independently, it still remains to be established whether these proteins from different repair pathways (NER and BER) cooperate with one another in a coordinated search. Since a C:A mismatch, for example, does not distort the DNA helix, it would be expected to evade the biological NER pathway. Alternatively, if enzymes rely on DNA/protein CT as a first step in finding damage, then any protein that can carry out DNA CT can participate in the search, integrating repair pathways that were previously thought to be separate. To examine this coordinated search, AFM is used to visualize mixtures containing two types of proteins: i) those that are able to carry out DNA CT and ii) those that are defective at DNA CT. AFM, a technique that allows for visualization of single-molecule protein/DNA interactions, can be used to observe proteins bound to long strands (3.8 kbp) of DNA containing a site-specific mismatch (C:A) (23, 36-39). Binding density ratios calculated from counting strands and proteins in AFM images can then give us clues to the first step in lesion detection. Here, not only do we examine whether proteins from the NER pathway redistribute in the vicinity of lesions as a function of their ability to perform DNA CT, but also whether they can cooperate with other repair proteins in the DNA-mediated search for damage.

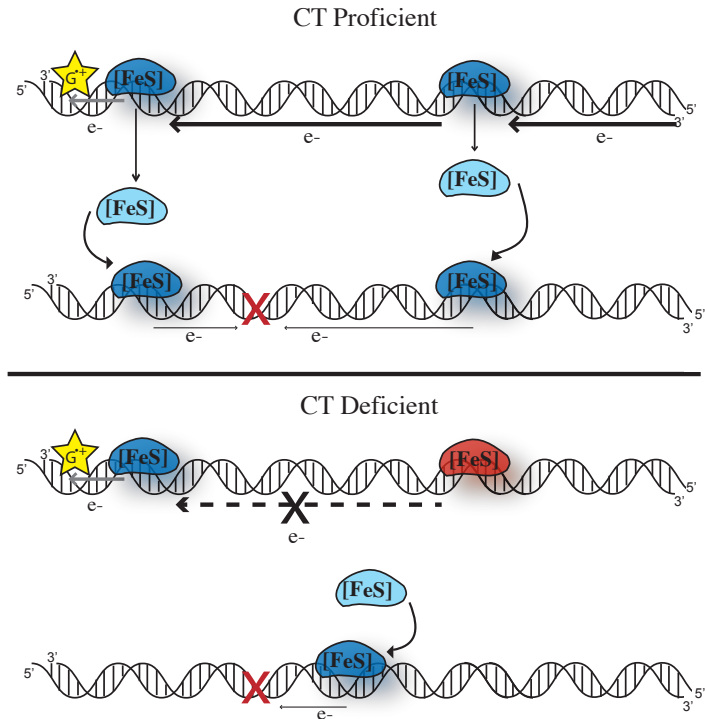


Figure 5.1. Model for damage detection and redistribution by repair proteins. (Top) Given two repair proteins of similar potential containing [4Fe-4S] clusters, which can carry out DNA CT, (XPD or EndoIII (blue)), CT can proceed through well-matched unmodified DNA. Stimulated through protein oxidation by guanine radicals (yellow) formed under oxidative stress, DNA CT occurs between DNA-bound proteins, promoting the dissociation of reduced protein (light blue). DNA CT does not occur, however, in the presence of an intervening mismatch or lesion (red X); repair proteins are not reduced, do not dissociate, and instead remain bound in the vicinity of the lesion. (Bottom) If repair proteins are mutants such as XPD L325V or EndoIII Y82A (red) and are unable to perform DNA CT (dashed line), they cannot send or receive signals to locate damage. In the presence of a lesion, these proteins then do not preferentially redistribute in the vicinity of the mismatch.

MATERIALS AND METHODS

All chemicals were purchased from Sigma Aldrich. All enzymes were purchased from New England Biolabs unless otherwise specified. Mica surfaces were purchased from SPI supplies. Silicon AFM probes were purchased from Budget Sensors. Oligonucleotides were purchased from IDT or synthesized on a 3400 DNA synthesizer (Applied Biosystems).

Mismatched (C:A) Strand Synthesis

Four primers with the following sequences were synthesized using standard phosphoramidite chemistry:

- 1) 5'-GTACAGAGTTCAGTCGGCATCCGCTTACAGACAAGC-3' (forward),
- 2) 5'-CCGGTAACTATCGTCTTGAGTCC-3' (reverse),
- 3) 5'-GACTGAACTCTGTACCTGGCACGACAGGTTCCCG-3' (forward),
- 4) 5'-GACTGAACTCTATACTGGCACGACAGGTTCCCG-3' (forward)

The underlined bases highlight the location of a 2'-O-methyl residue (Glen Research). Primers were phosphorylated using 5 U PNK, 10% PNK buffer, 0.5 mM ATP for 5 hours at 37 °C. Primers were purified using phenol-chloroform extraction followed by ethanol precipitation (54). After being dried in vacuo, primers were redissolved in 20 µL water and used in separate PCR reactions (41) using pUC19 as a template to generate two duplexes 1610 bp and 2157 bp (matched), each containing one 14-nucleotide single-strand overhang. Each 100 µL PCR reaction contained 50 pmol of each of two primers, 1X *Taq* buffer (100 mM Tris-HCl, 15 mM MgCl₂, 500 mM KCl, pH 8.3), 0.2 mM each dNTP, 1 ng plasmid template pUC19 and 3 U *Taq* polymerase (Roche). A typical step program for PCR was as follows: After incubation at 94°C for 10 minutes, 34 cycles

were performed as follows: 94°C for 1 minute, (52°C for primers 1+2, 54°C for primers 2+3 or 2+4), for 1 minute, and 72°C for 3 minutes. The PCR product was then suspended in 50 mM NaCl/ 5mM phosphate buffer and quantitated. Separate duplexes were annealed at 65 °C for 8 minutes in 10 mM Tris buffer, then cooled to 20 °C during 2 hours. A total of 15 units of T4 DNA ligase and 10% T4 ligase buffer were added (total reaction volume ~20 µL) and incubated overnight at 16 °C, followed by deactivation for 10 minutes at 65 °C to yield the 3767 bp (mismatched) long strand. We did not bring the ligation reaction to completion, so as to obtain a mixture of DNA samples that were equivalent other than the presence of the mismatch at the ligation site. The DNA duplexes (ligated and unligated) were then analyzed by 0.6% agarose gel electrophoresis. Single DNA strands complementary to short duplex overhangs were ordered from IDT: 5'-GACTGAACCTGTAC-3' Tm=41.6 ° C (1.6 kbp duplex overhang), 5'- GTACAGAGTTCAAGTC-3' Tm=41.6 ° C (2.2 kbp matched duplex overhang), and 5'- GTATAGAGTTCAAGTC-3' Tm=37.5 ° C (2.2 kbp mismatched duplex overhang). Single-strand DNA was purified using reversed-phased HPLC and verified with MALDI-TOF mass spectrometry.

Protein Purification and Expression

EndoIII and Y82A EndoIII were expressed from the pNTH10 expression vector and purified as described previously (22). EndoIII and Y82A were stored in 20 mM sodium phosphate pH 7.5, 100 mM NaCl, 20% glycerol, and 0.5 mM EDTA buffer. Protein concentrations were determined using the UV-visible absorbance of the [4Fe4S] cluster (410 nm, e = 17,000) (55). XPD was made according procedures described in reference 33.

AFM Experiments

AFM experiments were performed using the protocol similar to that reported previously (23). Stock DNA solution contained 50 –200 ng of total DNA (~6 μ M) composed of the mixture of ligated 3.8-kbp duplexes and the two unligated duplexes (1.6 and 2.2 kb) in 6 mM MgCl₂/Tris-EDTA buffer. The 1.6 kb overhang complement (60 μ M) was added to the DNA solution to block the 14 bp single-strand overhangs generated by PCR. This was then incubated overnight at 4 °C. XPD protein was dialyzed against the protein buffer (20 mM phosphate, 100 mM NaCl, 1 mM EDTA, 5% glycerol, pH 7.5 and filtered prior to use) to remove residual DTT. The concentration of individual proteins was determined by UV/visible spectrophotometry (Beckman DU 7400) using $\epsilon=17,000\text{ M}^{-1}$ at 410 nM for the [4Fe-4S] cluster. After addition of excess 2.2 kb duplex complement (60 μ M), XPD (0.6 μ M) was added to the stock DNA solution, this protein/DNA solution was incubated at 4 °C overnight. A sample was then deposited (5-10 μ L) onto a freshly cleaved mica surface for 1-2 min, rinsed with 2 mL of water, and dried under argon. Mutant XPD protein (L325V) was added to a stock solution of 50 ng DNA for a final protein concentration of 0.6 μ M. Deposition conditions were identical to that for WT XPD- DNA samples after incubation at 4 °C overnight.

For mixed protein experiments (WT^{XPD}/WT^{EndoIII}, WT^{XPD}/Y82A^{EndoIII}, WT^{EndoIII}/L325V^{XPD}, and WT^{XPD}/L325V^{XPD}), XPD, EndoIII, L325V, or Y82A was added to the prepared DNA solution described previously at equimolar (1:1) concentrations (0.3 μ M each) prior to incubation at 4 °C overnight. Protein/DNA complexes were formed with DNA solution containing ~200 ng of the mixture of PCR products and overhang complements (~6 μ M DNA) in 6 mM MgCl₂/Tris-EDTA buffer at 4°C overnight. The

reaction mixture was then deposited (5-10 μ L) on the mica surface for 1-2 minutes, rinsed with 2 mL water, and dried under argon.

AFM Instrumentation

Silicon AFM Probes purchased from Budget Sensors, with a spring constant of 3 N/m and a resonance frequency of 75 kHz, were used in a Digital Instruments Multimode SPM. Images were captured in air with scan areas of 2x2 μ m² or 3x3 μ m² in tapping mode, at an amplitude of 0.54-2.00 V and at a scan rate of 3.05 Hz. Scan rates of 3.05 Hz were used in order to obtain images of higher quality.

Binding Density Ratio Calculations

WSxM software was used to measure general DNA contour lengths and height profiles of the proteins as described previously (23, 56). For each data set, images from at least three independent samples were analyzed, compared, and pooled (>200 long or short strands). Distinguishable strands and protein positions were counted by hand. The binding density ratio, r, is defined as the ratio of the proteins bound on long strands divided by proteins bound on short strands. The ratio is normalized for length by dividing by 1.9 kbp, which is the average length of the short strands. Binding affinities were found by determining the number of proteins bound per kilobasepair strand. The uncertainty was determined through the total number of proteins observed.

Protein Electrochemistry

Protein electrochemistry was performed as previously described (33). Briefly, individual proteins samples were dialyzed to remove residual DTT and quantified based on 410 nm absorbance. Protein was then added to a DNA modified electrode containing a 9 nucleotide 5' single-strand overhang. Cyclic Voltammograms were then obtained using

Ag/AgCl reference electrodes and a Pt auxiliary electrode at 50 mV/s scan rate on a CH Instruments 620C electrochemical analyzer.

RESULTS

Experimental strategy using AFM to probe protein distribution

With BER proteins we have previously demonstrated that the ability of a protein to perform DNA CT directly correlates to its redistribution in the vicinity of base lesions or mismatches that inhibit CT (23). We tested XPD redistribution promoted through DNA CT by preparing DNA strands containing a single C:A mismatch, a modification that we know to inhibit CT (40), alongside DNA strands containing no mismatches. To distinguish the strands in microscopy experiments, we made mismatched strands >1200 base pairs longer than the matched strands. AFM was utilized to gather images of DNA and bound protein that could be analyzed for the propensity of XPD to redistribute. ATP was not incorporated in AFM experiments, as XPD helicase activity should not be required for a DNA-mediated redistribution.

Long (3.8 kilobase) DNA duplexes containing a site-specific C:A mismatch and short (2.2 and 1.6 kilobases) well-matched duplexes of the same total sequence were constructed. To prepare these DNA samples, pUC19 plasmid was amplified with primers incorporating a 2' *O*-methyl residue to yield two short duplexes containing 14-nucleotide single-strand overhangs (23, 41). Upon ligation of these two duplexes, 3.8 kbp strands were formed that contained only one C:A mismatch in the middle of the strand. The ligation reaction was not taken to completion, so as to have a mixture of well-matched short and mismatched long strands for protein distribution studies. Although a C:A mismatch effectively inhibits DNA CT (40), it is not a lesion that is preferentially bound by XPD. However, the 14-nucleotide overhangs generated with PCR are specific substrates for XPD helicase ($K_d \sim 1 \mu\text{M}$) (25, 42). We directly observed this preference in

initial AFM experiments. Protein assignments were verified through analysis of their 3-4 nm heights in the images; without protein, features of this dimension were not observed and larger heights (> 7 nm) indicated salt precipitates or protein aggregation. Only clearly-identifiable long or short strands and bound proteins were counted. XPD protein position was determined based on the distance of the protein from the end of the strand.

We examined distribution with and without blocking the ends of short strands, given that XPD has some preference for single-strand overhangs. Comparing raw protein position (middle versus ends) on long and short strands, XPD exhibited a large preference for the ends (~300 bp range) of short duplexes containing overhangs ($>50\%$ of bound proteins). To block XPD from binding to the 14 bp segment, overhang complements were added to DNA/protein solutions in excess. When the overhangs were blocked, no preferential binding to the short strands was observed (*vide infra*).

Detection of XPD Complexes

AFM images of DNA-bound protein complexes are represented in Figure 5.2. XPD protein bound to matched DNA (Figure 5.2 top) can be easily distinguished based on strand height profile of tapping mode images. Zoomed in images display clearly identifiable long and short strands with protein bound (Figure 5.2 bottom). Images of DNA and protein complexes were acquired with a scan size of $2 \times 2 \mu\text{m}^2$ or $3 \times 3 \mu\text{m}^2$ at a scan rate of 3.05 Hz. As AFM images vary with surface cleavage, sample wetness, deposition time, and volume, >200 long or short strands were counted for at least three independent samples. The uncertainty was based on the total number of proteins counted. Importantly, we measured the relative binding affinity of mutants and wild type (WT) proteins, and, in all of the samples described, the number of proteins bound per base pair

remained constant (Table 5.1). Thus, any changes we saw in distribution are not due to differences in binding affinities of proteins.

To probe the DNA CT properties of a redox-active DNA helicase, XPD and DNA complexes were examined with AFM. XPD shows redistribution onto long mismatched strands with a ratio of protein binding densities, r (long/short) of 1.54 ± 0.08 (Figure 5.3). We observed 0.23 proteins per kilobase of long strand and 0.15 proteins per kilobase of short strand (see Table 5.1 for further details). If we instead examine XPD distribution when long and short strands are fully matched, we see a binding density ratio of 0.94 ± 0.05 . Previously, for EndoIII, we found r for (long/short) was 1.6 ± 0.09 (22). We expect a ratio of 1 if there is an equal distribution of proteins on matched and mismatched strands (22). Thus, similar to EndoIII distribution, XPD, an NER protein with DNA-bound redox-activity, redistributes to localize in the vicinity of a C:A mismatch.

We also tested the possible redistribution of a CT-deficient mutant, L325V. The L325V XPD mutant exhibits an electrochemical signal that is less than half that of WT XPD (Figure 5.3), indicating its DNA CT deficiency. Interestingly, there is no preference for the mismatched strands; L325V exhibits a protein binding density ratio, r (long/short) of 1.14 ± 0.06 in mismatched samples, which is within error of the fully matched binding density ratio r (long/short) of 1.05 ± 0.07 (Figure 5.3). Thus, as with the CT-deficient EndoIII mutant Y82A (22), we find a correlation between the inability of L325V to perform CT and its lack of redistribution onto mismatched strands. Notably, even though the [4Fe-4S] cluster is intact, this mutant protein cannot cooperate with other proteins using DNA CT. This result identifies L325 as an important residue in DNA/protein CT.

Atomic Force Microscopy of Protein Mixtures

We have established that DNA-mediated CT occurs on a much faster timescale than protein diffusion (43, 44), and we have characterized several mutants of EndoIII from the BER repair pathway that exhibit similar midpoint potentials of ~ 80 (± 30) mV vs. NHE yet differ in their ability to carry out DNA CT (14, 23, 26). We have not yet provided evidence that different proteins can signal one another through DNA-mediated CT. AFM provides an opportunity to examine this by assaying protein mixtures.

WT XPD and EndoIII, both proficient at DNA CT, were mixed in a 1:1 equimolar ratio with DNA. Short duplex overhangs were blocked with excess complementary single strands. Figure 4 shows representative images of fully matched DNA strands or mismatched DNA strands incubated overnight with XPD/EndoIII 1:1 protein (WT^{XPD}/WT^{EndoIII}). XPD is twice as large as EndoIII (65 and 32 kDa respectively) (PDB IDs: 3CRV, 1P59). The average height of the protein in AFM studies can be estimated using the equation: $R=0.717(M)^{1/3}$ where R is the radius of the protein globule in Å and M is the mass of the protein in Da (45). Thus, XPD is expected to have a height of 5.6 nm, which is within error of EndoIII (4.6 nm). While we generally cannot distinguish them, select images (Figure 5.4 inset) are suggestive of both EndoIII and XPD binding. XPD (0.3 μ M)/EndoIII (0.3 μ M) 1:1 protein mixture shows that XPD and EndoIII redistribute onto long mismatched strands with a binding density ratio r (long/short) of 1.75 ± 0.13 . Fully matched controls yield a binding ratio r (long/short) of 1.02 ± 0.07 . Importantly, controls were also performed with only XPD (0.3 μ M) under the same conditions. Consistent with XPD at a higher concentration (0.6 μ M), XPD at half the concentration (0.3 μ M) redistributes onto long mismatched strands ($r=1.38 \pm 0.07$) with

no redistribution in fully matched samples ($r=1.08 \pm 0.07$). Significantly, mixing XPD and EndoIII protein results in a binding density ratio of 1.75, which is higher than that of each protein separately. This suggests that these two proteins signal one another to localize in the vicinity of the lesion.

To explore cooperativity between XPD and EndoIII, we replaced WT EndoIII with mutant Y82A EndoIII, a protein that binds to DNA but cannot perform DNA-mediated CT efficiently (22). In previous studies, Y82A did not redistribute in mismatched samples ($r=0.9 \pm 0.1$) (22). When XPD is mixed with Y82A 1:1 (WT^{XPD}/Y82A^{EndoIII}), there is no redistribution onto mismatched strands ($r=0.98 \pm 0.05$). WT^{XPD}/Y82A^{EndoIII} matched controls are within error of mismatched results with a binding density ratio of 1.11 ± 0.07 . The number of proteins bound per kilobasepair remains the same between WT^{XPD}/Y82A^{EndoIII} and WT^{XPD}/WT^{EndoIII} mixtures (0.13 proteins/kbp). When WT^{XPD} is titrated into Y82A^{EndoIII} at a ratio of 3:1, increasing the probability that the enzyme bound to the DNA strand is able to perform CT, the proteins once again redistribute onto mismatched strands.

Complementing WT^{XPD}/WT^{EndoIII} and WT^{XPD}/Y82A^{EndoIII} mixture studies, we also investigated signaling between EndoIII and XPD mutant L325V. Similar to EndoIII Y82A, XPD L325V cannot redistribute onto mismatched strands. WT^{XPD}/L325V^{XPD} 1:1 mixtures were examined initially to determine whether L325V, deficient in DNA CT, could signal XPD. WT^{XPD}/L325V^{XPD} mixtures showed no redistribution ($r=0.88 \pm 0.04$). This result was within error of matched controls, with a binding density ratio revealing even a slight preference for short strands ($r=0.90 \pm 0.05$). L325V inhibits XPD from relocalizing in the vicinity of lesions, but does L325V have any influence on the search

for damage by EndoIII BER protein? WT^{EndoIII}/L325V^{XPD} mixtures were examined and exhibited no difference in mismatched versus matched samples, where $r=1.02 \pm 0.05$ and 0.94 ± 0.04 respectively. As with the WT^{XPD}/Y82A^{EndoIII} mixture, here we see that L325V binding alters EndoIII redistribution. Figure 5.5 shows binding density ratio comparisons for WT^{XPD}/WT^{EndoIII}, WT^{XPD}/Y82A^{EndoIII}, WT^{EndoIII}/L325V^{XPD}, and WT^{XPD}/L325V^{XPD} 1:1 protein mixtures.

For mixtures of active proteins and CT-deficient mutants, we might have expected binding density ratios to be equal to that of pure samples of active repair protein. However, we are testing redistributions at protein loadings of ~2 per DNA strand. Thus if one of the proteins is CT-defective, there is no protein to which the CT-proficient protein may signal. Certainly the striking differences seen between CT-active protein mixtures and those containing CT-deficient mutants support the idea that the proteins can carry out DNA CT to one another. Having established that this ability to redistribute in the vicinity of mismatches depends on the ability of the protein to carry out DNA CT (23), these results thus provide evidence for DNA CT as a means of inter-protein signaling.

DISCUSSION

The data presented here indicate that XPD, an archaeal protein from the NER pathway, may cooperate with other DNA CT-proficient proteins to localize in the vicinity of damage. XPD, a superfamily 2 DNA helicase with 5'-3' polarity, is a component of TFIIH that is essential for repair of bulky lesions generated by exogenous sources such as UV light and chemical carcinogens (28, 46, 47). XPD contains a conserved [4Fe-4S] cluster that has been suggested to be conformationally controlled by ATP binding and hydrolysis (25). Mutations in the iron-sulfur domain of XPD can lead to diseases including TTD and XP, yet the function of the [4Fe-4S] cluster is currently unknown (23, 28, 29). Electrochemical studies have shown that when BER proteins MutY and EndoIII bind to DNA, their [4Fe-4S] clusters are activated toward one electron oxidation (14, 26). XPD exhibits a DNA-bound midpoint potential similar to that of EndoIII and MutY when bound to DNA (~80 mV vs. NHE), indicative of a possible role for the [4Fe-4S] cluster in DNA-mediated CT (33). For EndoIII, we have determined a direct correlation between the ability of proteins to redistribute in the vicinity of mismatches by AFM, and the CT proficiency of the proteins measured electrochemically (23). Thus, we may utilize single-molecule AFM as a tool to probe the redistribution of proteins in the vicinity of base lesions and in so doing, the proficiency of the protein to carry out DNA CT.

Here, we show that, like the BER protein EndoIII, XPD involved both in transcription and NER redistributes in the vicinity of a lesion. Importantly, this ability to relocalize is associated with the ability of XPD to carry out DNA CT, as the L325V mutant is DNA CT deficient and does not redistribute effectively onto the mismatched strand.

These data further provide evidence that two different repair proteins, each containing a [4Fe-4S] cluster at similar DNA-bound potential, can communicate with one another through DNA-mediated CT. This is especially interesting considering that the proteins are from completely different organisms. However, their critical attributes include similar DNA-bound potentials, facilitation of electron exchange, and the ability to carry out DNA-mediated CT. Furthermore, no signaling to effect the redistribution in the vicinity of lesions occurs when one partner is CT-deficient.

Lesion detection by repair proteins depends on the maximum distance over which DNA-mediated CT can occur and the percentage of proteins oxidized (6, 22, 48). While we have documented that DNA CT occurs over at least 100 bp, we do not yet know the maximum distance for this process (5, 49). If CT could proceed only over short distances (<500 bp), more than 6 proteins would be required for signaling across strands. Instead, only 1-3 proteins are bound to the long matched or mismatched strands in AFM experiments, suggesting that DNA CT is occurring over distances much greater than those we have measured electrochemically.

How might this signaling be utilized inside the cell? Surely this ability to redistribute in the vicinity of lesions reduces the search process required to find lesions across the genome. The higher the concentration of total proteins involved in signaling, the more efficient the search process becomes (22). Indeed, XPD may utilize DNA-mediated CT to signal its presence and perhaps to “call off” other proteins from other repair pathways. Various DNA-binding proteins, such as those involved in repair and other DNA transactions, have been found to contain iron-sulfur domains and other redox cofactors (50-53). DNA-mediated signaling among DNA-binding proteins that are

involved in maintaining the integrity of the genome allows a coordination of repair, transcription, and replication processes.

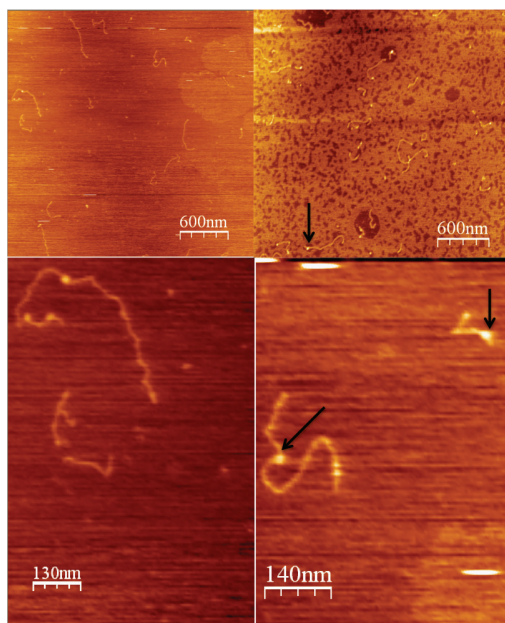


Figure 5.2 Atomic force microscopy to visualize protein. Tapping mode AFM images of DNA and XPD protein on mica imaged in air. The matched strands and protein (dots) are visible on the surface (top). Since the single strand overhangs on the short duplexes have been blocked by annealing short oligomers, XPD is bound in random positions on the DNA. Zoomed-in images of DNA long (3.8 kbp) and short (1.6 and 2.2 kbp) strands with bound proteins (black arrows) are shown below. Images were acquired with a scan size of $2 \times 2 \mu\text{m}^2$ or $3 \times 3 \mu\text{m}^2$, at a rate of 3.05 Hz with a data scale of 10 nm/ 0.5 V.

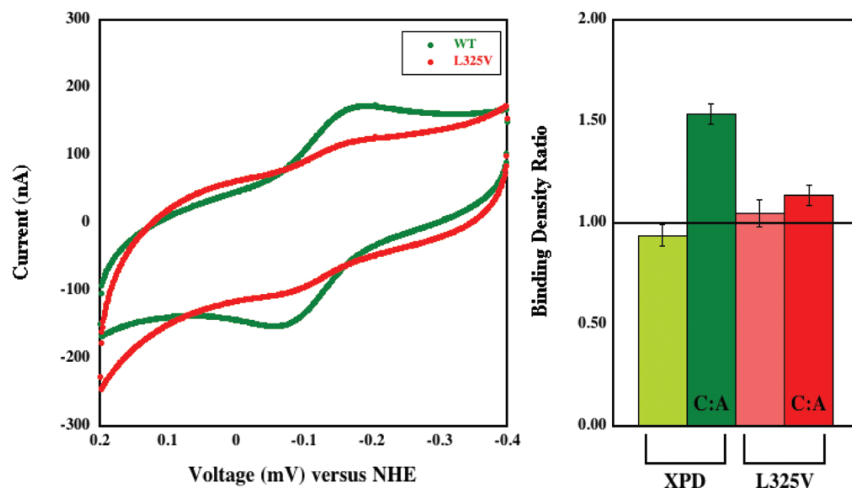


Figure 5.3 Electrochemistry of WT and L325V SaXPD (Left) Cyclic Voltammogram (CV) of WT SaXPD [8 μ M] (green) and L325V SaXPD [8 μ M] (red) on DNA modified electrodes after 90 minutes. (Right) Quantitation of XPD and mutant L325V protein density ratios (<10% uncertainty) where C:A indicates a mismatch is contained in long strands. The unmarked bars show the control measurements for fully matched long and short strands.

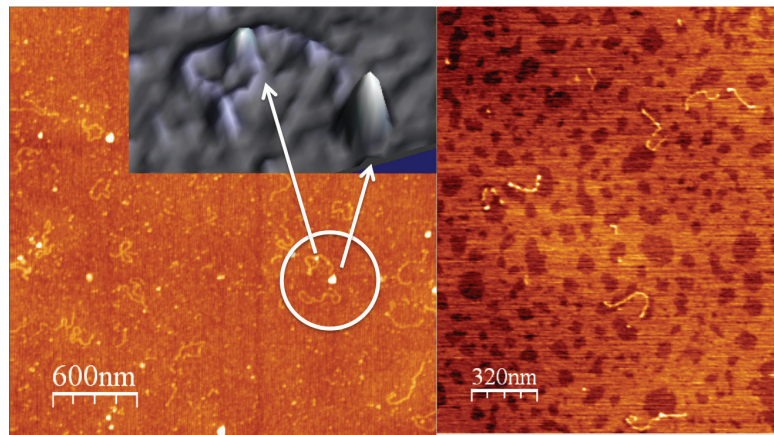


Figure 5.4 Representative tapping mode AFM images. Fully matched long and short DNA strands (*left*) or mismatched long DNA and matched short DNA strands (*right*) are incubated overnight with XPD/EndoIII 1:1 protein mixture. Inset shows zoomed-in view of a long DNA strand with both large and small proteins bound.

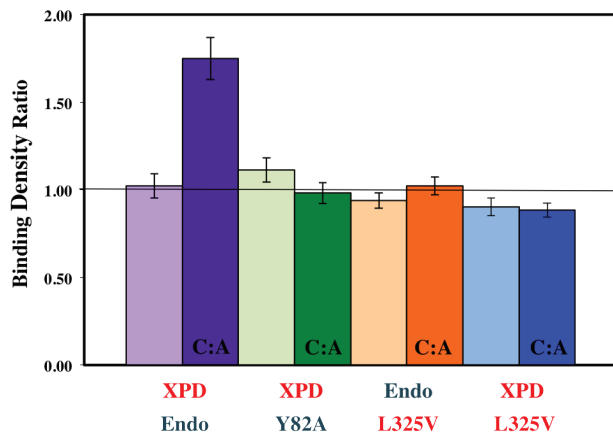


Figure 5.5 Binding density ratio of mixtures in SaXPD and EndoIII. XPD (red text)/EndoIII (blue text) and mutant mixtures binding density ratio comparisons. Quantitation of protein density ratios (<10% uncertainty) where C:A indicates a mismatch is contained in long strands. WT^{XPD}/WT^{EndoIII} mixtures 1:1 (purple), both proteins CT proficient, redistribute onto mismatched strands. WT^{XPD}/Y82A^{EndoIII} and WT^{EndoIII}/L325V^{XPD} 1:1 mixtures (green and orange respectively), Y82A and L325V both mutants deficient in CT, do not show redistribution. WT^{XPD}/L325V^{XPD} 1:1 mixtures (blue) do not show redistribution, as XPD cannot perform DNA-mediated signaling with itself if the L325V mutant is present.

Sample	BDR ^{a,b}	Long Strands	Proteins	Short Strands	Proteins	Error (%) ^c	Prot./Kbp
0.6 uM XPD	0.94	307	216	360	142	5.3	0.19
0.6 uM XPD (CA)	1.54	354	304	323	95	5	0.20
0.3 uM XPD	1.08	304	123	502	99	6.7	0.11
0.3 uM XPD (CA)	1.38	376	271	354	97	5.2	0.18
L325V 0.6 uM	1.05	221	149	251	85	6.5	0.18
L325V 0.6 uM (CA)	1.14	311	236	415	145	5	0.19
XPD/EndoIII 1:1	1.02	221	127	257	76	7	0.15
XPD/EndoIII 1:1 (CA)	1.75	253	150	370	66	7.6	0.13
XPD/Y82A 1:1	1.11	468	183	665	123	6	0.10
XPD/Y82A 1:1 (CA)	0.98	496	258	538	150	5	0.14
EndoIII/L325V 1:1	0.94	327	263	412	186	4.7	0.22
EndoIII/L325V 1:1 (CA)	1.02	361	217	553	171	5.1	0.16
XPD/L325V 1:1	0.90	309	174	408	134	5.7	0.16
XPD/L325V 1:1 (CA)	0.88	564	329	653	227	4.2	0.16

a. Binding Density Ratio (BDR) is reported as (number of proteins bound on long strands (3.6 kbp)) /number of long strands) divided by the (number of proteins on short strands (1.9 kbp))/number of short strands) normalized for length. (CA) represents samples with long mismatched strands.

b. These data represent three individual samples with 10-20 images per sample. L325V is a mutant of wild type XPD, and Y82A is a mutant of wild type EndoIII.

c. Error is reported as the (total number of proteins divided by the square root of the total number of proteins counted) times 100 for each type of sample.

Table 5.1. Binding Density Ratios for Atomic Force Microscopy Samples

References

1. Kuraoka I, *et al.*(2000) Removal of oxygen free-radical-induced 5', 8-purine cyclodeoxynucleosides from DNA by the nucleotide excision-repair pathway in human cells. *Proc Natl Acad Sci USA* 97: 3832-3837.
2. Sancar A, Lindsey-Boltz A, Ünsal-Kaçmaz K, Linn S (2004) Molecular Mechanisms of Mammalian DNA Repair and The DNA Damage Checkpoints. *Annu Rev Bioch* 73: 39-85.
3. David SS, Williams SD (1998) Chemistry of Glycosylases and Endonucleases Involved in Base-Excision Repair. *Chem Rev* 98:1221-1262.
4. David SS, O'Shea VL, Kundu S (2007) Base-excision repair of oxidative DNA damage. *Nature* 447: 941-950.
5. Slinker JD, Muren NB, Renfrew SE, Barton JK (2011) DNA charge transport over 34 nm. *Nat Chem* 3: 230-235.
6. Nunez ME, Hall DB, Barton JK (1999) Long Range Oxidative Damage to DNA: Effects of Distance and Sequence. *Chemistry and Biology* 6: 85-97.
7. Kelley SO, Boon EM, Barton JK, Jackson NM, Hill MG (1999) Single-Base Mismatch Detection Based on Charge Transduction Through DNA. *Nucl Acid Res* 27: 4830-4837.
8. Boal AK, Barton JK (2005) Electrochemical Detection of Lesions in DNA. *Bioconj Chem* 16: 312-321.
9. Genereux JC, Boal AK, Barton JK (2010) DNA-Mediated Charge Transport in Redox Sensing and Signaling. *J Am Chem Soc* 132: 891-905.
10. Boon EM, Livingston AL, Chmiel NH, David SS, Barton JK (2003) DNA-mediated charge transport for DNA repair. *Proc Natl Acad Sci USA* 100: 12543-12547.

11. Barton JK, Olmon ED, Sontz PA (2011) Metal complexes for DNA-mediated charge transport. *Coord Chem Rev* 255: 619-634.
12. Kuo CF, *et al.* (1992) Atomic structure of the DNA repair [4Fe-4S] enzyme endonuclease III. *Science* 258: 434-440.
13. Thayer MM, Ahern H, Xing D, Cunningham RP, Tainer JA (1995) Novel DNA binding motifs in the DNA repair enzyme endonuclease III crystal structure. *The EMBO Journal* 14: 4108-4120.
14. Gorodetsky AA, Boal AK, Barton JK (2006) Direct electrochemistry of endonuclease III in the presence and absence of DNA. *J Am Chem Soc* 128:12082-12083.
15. Porello SL, Cannon MJ, David SS (1998) A substrate recognition role for the [4Fe-4S]²⁺ cluster of the DNA repair glycosylase MutY. *Biochemistry* 37: 6465-6475.
16. Lukianova OA, David SS (2005) A role for iron-sulfur clusters in DNA repair. *Curr Opin Chem Biol* 9: 145-151.
17. Fromme JC, and Verdine GL (2003) Structure of a trapped endonuclease III- DNA covalent intermediate. *The EMBO Journal* 22, 3461- 3471.
18. Genereux JC, Boal AK, and Barton JK (2010) DNA-Mediated Charge Transport in Redox Sensing and Signaling. *J Am Chem Soc* 132, 891-905.
19. Fromme JC, Banerjee A, Huang SJ, and Verdine GL (2004) Structural basis for removal of adenine mispaired with 8- oxoguanine by MutY adenine DNA glycosylase, *Nature* 427, 652.
20. Cheadle JP, Sampson JR (2007) MUTYH-associated polyposis—from defect in base excision repair to clinical genetic testing. *DNA Repair* 6: 274-279.

21. Fodde R (2002) The APC gene in colorectal cancer. *Eur J Cancer* 38: 867-871.
22. Boal AK, *et al.* (2009) Redox signaling between DNA Repair Proteins for efficient lesion detection. *Proc Natl Acad Sci USA* 106: 15237-15242.
23. Romano CA, Sontz PA, Barton JK (2011) Mutants of the Base Excision Repair Glycosylase, Endonuclease III: DNA Charge Transport as a First Step in Lesion Detection. *Biochemistry* 50: 6133-5145.
24. Gorbatenya AE, Koonin EV (1993) Helicases: amino acid sequence comparisons and structure-function relationships. *Curr Opin Struc Biol* 3: 419-429.
25. Fan L, *et al.* (2008) XPD Helicase Structures and Activities: Insights into the Cancer and Aging Phenotypes from XPD Mutations. *Cell* 133: 789-800
26. Boal AK, *et al.* (2005) DNA-bound redox activity of DNA repair glycosylases containing [4Fe4S] clusters. *Biochemistry* 44: 8397-8407.
27. Yavin E, *et al.* (2005) Protein-DNA charge transport: Redox activation of a DNA repair protein by guanine radical. *Proc Natl Acad Sci USA* 102: 3546-3551.
28. Lehmann AR (2008) XPD structure reveals its secrets. *DNA Repair* 7: 1912-1915.
29. Fuss JO, Tainer JA (2011) XPB and XPD helicases in TFIIH orchestrate DNA duplex opening and damage verification to coordinate repair with transcription and cell cycle via CAK kinase DNA repair. *DNA Repair* 10: 697-713.
30. Takayama K, *et al.* (1996) Defects in the DNA Repair and Transcription Gene *ERCC2(XPD)* in Trichothiodystrophy. *Am J Hum Genet* 58: 263-270.
31. Taylor EM, *et al.* (1997) Xeroderma pigmentosum and trichothiodystrophy are associated with different mutations in the XPD (ERCC2) repair/transcription gene. *Proc Natl Acad Sci USA* 94: 8658-8663.

32. Rudolf J, Makrantoni V, Ingledew WJ, Stark MJR, White MF (2006) The DNA Repair Helicases XPD and FancJ Have Essential Iron-Sulfur Domains. *Molecular Cell* 23: 801-808.
33. Mui TP, Fuss JO, Ishida JP, Tainer JA, Barton JK (2011) ATP-Stimulated, DNA-Mediated Redox Signaling by XPD, a DNA Repair and Transcription Helicase. *J Am Chem Soc* 133, 41, 16378-16381.
34. Wolski SC, *et al.* (2008) Crystal Structure of the FeS Cluster-Containing Nucleotide Excision Repair Helicase XPD. *PLoS Biol* 6: 1332-1341.
35. Rudolf J, Rouillon C, Schwarz-Linek U, White MF (2010) The helicase XPD unwinds bubble structures and is not stalled by DNA lesions removed by the nucleotide excision repair pathway. *Nucl Acid Res* 38, 931-941.
36. Sun HB, Yokota H (2000) MutS-Mediated Detection of DNA Mismatches Using Atomic Force Microscopy. *Anal Chem* 72: 3138-3141.
37. Sorel I, *et al.* (2006) The EcoRI-DNA Complex as a Model for Investigating Protein-DNA Interactions by Atomic Force Microscopy. *Biochemistry* 45: 14675-14682.
38. Pastré D, *et al.* (2010) Specific DNA-Protein Interactions on Mica Investigated by Atomic Force Microscopy. *Langmuir* 26: 2618-2623.
39. Jiang Y, Marszalek PE (2011) Atomic force microscopy captures MutS tetramers initiating DNA mismatch repair. *The EMBO Journal* 30: 2881-2893.
40. Boon EM, Ceres DM, Drummond TG, Hill MG, Barton JK (2000) Mutation detection by electrocatalysis at DNA-modified electrodes. *Nature Biotechnology* 18: 1096-1100.

41. Donahue WF, Turczyk BM, Jarrell KA (2002) Rapid gene cloning using terminator primers and modular vectors. *Nucl Acid Res* 30: e95.
42. Rudolf J (2006) Characterisation of XPD from *Sulfolobus Acidocaldarius*: an Iron-Sulphur Cluster Containing DNA Repair Helicase. Thesis submitted for the degree of Doctor of Philosophy, University of St. Andrews.
43. *Charge Transfer in DNA: From Mechanism to Application* (2005) ed Wagenknecht HA (Wiley-VCH, Weinheim).
44. Berg OG, Winter RB, von Hippel PH (1981) Diffusion-driven mechanisms of protein translocation on nucleic acids, 1. Models and theory. *Biochemistry* 20: 6929-6948.
45. *Atomic Force Microscopy Biomedical Methods and Applications* (2004) ed Braga PC, Ricci D (Humana Press; Totowa, NJ).
46. Liu H, *et al.* (2008) Structure of the DNA Repair Helicase XPD. *Cell*, 133: 801-812.
47. Broughton BC, *et al.* (2001) Two individuals with features of both xeroderma pigmentosum and trichothiodystrophy highlight the complexity of the clinical outcomes of mutations in the *XPD* gene. *Hum Mol Gen* 19, 2539-2547.
48. Yavin E, Stemp EDA, O'Shea VL, David SS, Barton JK (2006) Electron trap for DNA-bound repair enzymes: a strategy for DNA-mediated signaling. *Proc Natl Acad Sci USA* 103:3610-3614.
49. Nunez ME, Noyes KT, Barton JK (2002) Oxidative charge transport through DNA in nucleosome core particles. *Chem Biol* 9: 403-415.
50. Lee PE, Demple B, Barton JK (2009) DNA-mediated redox signaling for transcriptional activation of SoxR. *Proc Natl Acad Sci USA* 106: 13164-13168.

51. Augustyn KE, Merino EJ, Barton JK (2007) A role for DNA-mediated charge transport in regulating p53: Oxidation of the DNA-bound protein from a distance. *Proc Natl Acad Sci USA* 104: 18907-18912.
52. Merino EJ, Barton JK (2008) DNA Oxidation by Charge Transport in Mitochondria. *Biochemistry* 47, 1511-1517.
53. Klinge S, Hirst J, Maman JD, Krude T, Pellegrini L (2007) An iron-sulfur domain of the eukaryotic primase is essential for initiation of RNA primer synthesis. *Nat Struct Mol Biol* 14: 875-877.
54. Davis RW, Botstein D, Roth JR (1980) Advanced Bacterial Genetics: A Manual for Genetic Engineering (Cold Spring Harbor: Cold Spring Harbor Laboratory Press).
55. Cunningham RP, *et al.* (1989) Endonuclease III is an iron-sulfur protein. *Biochemistry* 28:4450-4455.
56. Horcas I, *et al.* WSXM: a software for scanning probe microscopy and a tool for nanotechnology. *Rev Sci Instrum* 78: 013705.

Chapter 6

Summary and Outlook

As a molecule, DNA appears at first glace to be simple, but is in actuality incredibly complicated, and is the basis of cell life. DNA is composed of only four unique sugars, the nucleobases, connected by a sugar phosphate backbone. Individual DNA strands base pair in an anti-parallel manner to form a double helix. Permutations in the sequence of the four individual nucleobases encode the entire genome for a particular organism. Genetic information is subsequently transcribed into RNA that is then translated into proteins, which perform the majority of cellular functions. Therefore, mutations in the genome have extremely detrimental downstream effects that can lead to many diseases, including progeria and cancers. DNA damage comes from a variety of sources, ranging from external chemicals and ionizing energy to internal reactive oxygen species and mistakes by the proteins involved in genome replication. The cell has developed many pathways to prevent and repair DNA damage. These processes, including base excision repair (BER), nucleotide excision repair (NER), homologous recombination (HR), non-homologous end joining (NHEJ), and mismatch repair (MMR), all involve the coordination of dozens of proteins that must identify a site of DNA damage and subsequently coordinate the repair of the lesion. While some proteins are involved in more than one repair pathway, many of them are distinct and are only utilized in a single repair pathway. Throughout many organisms, these repair processes are well conserved, with protein homologues identified in each organism.

One unique property of DNA that is often overlooked is its ability to conduct charge. As a duplex, DNA is capable of sending electrons through the π -stacked aromatic bases in a phenomenon known as DNA Charge Transport (CT). This process is sensitive to the integrity of the DNA π -stack, as perturbations to individual bases

diminishes the ability of the molecule to conduct charge, while damage to the sugar phosphate backbone will not attenuate CT. DNA CT has been observed through 100 bases (34 nm) and is believed to occur over much longer distances. Additionally, it has a β value, which reflects the dependence of electron transfer on distance, less than 0.05 making it an especially efficient conductor of charge. It has been proposed that proteins can utilize DNA-mediated CT to signal one another to coordinate at a site of DNA damage. Using two base excision repair (BER) proteins from *E. coli*, EndoIII and MutY that contain a [4Fe-4S] cluster, it was found that these proteins both exhibit a DNA bound redox potential of 80 mV versus NHE. We also found that in the oxidized state (3+), these proteins have a 1000-fold increase in binding affinity for DNA as compared to the reduced state (2+). A model was therefore developed to describe the coordinated signaling between BER proteins to localize to a site of DNA damage. Briefly, when a redox protein binds DNA, it is activated towards oxidation and releases an electron to a distally bound protein through the DNA. If the DNA is intact, the second protein can receive the electron, become reduced, and dissociate from the DNA. However, if the DNA is damaged, this process cannot occur; the protein remains bound on the DNA and subsequently processes toward the site of damage. This model describes an efficient search process for proteins that are low in copy number with a very short search time for scanning the entire genome. It is therefore important to examine the role of proteins that a) contain a redox active cluster, b) bind DNA, and c) have an active role in DNA repair. This work expands on our collection of DNA binding proteins that can utilize DNA-mediated CT and furthers our understanding of the role of DNA-mediated signaling between repair proteins as a conserved mechanism throughout many organisms.

We electrochemically characterized the NER helicase XPD from the thermophile *Sulfolobus acidocaldarius*. Using a DNA-modified electrode with a 5' ssDNA overhang, which is a substrate for the helicase, we observed a DNA-bound redox potential of 82 mV versus NHE, consistent with the previously reported value for BER proteins. We then sought to understand what role ATP hydrolysis has on DNA-mediated signaling, as XPD is an ATP-dependent helicase. After incubating SaXPD on the electrode, a titration of ATP and ATP- γ -S was performed. When 5 mM ATP was added, an increase in the current was observed, consistent with previously reported kinetic measurements. A mutant deficient in helicase and ATPase activity, G34R, was subjected to the same conditions, and, upon ATP addition, showed minimal increase in electrochemical current. SaXPD exhibits a preference for a 5' ssDNA overhang, and when this ATPase assay was performed with either a 3' ssDNA overhang or no overhang, only a minimal increase in signal was observed, followed by subsequent signal decay, suggesting that the protein is sliding off the DNA substrate. Therefore, SaXPD exhibits a DNA-mediated signaling event associated with ATP hydrolysis. The ATP binding site is over 30 angstroms from the cluster, and it is intriguing that ATP binding and hydrolysis can affect DNA mediated signaling. The current increase was small, approximately 10%, likely because the protein functions at elevated temperature, and these assays are performed at room temperature.

Because of the results observed with SaXPD, we were then interested in exploring the effect of disease-related mutants on DNA-mediated electrochemistry; databases of protein mutants involved in the XP-related diseases xeroderma pigmentosum (XP), trichothiodystrophy (TTD), and cockayne syndrome (CS) were used to identify targets.

The G34R mutant is a typical mutant because it lacks ATPase and helicase activity, but other mutants involved in disease are not as straightforward. In Chapter 3, we describe the electrochemistry of the disease-related K84H, L325V, R460P, R460W, A511R, and the artificial Y104A mutants. The L325V, R460P, R460W, and A511R all appear to have reduced DNA-mediated signaling relative to the WT proteins, while the Y104A and K84H mutants have enhanced electronic signaling. The CT-deficient mutants L325V and R460W, which maintain ATPase activity, helicase activity, bind DNA, and bind TFIIH, were particularly puzzling because they continued to lead to either TTD, XP, or COFS. Perhaps their deficiencies in CT are the major contributing factor to the disease state. Attempts were made to restore CT using our enhanced Y104A mutant in combination with either CT-deficient mutant, but each double mutant exhibited lower electrochemical signals than its single mutant counterparts. Using the SaXPD crystal structure, we modeled a mutant to restore CT to the L325V mutant. This L325V/M331A mutant has an electrochemical signal slightly higher than the original L325V mutant, but lacks ATPase and helicase activity.

We then focused on the yeast *S. cerevisiae* XPD homologue, Rad3. A haploid deletion strain of Rad3 was generated and complemented with a plasmid-based copy of Rad3, enabling ready manipulation of the Rad3 copy in the cell. The analogous mutations to the SaXPD mutants were generated and assayed for survival. All mutants were viable, indicating that none completely abolish Rad3 activity *in vivo*. The viability of these disease-related mutants speaks to the differences between the ScRad3 and human XPD. To test the ability of Rad3 mutations *in vivo*, a UV-induced and NQO-induced survival assay was performed. Both of these assays yielded similar results, indicating

that UV-induced lesions and quinol-DNA adducts are repaired with the same efficiency by ScRad3. The ATPase and helicase deficient ScRad3 mutants G47R, R618P, and C665R showed little to no growth at either 20 J/m² or 20 ng/mL NQO, while the I463V/Δ and R618W mutants showed growth similar to the WT strain, albeit with a slight deficiency. When monitoring key genes involved in DNA repair, no strain-specific increase in transcription was observed, indicating that Rad3 is not involved in regulating these genes in response to DNA damage.

In the ScRad3 strain, when mutations were made at the R618 position, we found survival in the order of proline < glutamate < alanine < tryptophan < tyrosine ≈ leucine ≈ arginine (WT), suggesting that mutations at this position drastically affect survival. Large bulky mutations that affect structure, such as proline and glutamate, lead to inviability, while maintaining aromaticity in tryptophan and tyrosine lead to results similar to the WT Rad3 strain. To investigate the kinetics of the repair process, growth was monitored and demonstrated that the G47R, R618P, and C665R mutant strains show significant attenuation in growth in the presence of NQO, while the WT, I463V/Δ, and R618W strains grow with only a small shift in $t_{1/2} \approx 1.5$ hours.

Finally, the ability of Rad3 to repair other DNA damage products was tested through monitoring of the growth of WT and G47R Rad3 strains in the presence of methyl methanesulfonate (MMS), camptothecin (CPT), and hydroxyurea (HU). For HU, both strains exhibited similar attenuated growth, while the G47R strain showed significant attenuation relative to the WT strain in the presence of MMS and CPT, suggesting that Rad3 assists with the repair of methylated DNA or cross-linked DNA, respectively. To better understand the biochemistry of the protein, we purified Rad3

from *S. cerevisiae* in *E. coli* cells. Mutants purified from *E. coli* exhibited ATPase, helicase, and DNA binding activities, albeit with variation from previously reported SaXPD results, likely due to protein instability in the storage buffer. Rad3 also contains a [4Fe-4S] cluster, as observed by UV-visible spectroscopy. When incubated on a DNA-modified electrode, Rad3 exhibits a DNA-bound redox potential of 80 mV versus NHE. All mutants exhibit this potential and have the same current intensity relative to the WT protein. While many of the disease-related mutants show diminished activities in our *in vivo* *S. cerevisiae* assay, the R618W and I463V/Δ mutants are viable. The ScRad3 protein is significantly different from the previously studied SaXPD, and a full understanding of ScRad3 will establish what role CT plays and provide key insights into the molecular basis for XP-related diseases.

The fact that these proteins all have a similar potential on a DNA-modified electrode enables the expansion of our model for protein utilization of DNA-mediated signaling. We have developed an atomic force microscopy (AFM) assay to measure distribution onto well-matched and mismatched DNA strands. In this assay, the BER protein EndoIII redistributes onto a long strand of DNA containing a C:A mismatch, compared to a short strand that is well-matched. Similarly, with SaXPD, the protein redistributes with a binding density ratio (BDR) of 1.54 ± 0.08 , and the L325V CT deficient mutant redistributes with a BDR of 1.14 ± 0.06 . When a mixture of the WT and L325V mutant SaXPD were incubated with DNA, a BDR of 0.88 ± 0.04 was found, suggesting that a deficiency in protein CT does not allow proteins to redistribute near a DNA lesion. When SaXPD and *E. coli* EndoIII were mixed, a BDR of 1.75 ± 0.14 was observed. When a CT deficient version of SaXPD or EndoIII was added, BDRs of $1.02 \pm$

0.05 and 0.98 ± 0.05 were observed, respectively. These data suggest that the CT proficiency in a protein affects redistribution near the site of a DNA lesion that attenuates CT. These two proteins are also from both entirely different repair pathways (NER versus BER) and completely different organisms (*S. acidocaldarius* versus *E. coli*), suggesting that DNA-mediated signaling is a general mechanism amongst all forms of life.

Taken together, this body of work vastly expands our repertoire of proteins that are capable of utilizing DNA CT. We have correlated ATPase activity with electrochemical signaling, as observed in SaXPD, and demonstrated that signaling between proteins from different organisms can localize at a DNA lesion. We have begun work to uncover other proteins that can utilize this signaling pathway. Beyond the NER SaXPD and ScRad3 proteins and the BER EndoIII and MutY proteins, the human primase, yeast Dna2, *E. coli* DinG, and the yeast polymerases all contain a redox active [4Fe-4S] cluster. All of these proteins exhibit the same DNA-bound redox potential, allowing them to signal one another. Perhaps to coordinate repair between the different repair pathways, these proteins utilize DNA-mediated signaling to identify the presence of other redox active proteins or to simply be used as redox shuttles to coordinate the repair proteins in the vicinity of DNA lesions.

Appendix 1

Primers and strains used in *S. cerevisiae* *in vivo* assays

TPM 033:	CTTCCGTTATTACTCAGGGACC <u>GTAT</u> CACCATTAG	(39-mer)
TPM 034:	CTTGGATACTGTCTAATGGTG <u>TAC</u> GGTCCCTGAAG	(37-mer)
TPM 046:	GATGCCTTCAGGAACA <u>CGTAAA</u> AC GG	(26-mer)
TPM 041:	GGATAGTAATGAGACC GTTT <u>ACGT</u> GTT CCTG	(32-mer)
TPM 042:	TATCGATTTGATCATCAATAT <u>CCCAGAA</u> CT GTGC	(35-mer)
TPM 043:	TACCTATCATCAGCACAGT TCT <u>GGGATATTG</u>	(31-mer)
TPM 044:	ACATGCAGCTCAA <u>CGTCTGGGG</u>	(22-mer)
TPM 045:	AGTACTCTCCCCAG <u>ACGTTGAGCTG</u>	(25-mer)
TPM 048:	CAGTTTAAAGTTAACATTCTGGATA <u>CGC</u> GTCTAATGGTG	(42-mer)
TPM 049:	CAGGGACC <u>GTAT</u> CACCATTAGAC <u>GCG</u> TATCCAAG	(34-mer)
TPM 057:	CTTCCGTTATTACTCAGGGACC <u>CTA</u> CACCATTAG	(39-mer)
TPM 058:	CTTGGATACTGTCTAATGGTG <u>TAG</u> GGTCCCTGAAG	(37-mer)
TPM 059:	CTTCCGTTATTACTCAGGGACC <u>TTC</u> CACCATTAG	(39-mer)
TPM 060:	CTTGGATACTGTCTAATGGTG <u>GAA</u> GGTCCCTGAAG	(37-mer)
TPM 071:	GATTTGATCATCAATATGGC <u>CCA</u> ACTGTGCTGA	(34-mer)
TPM 072:	TACCTATCATCAGCACAGT <u>TGGGCC</u> ATTTG	(31-mer)
TPM 073:	GATTTGATCATCAATATGGC <u>TGG</u> ACTGTGCTGA	(34-mer)
TPM 074:	TACCTATCATCAGCACAGT <u>CCA</u> GCCATATTG	(31-mer)
TPM 099:	<u>ACTGACATGGCCATATCCAAT</u> GACCAAGAGGGGTATCT	(39-mer)
TPM 100:	AACAGATAACCCCTTGGTC <u>ATTGGATATGCCATGTC</u>	(39-mer)
TPM 102:	GATTTGATCATCAATATGGC <u>GCA</u> ACTGTGCTGA	(34-mer)
TPM 103:	TACCTATCATCAGCACAGT <u>TGC</u> GCCATATTG	(31-mer)
TPM 104:	GATTTGATCATCAATATGGC <u>GAA</u> ACTGTGCTGA	(34-mer)
TPM 105:	TACCTATCATCAGCACAGT <u>TTC</u> GCCATATTG	(31-mer)
TPM 106:	GATTTGATCATCAATATGGC <u>CTA</u> ACTGTGCTGA	(34-mer)
TPM 107:	TACCTATCATCAGCACAGT <u>TAGGCC</u> ATTTG	(31-mer)
TPM 112:	<u>CG</u> ATTTGATCATCAATATGGC <u>TAC</u> ACTGTGCTG <u>ATG</u>	(37-mer)
TPM 113:	<u>GG</u> ATACCTATCATCAGCACAGT <u>GTAA</u> CCATATTG <u>AT</u>	(36-mer)
TPM 033:	Forward Primer to I463V mutation in Rad3	
TPM 034:	Reverse Primer to I463V mutation in Rad3	
TPM 046:	Forward Primer to make G47R in Rad3	
TPM 041:	Reverse Primer to make G47R in Rad3	
TPM 042:	Forward Primer to make R460P (G617P)	
TPM 043:	Reverse Primer to make R460P (G617P)	
TPM 044:	Forward Primer to make A511R (C665R)	
TPM 045:	Reverse Primer to make A511R (C665R)	
TPM 047:	Reverse Primer to mutate M488A	
TPM 048:	Forward Primer to mutate I463V/M488A	
TPM 057:	Forward Primer to I460L mutation in Rad3	
TPM 058:	Reverse Primer to I460L mutation in Rad3	
TPM 059:	Forward Primer to I460F mutation in Rad3	
TPM 060:	Reverse Primer to I460F mutation in Rad3	

TPM 071:	Forward Primer to R460P (R618P) Mutation in Rad3
TPM 072:	Reverse Primer to R460P (R618P) Mutation in Rad3
TPM 073:	Forward Primer to R460W (R618W) Mutation in Rad3
TPM 074:	Reverse Primer to R460W (R618W) Mutation in Rad3
TPM 099:	Forward Primer for 716-730 del in Rad3
TPM 100:	Reverse Primer for 716-370 del in Rad3
TPM 102:	Forward Primer to R460A (R618A) Mutation in Rad3
TPM 103:	Reverse Primer to R460A (R618A) Mutation in Rad3
TPM 104:	Forward Primer to R460E (R618E) Mutation in Rad3
TPM 105:	Reverse Primer to R460E (R618E) Mutation in Rad3
TPM 106:	Forward Primer to R460L (R618L) Mutation in Rad3
TPM 107:	Reverse Primer to R460L (R618L) Mutation in Rad3
TPM 112:	Forward Primer to R460Y (R618Y) Mutation in Rad3
TPM 113:	Reverse Primer to R460Y (R618Y) Mutation in Rad3

Table S1.1. Primers used for Site Directed Mutagenesis (SDM). Sequence are shown above with description as indicated below.

TPM 061:	ATTATATGTTAGAGGTTGCTGCTTGG	(28-mer)
TPM 062:	CAATTCGTTGTAGAAGGTATGATGCC	(26-mer)
TPM 063:	CACGGATAGTGGCTTGCGAACATTAC	(29-mer)
TPM 064:	TATGATTATCTGGCAGCAGGAAAGAACTTGGG	(32-mer)
TPM 065:	GCTGGCACTCATATCTTATCGTTCACATGG	(32-mer)
TPM 066:	GAACCTGCTGTCAAATACCGCCTGGAG	(26-mer)
TPM 067:	ATTGGCCCGTCTGTTGCTGTG	(24-mer)
TPM 068:	TATGCTGAATCTCGTCTAGTTCTGTAGG	(30-mer)
TPM 069:	AGTTCAAGGTCTCCATTCTGC	(21-mer)
TPM 070:	CTCGGCTCTCGTATATTCCC	(22-mer)
TPM 075:	AAATGTTGGTAATGGCGTG	(21-mer)
TPM 076:	TTGCATGACGGAGACTGATG	(20-mer)
TPM 077:	GCTACACCAACATCCATTAAACG	(22-mer)
TPM 078:	CCAGTATTAGAGAACCAACGACAG	(23-mer)
TPM 079:	ATAACGGGTGGATTCTTGGAC	(21-mer)
TPM 080:	CCCGTCCTCAGCATTACTATC	(21-mer)
TPM 081:	AGCATACTCCAAGCCAATCG	(20-mer)
TPM 082:	CCGTAGTGTCTTCAGAGTTTC	(22-mer)
TPM 083:	TCAGGGCATACGGTCTTTG	(20-mer)
TPM 084:	CTGTTGGCGGTAGATCAC	(19-mer)
TPM 085:	CAGATAGTCAACGTCCAGGTAAG	(23-mer)
TPM 086:	AGATTGATGGTCTCACGCG	(20-mer)
TPM 087:	TTACGCCAGTTCCCCTAAC	(20-mer)
TPM 088:	TTGGAAGCCCTCTCAGAAATAG	(22-mer)
TPM 089:	AGAGCATTCTATAAGGGCACAC	(22-mer)
TPM 090:	TTGTATCTCATGACACCCGTG	(21-mer)
TPM 091:	GTCCTCATACTGCTCTCACATG	(22-mer)
TPM 092:	GCATACGGCGTCATTAATTG	(21-mer)

TPM 093:	GAGTGTGCTGGTAGGATTGG	(20-mer)
TPM 094:	ATGGGTGAGCATGTATTCAAGAG	(22-mer)
TPM 095:	ATGGATCAACCTGTCGACTTG	(21-mer)
TPM 096:	TGTAGGAACCCACTCTCAAATC	(23-mer)
TPM 097:	ACCATATGAAGGCTCTGTTGAG	(22-mer)
TPM 098:	TCACCGAATGATATCACCC	(20-mer)
TPM 061:	Forward Primer ACT1 RT-QPCR Tm 64.2	
TPM 062:	Reverse Primer ACT1 RT-QPCR Tm 63.8	
TPM 063:	Forward Primer ALG9 RT-QPCR Tm 67.3	
TPM 064:	Reverse Primer ALG9 RT-QPCR Tm 69.2	
TPM 065:	Forward Primer TFCI RT-QPCR Tm 68.5	
TPM 066:	Reverse Primer TFCI RT-QPCR Tm 69.6	
TPM 067:	Forward Primer PDAI RT-QPCR Tm 68.3	
TPM 068:	Reverse Primer PDAI RT-QPCR Tm 66.3	
TPM 069:	Forward Primer Rad3 RT-QPCR Tm 62.0	
TPM 070:	Reverse Primer Rad3 RT-QPCR Tm 62.2	
TPM 075:	Forward Primer Ss12 RT-QPCR Tm 62.0 (143)	
TPM 076:	Reverse Primer Ss12 RT-QPCR Tm 62.1	
TPM 077:	Forward Primer Rad1 RT-QPCR Tm 61.5 (125)	
TPM 078:	Reverse Primer Rad1 RT-QPCR Tm 61.9	
TPM 079:	Forward Primer Rad2 RT-QPCR Tm 62.0 (122)	
TPM 080:	Reverse Primer Rad2 RT-QPCR Tm 61.6	
TPM 081:	Forward Primer Met18 RT-QPCR Tm 62.3 (126)	
TPM 082:	Reverse Primer Met18 RT-QPCR Tm 62.1	
TPM 083:	Forward Primer Rad50 RT-QPCR Tm 62.1 (150)	
TPM 084:	Reverse Primer Rad50 RT-QPCR Tm 62.0	
TPM 085:	Forward Primer Isa1 RT-QPCR Tm 61.9 (128)	
TPM 086:	Reverse Primer Isa1 RT-QPCR Tm 62.4	
TPM 087:	Forward Primer Isa2 RT-QPCR Tm 61.8 (146)	
TPM 088:	Reverse Primer Isa2 RT-QPCR Tm 61.7	
TPM 089:	Forward Primer Pol1 RT-QPCR Tm 62.1 (147)	
TPM 090:	Reverse Primer Pol1 RT-QPCR Tm 61.8	
TPM 091:	Forward Primer Pol2 RT-QPCR Tm 62.0 (150)	
TPM 092:	Reverse Primer Pol2 RT-QPCR Tm 61.7	
TPM 093:	Forward Primer Pol3 RT-QPCR Tm 62.0 (137)	
TPM 094:	Reverse Primer Pol3 RT-QPCR Tm 62.1	
TPM 095:	Forward Primer Pol30 RT-QPCR Tm 62.1 (146)	
TPM 096:	Reverse Primer Pol30 RT-QPCR Tm 62.2	
TPM 097:	Forward Primer Rfc1 RT-QPCR Tm 62.0 (84)	
TPM 098:	Reverse Primer Rfc1 RT-QPCR Tm 61.9	

Table S1.2. Primers used for qPCR. Sequences of primers used for the genes involved in the qPCR experiments.

Parental Plasmid	Rad3 Mutation	Strain Transformed
12AB-Rad3	WT	<i>S. cerevisiae</i>
12AC-Rad3	WT	<i>S. cerevisiae</i>
7AB-HSSG-12xHis Rad3	WT	<i>E. coli</i> BL21 DE3 pLysS
7AB-12xHis Rad3	WT	<i>E. coli</i> BL21 DE3 pLysS
7AB-6xHis Rad3	WT	<i>E. coli</i> BL21 DE3 pLysS
7AC-MBP-6xHis Rad3	WT	<i>E. coli</i> BL21 DE3 pLysS
	I463V/del71 6-730	<i>E. coli</i> BL21 DE3 pLysS
	G47R	<i>E. coli</i> BL21 DE3 pLysS
	R618P	<i>E. coli</i> BL21 DE3 pLysS
	R618W	<i>E. coli</i> BL21 DE3 pLysS
	I463V/M46 8A/del716-730	<i>E. coli</i> BL21 DE3 pLysS
	C665R	<i>E. coli</i> BL21 DE3 pLysS
	I463L	<i>E. coli</i> BL21 DE3 pLysS
PRS314 – Rad3	WT	Untransformed
PRS313 – Rad3	WT	<i>S. cerevisiae</i> his3Δ1 leu2Δ0 met15Δ0 ura3Δ0 ΔRad3::kan
	I463V/del71 6-730	<i>S. cerevisiae</i> his3Δ1 leu2Δ0 met15Δ0 ura3Δ0 ΔRad3::kan
	G47R	<i>S. cerevisiae</i> his3Δ1 leu2Δ0 met15Δ0 ura3Δ0 ΔRad3::kan
	R618P	<i>S. cerevisiae</i> his3Δ1 leu2Δ0 met15Δ0 ura3Δ0 ΔRad3::kan
	R618W	<i>S. cerevisiae</i> his3Δ1 leu2Δ0 met15Δ0 ura3Δ0 ΔRad3::kan
	I463V/M48 A/del716-730	<i>S. cerevisiae</i> his3Δ1 leu2Δ0 met15Δ0 ura3Δ0 ΔRad3::kan
	C665R	<i>S. cerevisiae</i> his3Δ1 leu2Δ0 met15Δ0 ura3Δ0 ΔRad3::kan
	R618A	<i>S. cerevisiae</i> his3Δ1 leu2Δ0 met15Δ0 ura3Δ0 ΔRad3::kan
	R618E	<i>S. cerevisiae</i> his3Δ1 leu2Δ0 met15Δ0 ura3Δ0 ΔRad3::kan
	R618L	<i>S. cerevisiae</i> his3Δ1 leu2Δ0 met15Δ0 ura3Δ0

		Δ Rad3::kan
	R618Y	<i>S. cerevisiae</i> his3 Δ 1 leu2 Δ 0 met15 Δ 0 ura3 Δ 0 Δ Rad3::kan
	G617P	<i>S. cerevisiae</i> his3 Δ 1 leu2 Δ 0 met15 Δ 0 ura3 Δ 0 Δ Rad3::kan
	I463F	<i>S. cerevisiae</i> his3 Δ 1 leu2 Δ 0 met15 Δ 0 ura3 Δ 0 Δ Rad3::kan
	I463L	<i>S. cerevisiae</i> his3 Δ 1 leu2 Δ 0 met15 Δ 0 ura3 Δ 0 Δ Rad3::kan
PRS316 – Rad3	WT	<i>S. cerevisiae</i> Mata/Mat α his3 Δ 1 leu2 Δ 0 met15 Δ 0 ura3 Δ 0 Δ Rad3::kan

Table S1.3 Table of plasmids and yeast strains developed to study survival of Rad3 mutations and overexpression of Rad3 in *E. coli*.